

Stephen F. Austin State University

SFA ScholarWorks

Electronic Theses and Dissertations

Spring 5-13-2017

Structural and Stratigraphic Reconstruction of the Whiting Dome Salt Structure in Viosca Knoll-Mississippi Canyon, GOM, Using 3D Seismic Data

Matthew R. Worrell

Stephen F Austin State University, worrellmr@gmail.com

Follow this and additional works at: <https://scholarworks.sfasu.edu/etds>



Part of the [Geology Commons](#), [Geophysics and Seismology Commons](#), [Stratigraphy Commons](#), and the [Tectonics and Structure Commons](#)

[Tell us](#) how this article helped you.

Repository Citation

Worrell, Matthew R., "Structural and Stratigraphic Reconstruction of the Whiting Dome Salt Structure in Viosca Knoll-Mississippi Canyon, GOM, Using 3D Seismic Data" (2017). *Electronic Theses and Dissertations*. 97.

<https://scholarworks.sfasu.edu/etds/97>

This Thesis is brought to you for free and open access by SFA ScholarWorks. It has been accepted for inclusion in Electronic Theses and Dissertations by an authorized administrator of SFA ScholarWorks. For more information, please contact cdsscholarworks@sfasu.edu.

Structural and Stratigraphic Reconstruction of the Whiting Dome Salt Structure in Viosca Knoll-Mississippi Canyon, GOM, Using 3D Seismic Data

Creative Commons License



This work is licensed under a [Creative Commons Attribution-Noncommercial-No Derivative Works 4.0 License](https://creativecommons.org/licenses/by-nc-nd/4.0/).

STRUCTURAL AND STRATIGRAPHIC RECONSTRUCTION OF THE WHITING DOME
SALT STRUCTURE IN VIOSCA KNOLL-MISSISSIPPI CANYON, GOM, USING 3D
SEISMIC DATA

By

MATTHEW ROY WORRELL, BA in Anthropology, BS in Geology

Presented to the Faculty of the Graduate School of

Stephen F. Austin State University

In Partial Fulfillment

Of the Requirements

For the Degree of

Master of Science

STEPHEN F. AUSTIN STATE UNIVERSITY

May 2017

STRUCTURAL AND STRATIGRAPHIC RECONSTRUCTION OF THE WHITING DOME
SALT STRUCTURE IN VIOSCA KNOLL-MISSISSIPPI CANYON, GOM, USING 3D
SEISMIC DATA

By

MATTHEW ROY WORRELL, BA in Anthropology, BS in Geology

APPROVED:

Dr. Wesley Brown, Thesis Director

Jim Ferry, Committee Member

Dr. R. Larell Nielson, Committee Member

Dr. Joseph Musser, Committee Member

Richard Berry, D.M.A.
Dean of the Graduate School

ABSTRACT

Understanding the complexities of salt tectonics is one of the most important factors regarding seismic interpretation of stratigraphy, structure, and geomorphology in the Gulf of Mexico. Evaluating the processes affecting recent mobilization of salt in the shallow, well-imaged section can help provide analogues for older, similar occurrences in the deeper section, thereby providing structural models for the autochthonous salt and its effect on stratigraphy and even potential timing and migration issues of hydrocarbons.

Progradation of delta front and shelf to slope transitional sediments has expelled and emplaced an allochthonous salt structure (Whiting Dome) in the Viosca Knoll and Mississippi Canyon protraction areas of the Gulf of Mexico. Multiple salt mobilization concepts were employed in order to more specifically define the different stages of this salt structure. In chronologic order, these include Roho (expulsion and initial emplacement), shelf- and slope-loaded salt withdrawal minibasin and detachment (early development), whole cell gravity gliding (late development), and reactive halokinesis influenced diapir creation (current).

A model was developed that describes the interplay between salt tectonics and sedimentation through time based on intensive study of the geologic history of the area, interpretation of 3D seismic data, stratigraphic mapping outboard and above the major salt structures, and conceptual restorations.

Interpretation of the 3D seismic data was completed using IHS Kingdom 15. The three-dimensional seismic data used in this study was generously provided by TGS. All well information and well log data was sourced from the Bureau of Safety and Environmental Enforcement's public data domain. Strata are delineated using well log data and the MMS Biostratigraphic Chart publically available through the Bureau of Ocean Energy Management.

ACKNOWLEDGEMENTS

First and foremost, I would like to thank my wife for not killing me off before this ‘almost finished’ project was finished. Somehow, she managed to stay patient (mostly) and keep me grounded (as much as anyone could) long enough for me to complete something that I have become truly passionate about. Me even being able to write this section is completely due to her support.

I would also like to thank the faculty of the SFA Geology Department for putting up with someone so stubborn and always seemingly unable to fulfill their potential. Special thanks go out to Dr. Brown for being my thesis director and his unending patience while I worked on getting a dataset, especially during the times it never seemed it would happen.

To Jim Ferry, I wouldn’t have been able to perform this study without your guidance and assistance. Like I always say, I can never thank you enough.

I am very grateful to Dr. Nielson and Dr. Musser for their willingness to be on my thesis committee and still manage to remember who I was when I finally showed up at the last second with a manuscript.

To Amy Singer and the rest of the fine folks at TGS, thank you for putting up with all the e-mails and phone calls while I was begging for seismic data. This project has been amazing and the time I spent trying to get the data was more than worth it.

Finally, I would like to thank my family for always being there for me. You know how important you are. I don't know how you've put up with me for this long.

TABLE OF CONTENTS

ABSTRACT.....	i
ACKNOWLEDGEMENTS.....	iii
LIST OF FIGURES AND TABLES.....	vii
CHAPTER 1: INTRODUCTION.....	1
1.1 Area Overview.....	1
1.2 Thesis Objectives.....	4
1.3 Research Hypotheses.....	4
1.4 Thesis Significance.....	5
1.5 Literature Review.....	6
1.5.1 Mesozoic Structural and Depositional Setting.....	6
1.5.2 Cenozoic Depositional History.....	12
1.5.3 Salt and Salt Tectonics.....	19
CHAPTER 2: METHODOLOGY.....	29
2.1 Data Acquisition.....	29
2.1.1 Digitization of Raster Logs.....	31
2.2 Geologic Interpretation.....	33
2.2.1 Paleontology Surveys.....	34

2.2.2 Well Log Curves	37
2.2.3 Log Correlation	37
2.3 Seismic Interpretation	40
2.3.1 Creation of a Synthetic Seismogram.....	40
2.3.2 Seismic Stratigraphy	42
2.3.3 Picking Horizons.....	42
2.3.4 Evaluation and Imaging of Seismic Surfaces	44
2.4 Restoration	44
CHAPTER 3: INTERPRETATION AND CONCLUSIONS.....	45
3.1 Interpretation and Results	45
3.2 Conceptual Reconstruction	83
3.3 Discussion and Conclusions	88
3.3.1 Future Recommendations	94
REFERENCES	96
Appendix A: Seismic Technical Data.....	102
Appendix B: Depisode Maps from Galloway et al (2000)	105
VITA.....	121

LIST OF FIGURES AND TABLES

Figure 1: Locator map for study area.....	2
Figure 2: Map showing the relationship of kinds of trap styles to the Neogene allochthonous salt systems.....	3
Figure 3: Structural interpretation of the Whiting Dome salt structure.....	5
Figure 4: Timing chart and stratigraphic column for Middle-Late Jurassic evolution of the Gulf of Mexico Basin.....	6
Figure 5: Areal distribution and thickness of Louann salt deposition in the Gulf of Mexico.....	7
Figure 6: Simplified stratigraphic chart for the Jurassic and Cretaceous periods of the northeastern Gulf of Mexico illustrating the formation names, ages, and facies.....	9
Figure 7: Chronology of GOM Cenozoic genetic sequences and their bounding marine shale units and paleontologic markers.....	10
Figure 8: Basin-margin structural features and principal and secondary Cenozoic sediment dispersal axes of the GOM basin.....	11
Figure 9: Explanation of symbols for paleogeographic maps.....	12
Figure 10: Paleogeographic maps of the late Paleocene and early Eocene.....	13
Figure 11: Paleogeographic maps of the late Eocene and early Oligocene.....	14
Figure 12: Paleographic maps of the Miocene.....	15

Figure 13: Paleogeographic maps of the Pliocene and Pleistocene	16
Figure 14: Paleogeographic maps of the Pleistocene	17
Figure 15: Cenozoic shelf edge positions at the termination of successive deposits.....	18
Figure 16: Model of syn-exhumation salt basin	19
Figure 17: Salt basins in the Gulf of Mexico region, showing locations of salt structures and the interpreted limit of normal oceanic crust in the basin	20
Figure 18: Tectono-stratigraphic provinces of the northern Gulf of Mexico Basin	22
Figure 19: Uninterpreted and interpreted seismic profile across an organized roho system	23
Figure 20: Counter-regional salt feeder and associated fault systems	24
Figure 21: Reconstruction of a depth section from the northeastern Gulf of Mexico	25
Figure 22: Seismic line showing flip-flop salt tectonics.....	27
Figure 23: Visualization of structural differences between pre-, syn-, and post-raft tectonic depositional phases.....	28
Figure 24: Well locations.....	29
Table 1: Well information.....	30
Figure 25: Example of a raster log that has not been digitized.....	32
Table 2: List of wells and the specific logs that were digitized for this study.....	33
Figure 26: MMS Biostratigraphic chart.....	35

Table 3: Biostratigraphic markers and associated chronozones.....	36
Figure 27: Gamma ray log overlain on time domain seismic data	38
Figure 28: Simple log correlation across various well logs using gamma ray logs and paleodata	39
Figure 29: Right: Synthetic seismogram generator in Kingdom 15. Left: Synthetic seismogram with paleomarkers overlain on time domain seismic data.....	41
Figure 30: Example of a horizon and associated grids	43
Figure 31: Legend for seismic block and line interpretation in Chapter 3.	45
Figure 32: Location of interpreted arbitrary seismic lines shown in Chapter 3.....	46
Figure 33: Uninterpreted and interpreted, north oriented 3D reflection seismic block.....	48
Figure 34: Uninterpreted and interpreted, south oriented 3D reflection seismic block.....	49
Figure 35: North oriented uninterpreted and interpreted block model showing interior of Whiting Dome minibasin.....	50
Figure 36: Computer generated grids for top and bottom allochthonous salt.....	51
Figure 37: Three dimensional representations of top and bottom allochthonous salt.....	52
Figure 38: TopK horizon map and picks	54
Figure 39: MUM horizon maps and picks	56

Figure 40: Non-balanced reconstruction of seismic line perpendicular to salt flow through main feeder	57
Figure 41: Dip oriented and strike oriented interpreted 2D seismic lines showing fault dip orientation outboard of the Whiting Dome	58
Figure 42: MLU horizon maps and picks	59
Figure 43: MUU2 horizon maps and picks.....	61
Figure 44: MUU1 horizon maps and picks.....	63
Figure 45: PL horizon maps and picks	65
Figure 46: Collision of gliding Whiting Dome into expanding Mitchell Dome.....	66
Figure 47: Cross-section of western and eastern sub-basins with the Whiting Dome minibasin.....	67
Figure 48: Whiting Dome minibasin suprasalt PL maps	68
Figure 49: Dip oriented line through the center of the western sub-basin within the Whiting Dome minibasin.....	69
Figure 50: Dip oriented line through the center of the eastern sub-basin within the Whiting Dome minibasin.....	69
Figure 51: PU horizon maps and picks	70
Figure 52: Time structure and thickness map of suprasalt PUL deposits.....	71
Figure 53: Transtensional zone along western flank of the Whiting Dome salt structure.....	72
Figure 54: Thickness map of suprasalt PUU deposits in Whiting Dome structure.	73

Figure 55: Intratal failure along top PUU in multiple zones of the study area	74
Figure 56: PLL horizon maps and picks	76
Figure 57: PLM horizon maps and picks	78
Figure 58: PLU horizon maps and picks.....	79
Figure 59: Crestal fault system above diapir structure near proximal end of Whiting Dome.....	80
Figure 60: HOL horizon maps and picks	82
Figure 61: Current composition of Whiting Dome salt structure	83
Figure 62: Salt structure at the end of the Calabrian (PLL).....	83
Figure 63: Salt structure at the end of the Gelasian (PUU)	84
Figure 64: Salt structure at the end of the Piacenzian (PUL)	84
Figure 65: Salt structure at the end of the Miocene (MUU1).....	85
Figure 66: Salt structure at the end of the Zancian (PL).....	85
Figure 67: Salt structure at the end of the Upper Serravallian (MUM)	86
Figure 68: Salt structure at the end of the Maastrichtian (TopK)	86
Figure 69: Salt structure at the end of the Callovian (Louann).....	87
Figure 70: Time slice of Fault Attribute data generated from 3D PSTM reflection seismic block.....	89
Figure 71: Structural interpretation of time slice using Fault Attribute data (edge detection cube).....	90

Figure 72: Strike oriented stratigraphic interpretation and interpretation of depocenter shifts of supra salt strata near the center of the Whiting Dome minibasin.....	91
Figure 73: Uninterpreted and interpreted dip line from proximal end of salt structure through western sub-basin in minibasin portion of Whiting Dome.....	93
Figure 74: Salt tectonic and depositional phases of western sub-basin of minibasin portion of Whiting Dome salt structure	94
Figure 75: Full extent of MC Revival seismic survey by TGS with study area shown in purple rectangle.	102
Figure 76: Acquisition specifications for MC Revival seismic survey	103
Figure 77: Processing sequence and deliverables for the MC Revival seismic survey.....	104
Figure 78: Explanation of symbols for paleogeographic maps.	105
Figure 79: Paleogeography of the Lower Wilcox depisode (61-56.4 Ma)	106
Figure 80: Paleogeography of the Upper Wilcox depisode (48.5-54.5 Ma).....	107
Figure 81: Paleogeography of the Queen City depisode (47.5-44.5 Ma)	108
Figure 82: Paleogeography of the Yegua/Cockfield depisode (38.5-35 Ma)	109
Figure 83: Paleogeography of the early Frio/Vicksburg depisode (32.6-28 Ma).....	110
Figure 84: Paleogeography of the late Frio/Vicksburg (28-25 Ma)	111
Figure 85: Paleogeography of the first early Miocene depisode (25-18 Ma).....	112
Figure 86: Paleogeography of the middle Miocene depisode (15.6-12 Ma)	113

Figure 87: Paleogeography of the late Miocene depisode (12-6.4 Ma).....	114
Figure 88: Paleogeography of the Buliminella 1 depisode (6.4-4.2 Ma).....	115
Figure 89: Paleogeography of the Globoquadrina altispira depisode (4.2-3.1 Ma).....	116
Figure 90:Paleogeography of the Lenticulina 1 depisode (3.1-2.3 Ma)	117
Figure 91: Paleogeography of the early phase of the Angulogerina B depisode (2.3-2 Ma)	118
Figure 92: Paleogeography of the Sangamon depisode (0.6-0.1 Ma).....	119
Figure 93: Temporal distribution of volumetrically important Cenozoic depositional systems of the northern Gulf basin and major tectonic phases affecting North American and adjacent Mexican sediment source areas.....	120

CHAPTER 1: INTRODUCTION

1.1 Area Overview

The Gulf of Mexico (GOM) is one of the most productive petroleum producing regions in the world. According to the U.S. Energy Information Administration (2015), as of 2014, proven crude oil reserves from discoveries in the GOM have surpassed 4.7 billion barrels. Deep-water discoveries (defined as anything in water that is deeper than 200 meters) are roughly equivalent to 82 percent of all proven crude oil reserves in the GOM. A large majority of these fields are being produced out of Cenozoic formations both above and below the allochthonous salt sheet. This study focuses on the north-central Mississippi Canyon and southern Viosca Knoll protraction areas, located off the coast of Louisiana, approximately 150 miles southeast of New Orleans, and due south of the Mississippi coastline. The Mississippi Canyon protraction area has been an extremely prolific petroleum zone throughout the stratigraphic column (Weimer and Bouroullec, 2013). It is home to one of the largest deep-water fields in the GOM (Thunder Horse - approximately 100 kilometers due south of the study area), the infamous Macondo prospect (known better as the site of the Deepwater Horizon spill), the Pliocene and Miocene Mars-Ursa mini-basin fields, and recent discoveries by Shell in raft structures containing highly productive Norphlet Formation reservoirs (Weimer and Bouroullec, 2013).

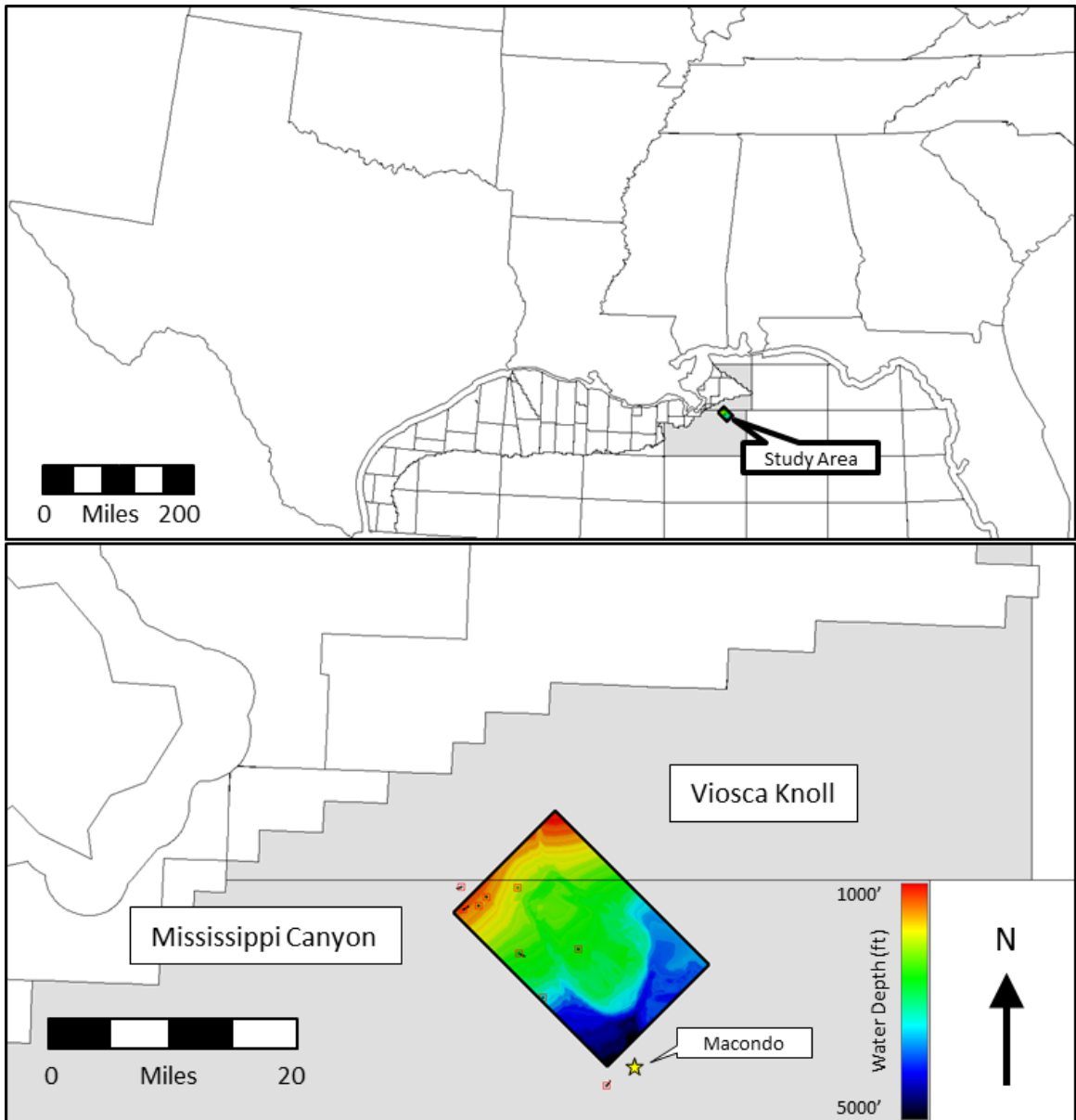


Figure 1: Locator map for study area. Viosca Knoll and Mississippi Canyon protraction areas highlighted in light gray. Study area represented by current sea floor bathymetry map generated using 3D seismic data.

The study area straddles the boundary of the Viosca Knoll and Mississippi Canyon Outer Continental Shelf (OCS) protraction areas (Figure 1), enveloping 243.5 square miles. The northern apex terminates at the intersection of Viosca Knoll (VK) blocks 904,

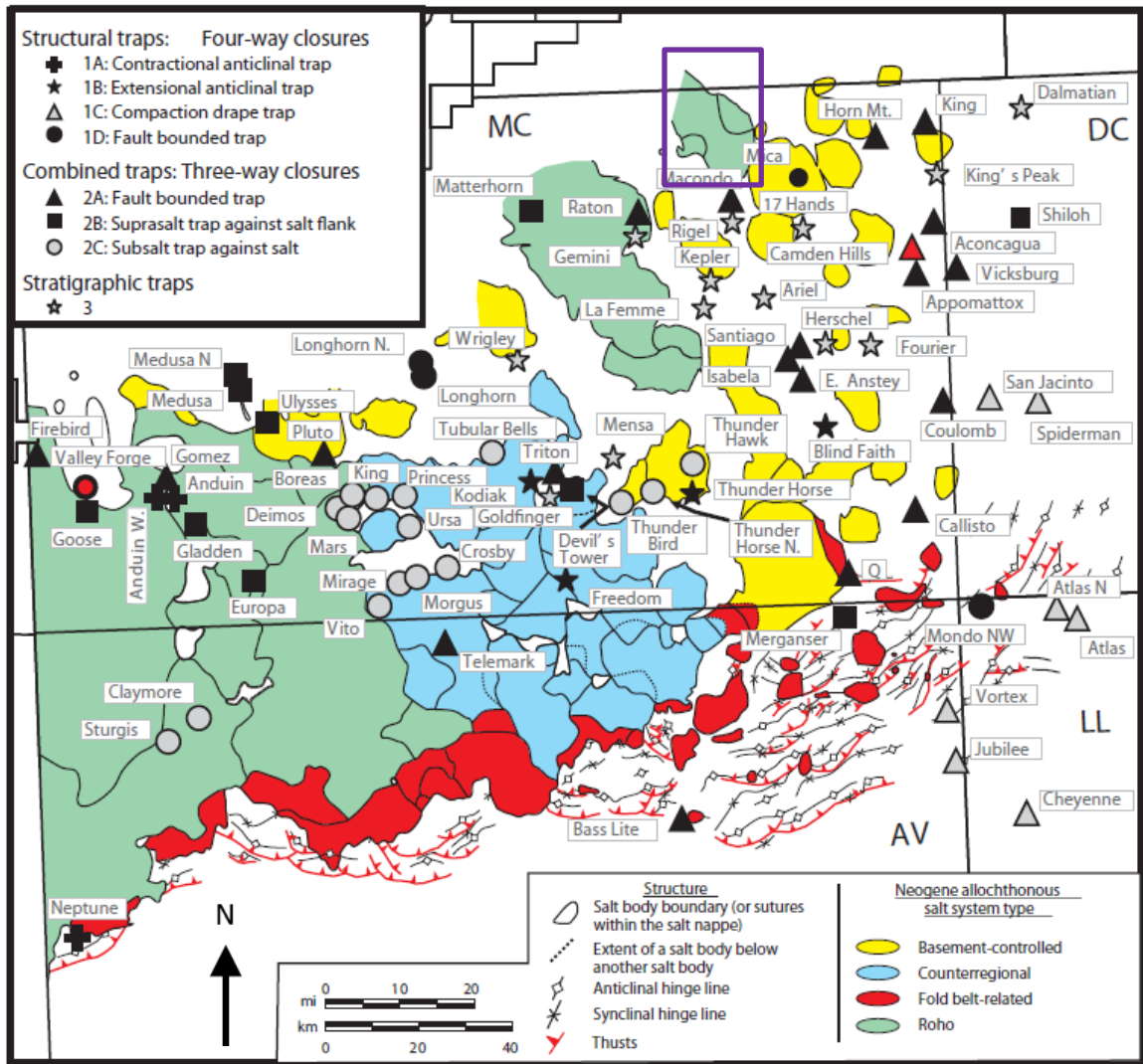


Figure 2: Map showing the relationship of kinds of trap styles to the Neogene allochthonous salt systems. General location of study area highlighted by purple box. Eight kinds of traps are recognized. Modified from Weimer and Bouroullec (2013).

905, 948, and 949; the western at the intersection of Mississippi Canyon (MC) blocks 27, 28, 71, and 72; the eastern in MC 123; and the southern in MC 252, approximately 1.3 miles west of the original Macondo borehole. While the entire GOM is structurally complex, overwhelmingly due to the underlying salt tectonics, the Mississippi Canyon area encompasses a larger and more comprehensive range of salt structure regimes than

any other GOM OCS (Figure 2). While most areas in the GOM basin are dominated by one or two salt structure types, the Mississippi Canyon area has no less than four.

1.2 Thesis Objectives

This study has two major objectives:

- 1. Interpret the seismic stratigraphy of the area.*
- 2. Reconstruct the structural evolution of the salt structure and its effect on the surrounding strata through time.*

Secondary objectives include determining the effect of salt tectonics on Pliocene and overlying strata, the correlation and subsequent interpretation of any available well logs in the area. These objectives are broadly defined by a set of questions that should be answered through the completion of this study:

- 1. How has differential loading affected the mobilization of the underlying allochthonous salt sheet?*
- 2. How has salt mobilization affected the structural and depositional setting of the overlying strata?*

1.3 Research Hypotheses

- 1. Progradation of sediment created a salt expulsion and rollover structure.*
- 2. Mobilization of salt created accommodation space for continuing infill.*
- 3. Infilling lead to unequal distribution of sediment load across salt forcing salt to move further basinward.*

4. *Older sediments within mini-basin area of salt structure became detached from host strata and migrated basinward along salt similar to the rafting events found in the Mississippi Canyon OCS Norphlet plays and the Kwanza Basin, Angola.*

1.4 Thesis Significance

Despite an immense amount of scientific research and corresponding literature in the Gulf of Mexico over the past century, no site-specific study has been published on the salt tectonics and evolution of the Whiting Dome. In fact, no site-specific published study has been performed on the Whiting Dome in any aspect. Minor analysis of the Whiting Dome has only appeared briefly in a paper by Peel et al. (Figure 3) (1995) and is referenced in a study as a possible analog

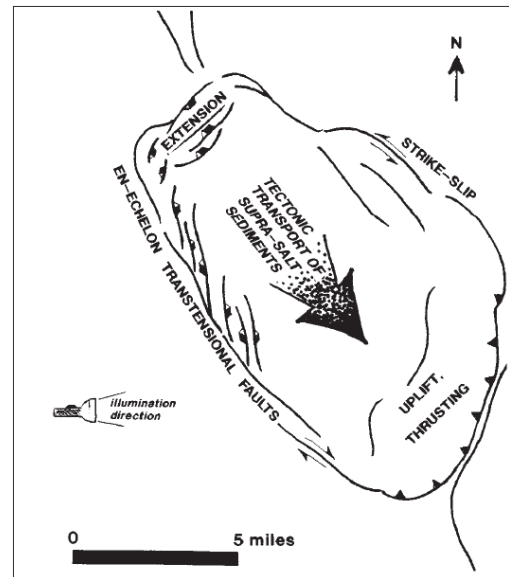


Figure 3: Structural interpretation of the Whiting Dome salt structure. This is the only piece of literature that directly references even minimal analysis of the Whiting Dome. From Peel et al. (1995)

for a surface feature on Mars (Andrews-Hanna, 2009). There is, however, a published study on the salt structure due southeast of the Whiting dome. That structure, the Mitchell Dome, has several similarities to the structure and evolution of the Whiting Dome (Fletcher et al., 1995).

This work will contribute to the understanding of salt tectonics and their effects on sediment deposition, especially in the Gulf of Mexico basin. In a localized sense, this study will assist in the evaluation and classification of a highly complex salt structure that does not truly fit in any of the standard salt structure classification systems.

1.5 Literature Review

The following information was researched using a variety of sources in order to enable an accurate interpretation of the data through increased knowledge of the region.

1.5.1 Mesozoic Structural and Depositional Setting

The breakup of Pangaea in the Late Triassic and Early Jurassic created a “divergent margin basin characterized by extensional rift tectonics and wrench faulting” (Mancini and Puckett, 2002) between the Yucatan Microplate and the North American plate (Hudec et al., 2013). In the Middle Jurassic, continued rift tectonics led to the development of multiple basins within the larger GOM basin and widespread deposition of the Louann Salt

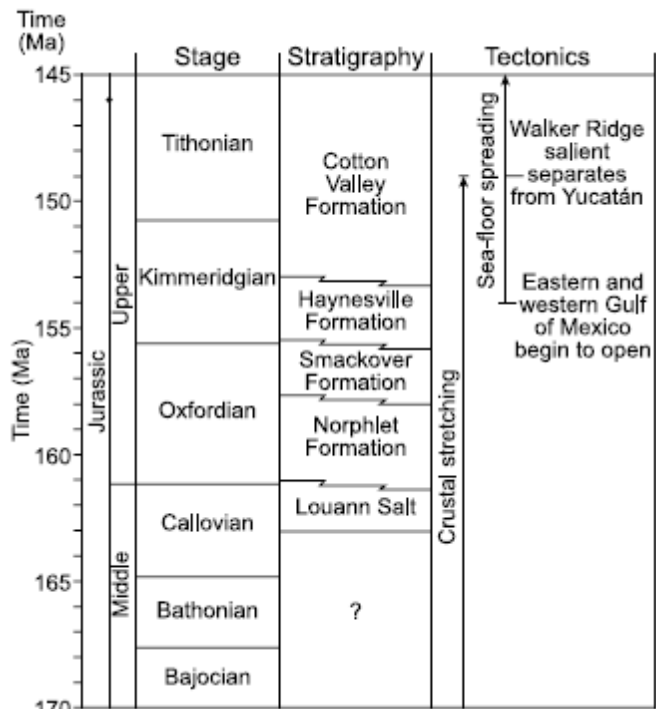


Figure 4: Timing chart and stratigraphic column for Middle-Late Jurassic evolution of the Gulf of Mexico Basin. From Hudec et al (2013).

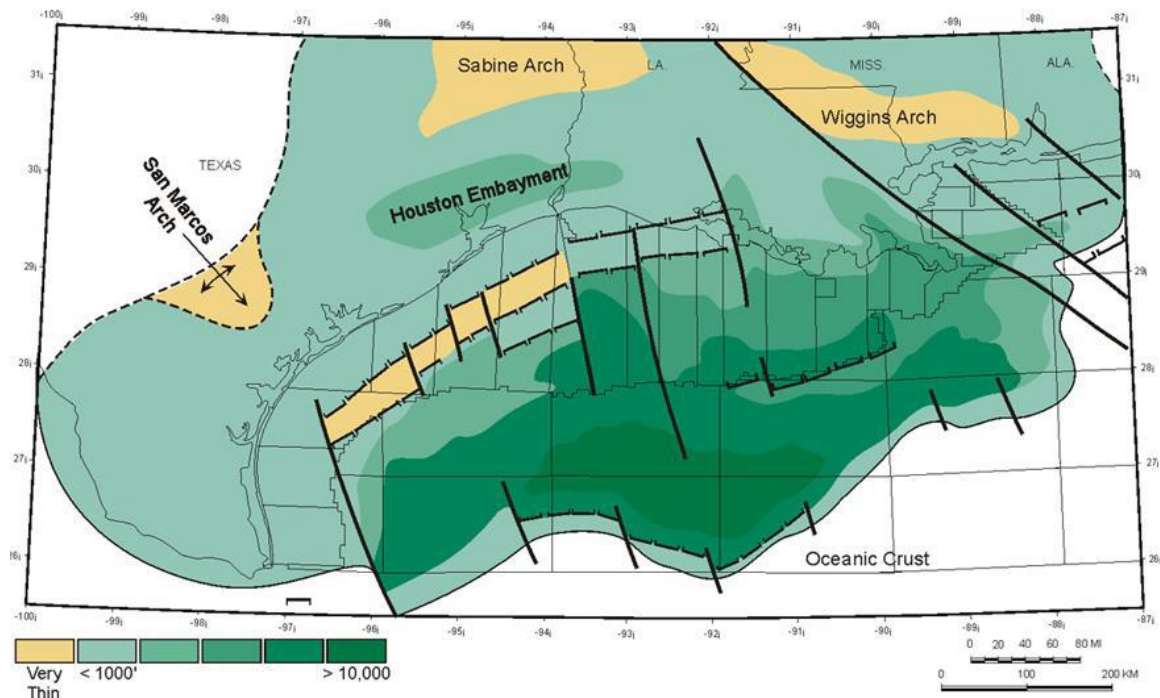


Figure 5: Areal distribution and thickness of Louann salt deposition in the Gulf of Mexico, From Karlo and Shoup (2000).

(Figure 4) (Mancini and Puckett, 2002; Karlo and Shoup, 2000). This expansive layer of salt created an extremely complex structural setting throughout the basin and will be discussed in more detail later in this study. Late Jurassic basinal subsidence (thermal and isostatic) was accompanied by a regional marine transgression (Mancini and Puckett, 2002) that resulted in the deposition of the Norphlet eolian dune facies, Smackover carbonate and marine sequences, and Cotton Valley sand and carbonate sequences (Figure 5) (Todd and Mitchum, Jr., 1977).

The middle Cretaceous (Valanginian) is marked by an extensive erosional period. This was followed in the Upper Cretaceous by several transgressive-regressive sequences. The first such sequence consisted of the Houston Formation, “marine

interbedded sandstone, calcareous shale, and interbedded limestone and shale,” and Sligo Formation, “marine shelf and reef limestone,” and was deposited in what is currently east Texas and Louisiana. The next sequence Pearsall Formation consisting of a shale-limestone-marine shelf lime mudstone and shale sequence, Glen Rose limestone-anhydrite-carbonate and carbonaceous shale, Fredericksburg Group siliciclastics and carbonaceous shales, and Washita Group limestones (Todd and Mitchum, Jr., 1977).

The Upper Cretaceous is mostly defined by shallow marine siliciclastics and carbonaceous units including the Woodbine Formation, Eagle Ford Shale, Austin Group, Taylor Group, and Navarro Group (Louisiana Geological Survey, 2000).

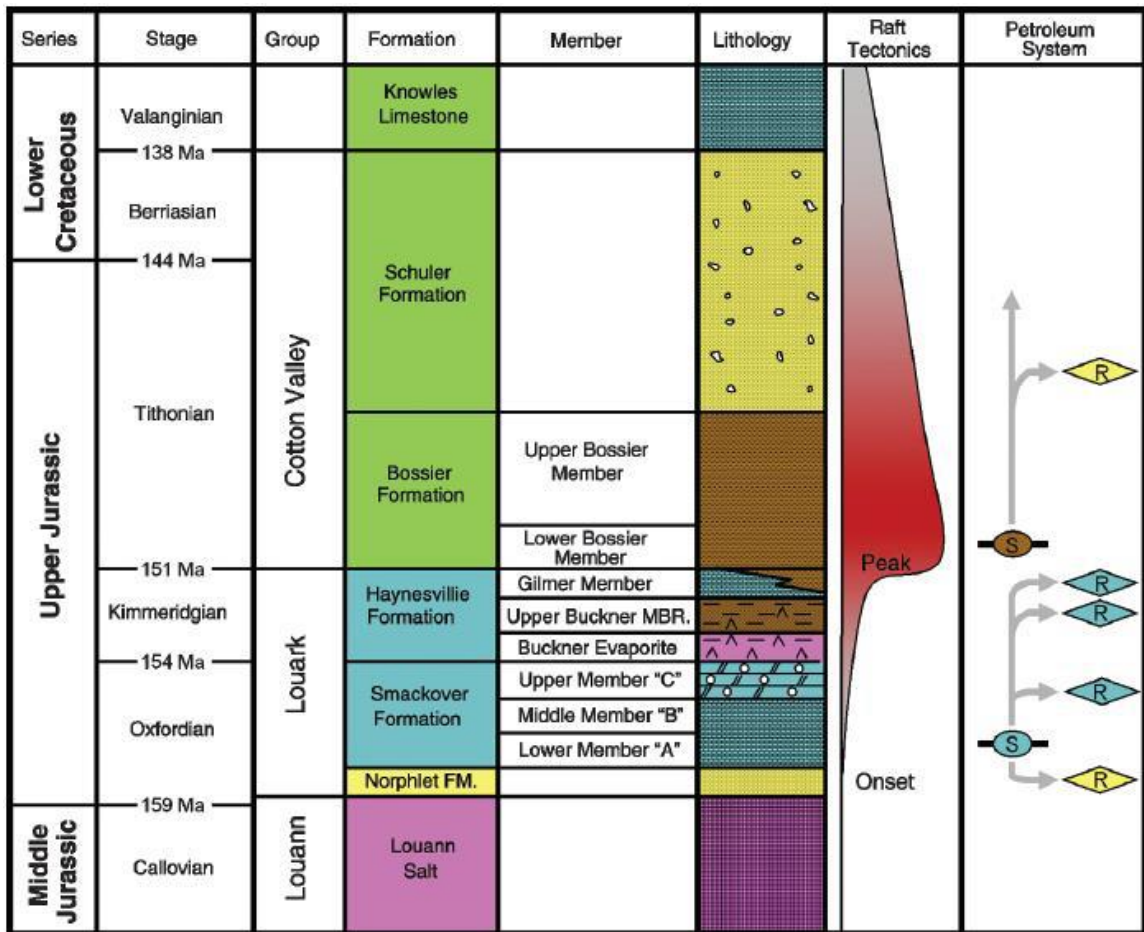


Figure 6: Simplified stratigraphic chart for the Jurassic and Cretaceous periods of the northeastern Gulf of Mexico illustrating the formation names, ages, and facies. Lithologies are colored blue for carbonates, yellow/brown for siliciclastics, and pink for evaporates. The timing of raft tectonics and key petroleum system elements are illustrated: S = source rocks, R = reservoirs, and the arrows indicate the charge. From Pilcher et al (2014).

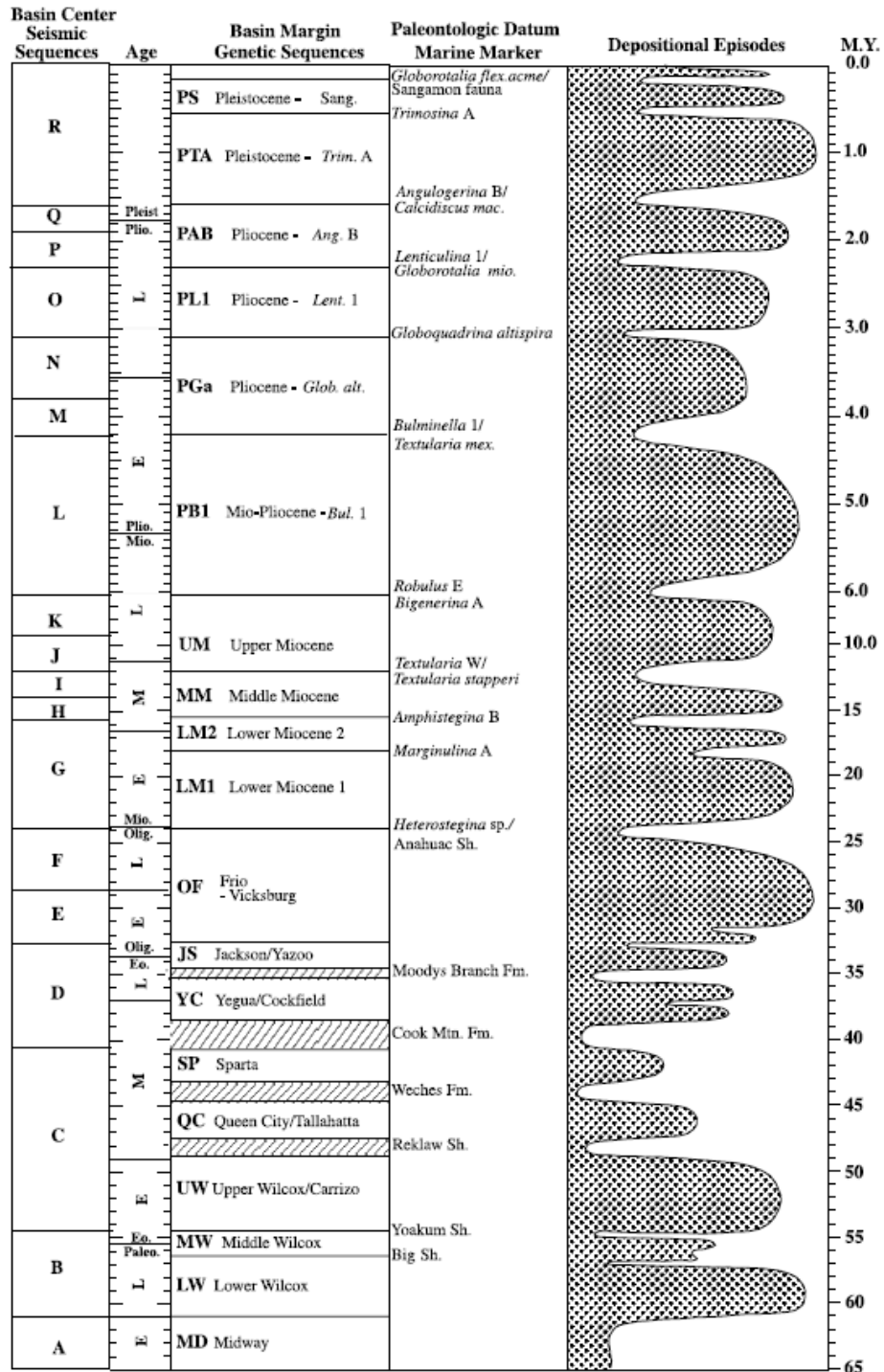


Figure 7: Chronology of GOM Cenozoic genetic sequences and their bounding marine shale units and paleontologic markers. From Galloway et al (2000).

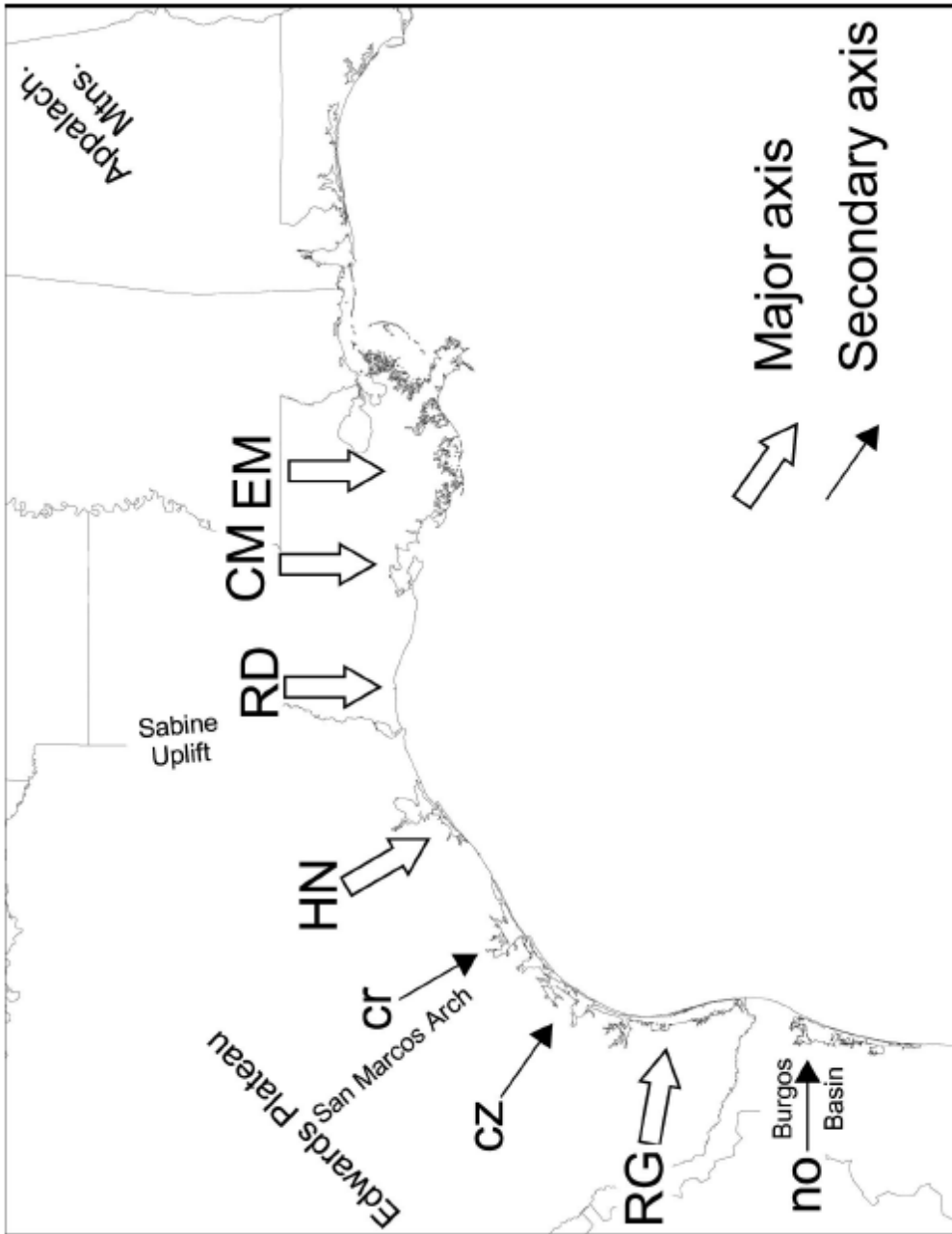


Figure 8: Basin-margin structural features and principal (caps) and secondary (lower case) Cenozoic sediment dispersal axes of the GOM basin: no = Norias; RG = Rio Grande; cz = Carrizo; cr = Corsair; HN = Houston; RD = Red River; CM = Central Mississippi, EM = Eastern Mississippi. From Galloway et al. (2000).

1.5.2 Cenozoic Depositional History

Galloway et al. (2000) divide Cenozoic deposition in the GOM into 24 distinct depositional episodes (23 labeled with Holocene unlabeled) (Figure 7). Depositional episodes (deposides) from the early Paleocene to late Oligocene are defined based on commonly accepted stratigraphic nomenclature and marine flooding horizons, whereas early Miocene to recent deposides are demarcated paleontologically. The major Gulf of Mexico depositional axes can be seen in Figure 10. A legend of symbols for the paleogeographic maps in this section can be seen in Figure 11. Unmodified versions of the paleographic maps in this section can be seen in Appendix B.

The first major influx of Cenozoic clastic sediment in the GOM is comprised of the Paleocene-Eocene aged Wilcox Group. The Lower Wilcox (Figure 10A) deposide lasted approximately 5.5 million years (61-56.4 Ma) (Galloway et al.,

2000). Sediment supply for this sequence was primarily sourced from Laramide uplands



Figure 9: Explanation of symbols for paleogeographic maps. From Galloway et al. (2000).

that fed the western and Mexico portions of the GOM; however, the northern GOM seems to have been sourced by sediments arriving through a precursor to the Central Mississippi major axis at the Holly Springs delta (Galloway et al., 2000).

The relatively short Middle Wilcox depisode is bounded by the Big Shale and Yoakum transgressions and is followed by the much larger Upper Wilcox/Carrizo depisode (Figure 10B) which is in turn topped by the Reklaw Shale (Galloway et al., 2000). According to Galloway et al.'s (2000) paleogeographic reconstructions, the study area ranged from being in a starved basin during the Lower Wilcox depisode to a basin floor depositional environment in the Upper Wilcox.

Following the deposition of transgressional Reklaw Shale, the Queen City Formation, Weches Formation, and Sparta Formation rounded out the middle Eocene. During the Queen City depisode (Figure 10C), the western GOM was dominated by a sand-rich shore zone along the Norma and Rio Grande axes while incorporating the muddy shelf of

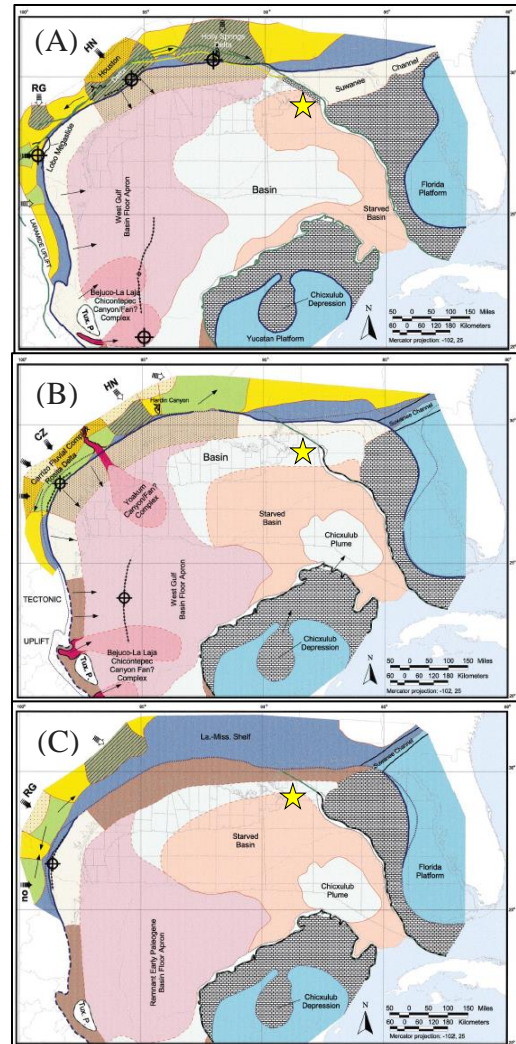


Figure 10: Paleogeographic maps of the late Paleocene and early Eocene. Study area represented by yellow star. (A) Lower Wilcox (B) Upper Wilcox (C) Queen City. Modified from Galloway, 2000. Modified from Galloway et al. (2000).

the fluvial-dominated delta system in the Houston embayment (Galloway et al., 2000). In the eastern GOM, the Suwanee channel divided the Louisiana-Mississippi clastic shelf and the Florida carbonate platform (Galloway et al., 2000). During the deposition of the Sparta Formation, the Central Mississippi fluvio-deltaic axis, while relatively small, became active for the first time since deposition of the Lower Wilcox (Galloway et al., 2000). This was accompanied by a large muddy shelf and small sandy shore-zones in the northeastern GOM, laterally extensive wave-dominated strand-plain/barrier complexes from northern Mexico to the Houston embayment, and a muddy perched ramp that did not reach the relict shelf margin (Galloway et al., 2000). Due

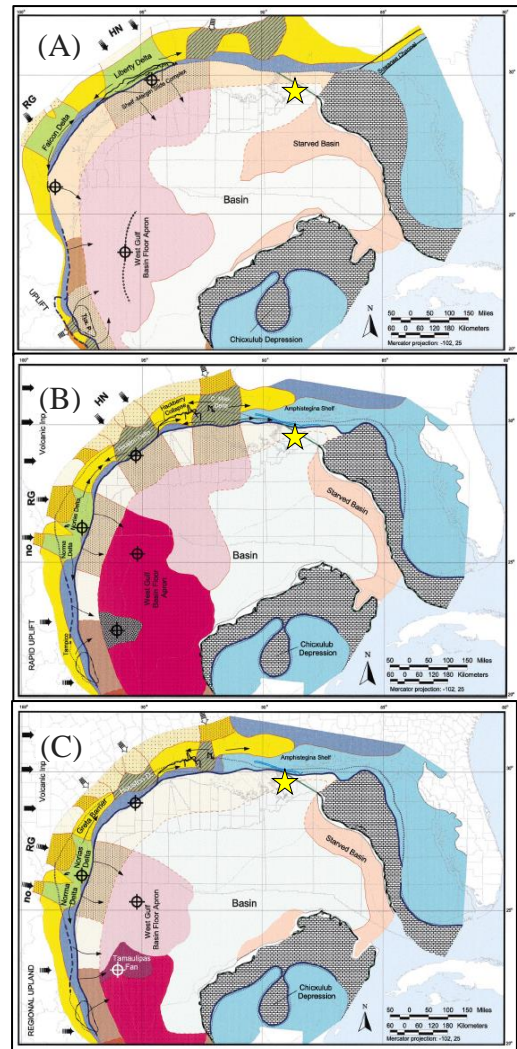


Figure 11: Paleogeographic maps of the late Eocene and early Oligocene. Study area represented by yellow star. (A) Yegua/Cockfield (B) Early Frio/Vicksburg (C) Late Frio/Vicksburg. Modified from Galloway, 2000.

to the relatively low sediment influx during this period, the study area most likely fluctuated between a starved basin and basin floor setting.

During the late Eocene, large Houston and Rio Grande axis sand rich deltas dominated the northwest GOM while smaller platform deltas prograded into the central

GOM and the eastern GOM consisted of a broad sand shore trending into a muddy shelf (Galloway et al., 2000). Due to uplift of the Mexican Cordillera and associated western GOM margins, regional depositional patterns morphed with active deposition occurring further east into the basin during the Yegua/Cockfield depisode (Figure 11A) than previously seen (Galloway et al., 2000). The Eocene closed with a short transgressive flooding, Moodys Branch Formation, and the Jackson depisode which was focused primarily in the northwest GOM and did not extend the shelf past that of the Yegua depisode (Galloway et al., 2000).

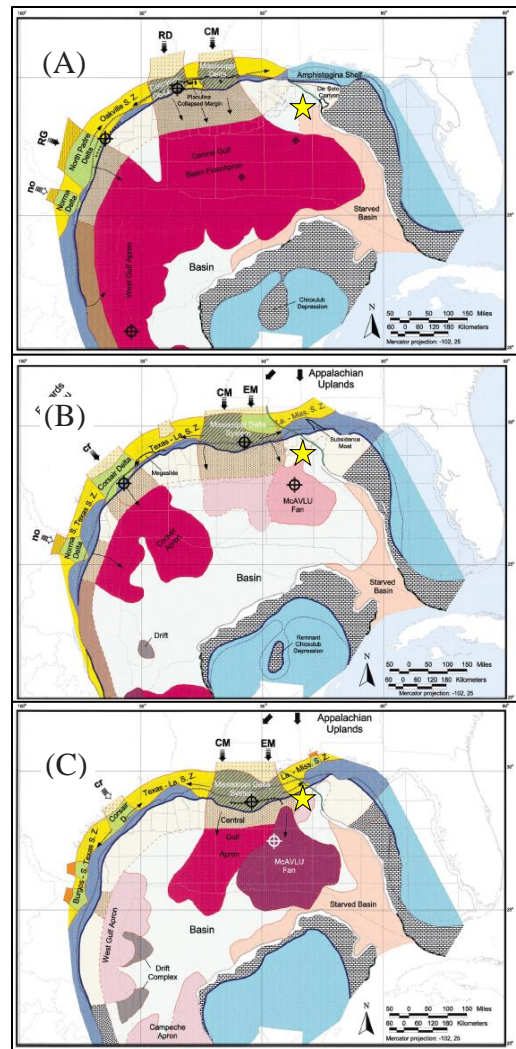


Figure 12: Paleographic maps of the Miocene. Study area represented by yellow star. (A) Early Miocene (B) Middle Miocene (C) Late Miocene. Modified from Galloway et al. (2000).

Early Oligocene Frio-Vicksburg deposition (Figure 11B) occurred most markedly in the western GOM, slowly losing potency moving away both northeast and south from the Rio Grande axis (Galloway et al., 2000). Galloway et al. (2000) describe the end of the depisode (Figure 11C) as a “long term systems tract retreat”, especially in the Houston and Mississippi delta areas, leaving only

muddy basin floor deposits in the study area and culminating in the transgressive Anahuac Shale.

The early Miocene (Figure 12A) was met with increased sediment influx and shifting depocenters due to a redistribution of drainage patterns across western North America caused by the onset of Basin and Range extension (Galloway et al., 2000). The Central Mississippi and Red River axes become the major importers of sediment into the GOM; enough sediment is dispersed that the basin floor apron extends to the toe of the Yucatan Peninsula for the first time (Galloway et al., 2000). However, the Mississippi Delta system had not shifted far enough east through the early Miocene to fill the study area with anything but muddy basin floor deposits.

The middle Miocene (Figure 12B) marks the emergence of the Eastern Mississippi dispersal axis; along with the Central Mississippi axis, the central GOM shelf margin is prograded up to 40 km while creating the McAVLU submarine fan (Mississippi Canyon,

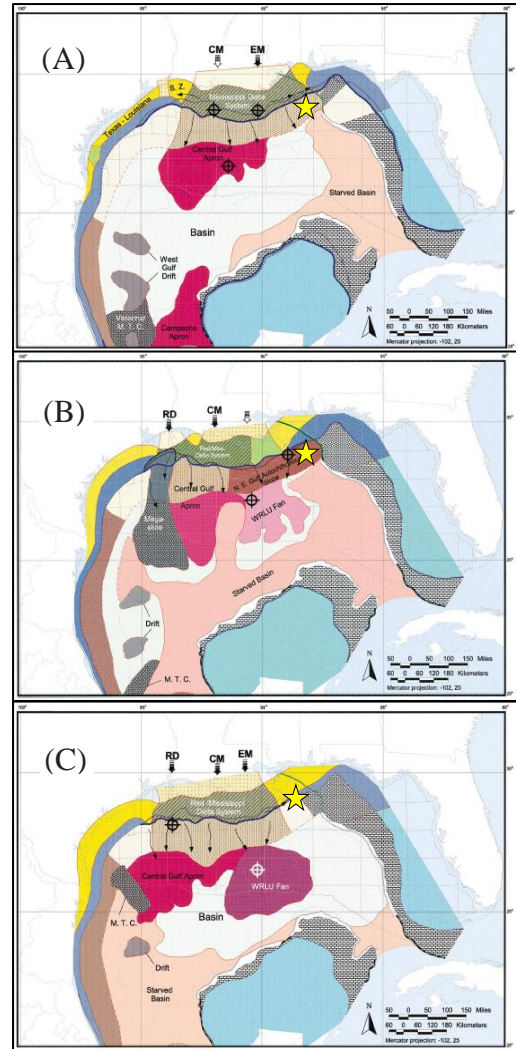


Figure 13: Paleogeographic maps of the Pliocene and Pleistocene. Study area represented by yellow star. (A) *Buliminella 1*, Mio-Pliocene (B) *G. altispira*, mid-Pliocene (C) *Lenticulina 1*, late Pliocene. Modified from Galloway et al. (2000).

Atwater Valley, Lund outer continental shelf areas) (Galloway et al., 2000). The McAVLU submarine fan is the first depocenter/non-basin floor deposition within the study area during the Cenozoic.

Stable sediment dispersal patterns define the upper Miocene depisode (Figure 12C); during this period, the finalization of the decline of major influx in the northwestern GOM occurs and the Eastern and Central Mississippi axes merge into a composite delta (Galloway et al., 2000). With the shelf margin

having been prograded anywhere from 40-80 km in the region, the study area is apparently dominated by the Mississippi Delta and delta fed apron.

As at the end of the Miocene, early Pliocene deposits tend to be localized to the central GOM; however, the Central Mississippi axis/delta became the dominate axis and was flanked by the subordinate Red River and Eastern Mississippi axes (Galloway et al., 2000). The study area was undergoing delta retreat and thereby is characterized by retrograding slope, wave-dominated delta, and shore-zone facies.

By the end of the Pliocene, glacial reorganization of drainage networks in central and eastern North America increased the drainage basin of the Mississippi axes (Figure 13)

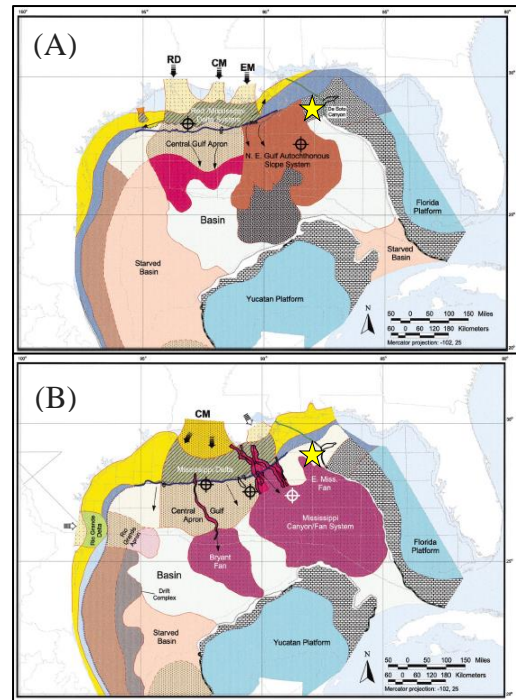


Figure 14: Paleogeographic maps. Study area represented by yellow star. (A) Anglulogerina B, Pleistocene (B) Sangamon, Holocene. Modified from Galloway et al. (2000).

(Galloway et al., 2000). The first phase of the modern Mississippi fan system has its roots during this time period; this system is initiated by small canyon creation (Prather et al., 1998). The study area is dominated by siliciclastic shelf and retrogradational apron deposits.

The Pleistocene was marked primarily by high-amplitude sea level fluctuations due to associated glacial cycles resulting in frequent shoreline shifts of tens to hundreds of miles (Figure 14) (Galloway et al., 2000). This led to significant shelf edge progradation and extensive submarine canyon incision (Galloway et al., 2000).

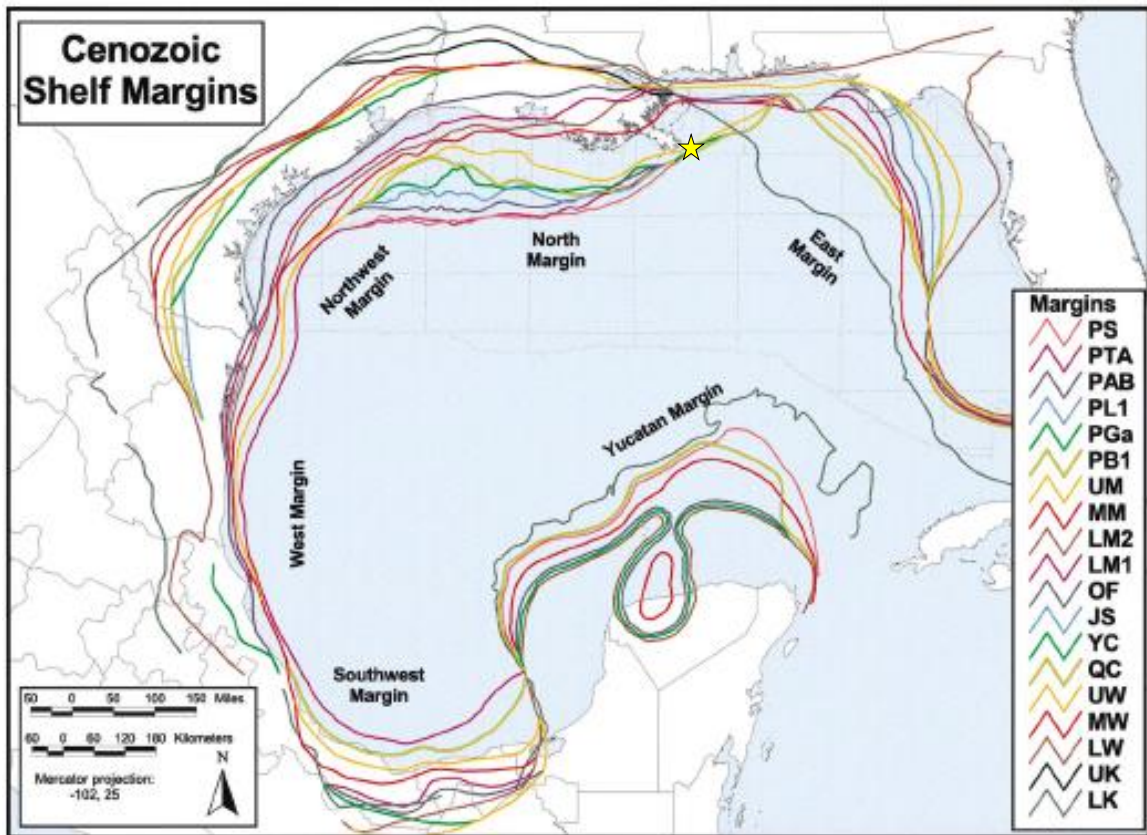


Figure 15: Cenozoic shelf edge positions at the termination of successive depositional episodes. Study area represented by yellow star. Modified from Galloway et al (2000).

1.5.3 Salt and Salt Tectonics

In the GOM basin, as is often the case globally, salt “includes all rock bodies composed primarily of halite” (Hudec and Jackson, 2007). Over the extent of Earth’s surface, there are over 130 individual salt basins that fall into four major categories based on the tectonic setting of the basin in which deposition occurs: collisional, passive-margin, synrift, and cratonic (Hudec and Jackson, 2007). The GOM basin falls into the

passive-margin classification. Within this tectonic setting, salt basins are classified as prerift, syn-stretching, syn-thinning, and syn-exhumation (Rowan, 2014). According to Rowan (2014), the GOM basin has typically been classified as a syn-stretching to syn-thinning basin; however, he posits that due to evidence of allochthonous salt overlying

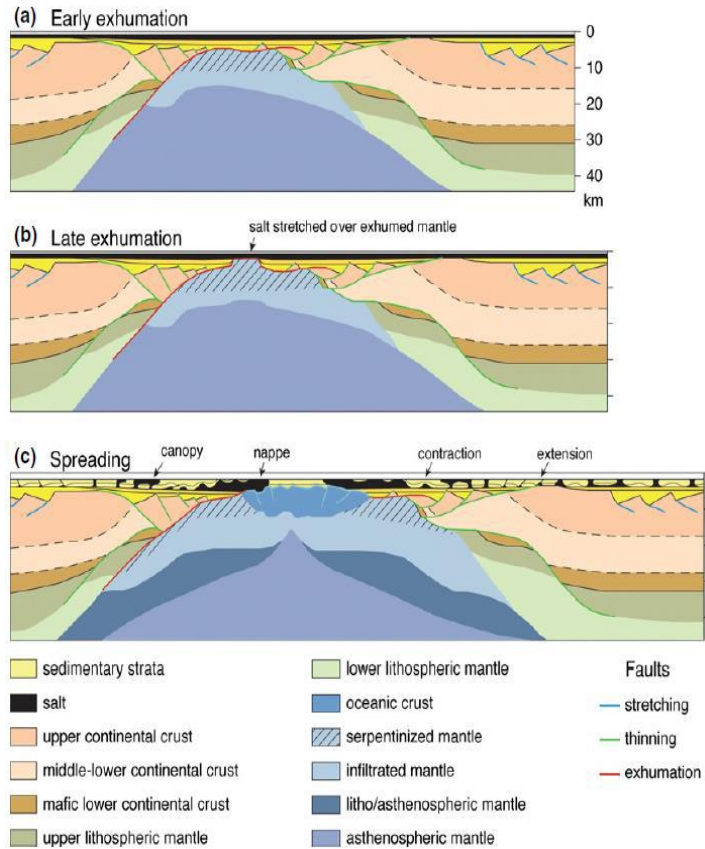


Figure 16: Model of syn-exhumation salt basin: (a) early exhumation stage with deposition of sag basin (orange) and salt after almost all crustal faulting has ceased, so that there is little offset of the base salt; (b) late exhumation stage with separation of synrift and sag sequences and salt attenuation over newly exhumed mantle; (c) spreading stage and development of thin-skinned deformation due to gravitational failure of the margin. Note that although serpentinized mantle is shown, it is also possible that distal salt is deposited over volcanic crust. From Rowan (2004).

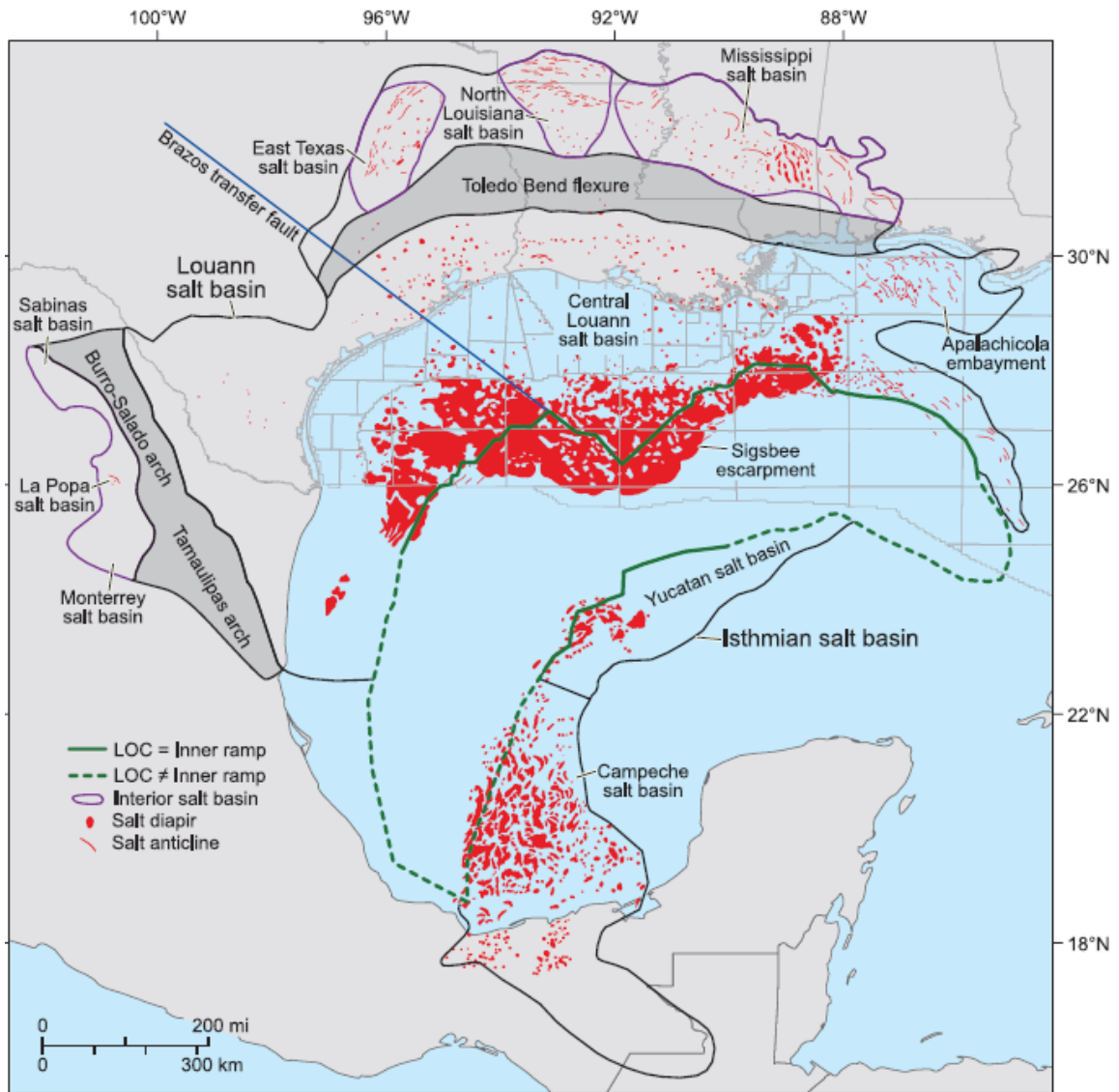


Figure 17: Salt basins in the Gulf of Mexico region, showing locations of salt structures and the interpreted limit of normal oceanic crust in the basin. From Hudec et al (2013a).

portions of the oldest oceanic crust in the GOM as well as a lack of faults in base salt basinwide it is a syn-exhumation salt basin (Figure 16).

The complexity of salt influenced basins arises due primarily to the propensity of salt to react to overburden similarly to a buoyant, dense liquid (Ge et al., 1997; Hudec

and Jackson, 2007; Warsitzka et al., 2014). Hudec and Jackson (2007) summarize the mobilization of salt, thusly:

The primary driving force for salt tectonics is differential loading, which may be induced by gravitational forces, by forced displacement of one boundary of a salt body relative to another, or by a thermal gradient. Buoyancy, long considered a key driver for salt tectonics, is of secondary importance in many settings. Two factors resist salt flow: strength of the overburden and boundary drag along the edges of the salt body. Salt will move only if driving forces exceed the resistance to flow.

These concepts have been scientifically substantiated through a multitude of seismically based kinematic restorations (*examples:* (Broussard and Sarwar, 2014; Brun and Fort, 2011; Fletcher et al., 1995; Duval et al., 1992; Ge et al., 1997)) and analogue experiments (*examples:* (Warsitzka et al., 2014; Ge et al., 1997)).

As mentioned earlier, the Louann Salt was deposited in the late Jurassic and covered an expansive area (Figure 17). Due to differential loading throughout the basin, the salt has been redistributed into multiple structural systems. Diegel et al. (1995) define eight tectono-stratigraphic provinces (Figure 18) that formed because of, or in conjunction with, salt and/or shale mobilization:

- 1. A contractional foldbelt province at the toe of slope*
- 2. A tabular salt-minibasin province on the slope*
- 3. A Pliocene-Pleistocene detachment province on the outer shelf*

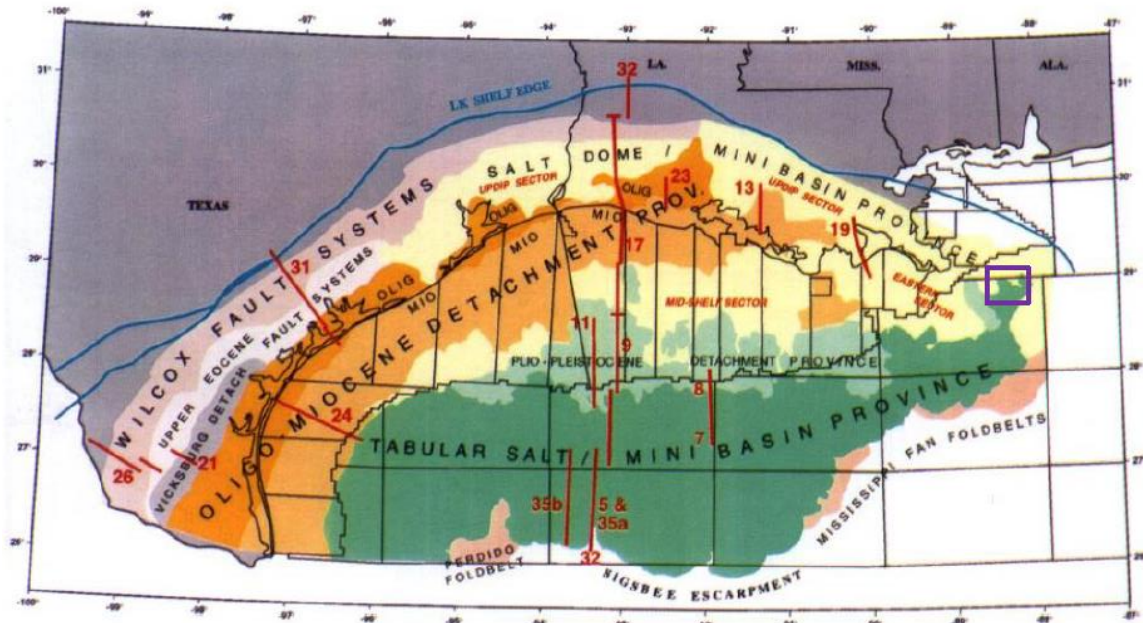


Figure 18: Tectono-stratigraphic provinces of the northern Gulf of Mexico Basin. Purple Box represents general location of the study area. Modified after Diegel et al. (1995).

4. A salt dome-minibasin province
5. An Oligocene-Miocene detachment province onshore and on the shelf
6. An Oligocene Vicksburg detachment province onshore Texas
7. An upper Eocene detachment province
8. The Wilcox growth fault province of Paleocene-Eocene age

Using these divisions as defined by Diegel et al. (1995), the study area is assigned to the tabular salt-minibasin province. However, recent work would suggest that the salt structure in question more closely resembles a Roho structure (Figure 19) and should be classified as part of province 3 (Karlo and Shoup, 2000; Bouroullec et al., 2004; Weimer and Bouroullec, 2013). Karlo and Shoup (2000) define a Roho structure as a

“combination [of] gravity slides and salt withdrawal structures formed in response to the progradation of shelf sediments onto a salt wing.” The main salt structure in the study area also has many similarities to counter-regional systems seen elsewhere in the GOM (Figure 20). Analog experiments performed by Ge et al. (1997) provide step by step representations of a complex salt structure being formed due to progradation that include rollover expulsion and detachment features and may be similar in nature to the salt structure found in the study area (Figure 20).

Recently, Hudec et al. (2009) published a paper on the factors that drive

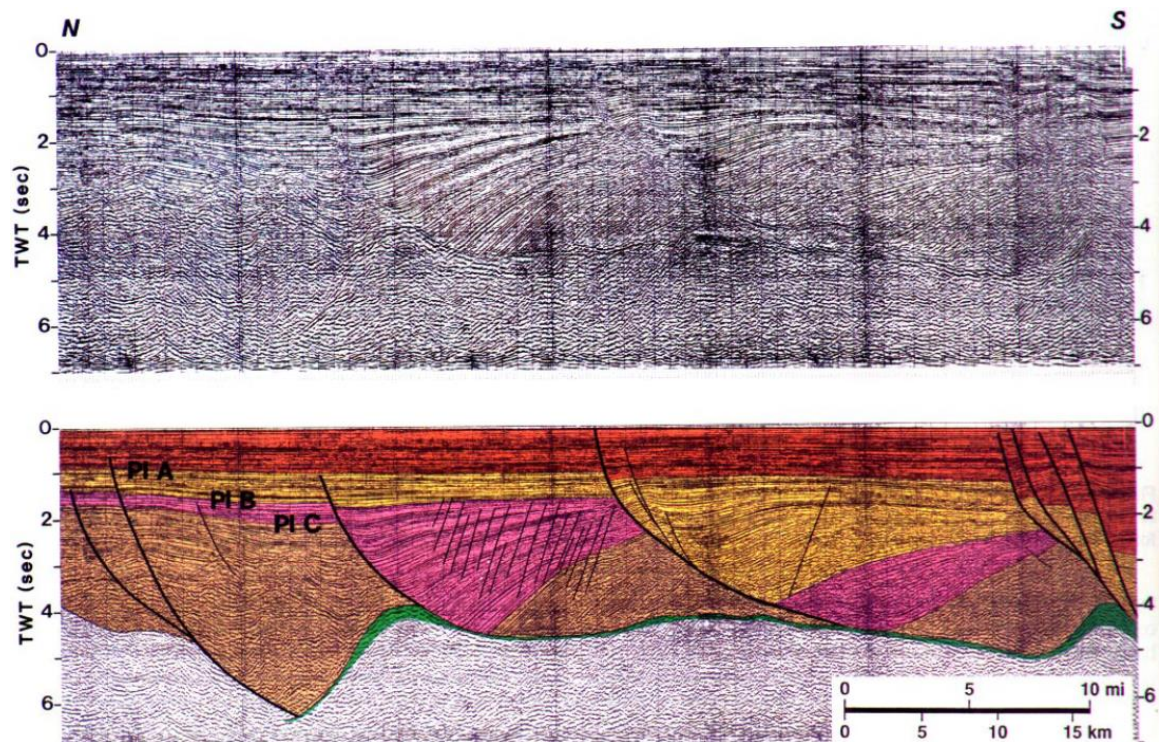


Figure 19: Uninterpreted (top) and interpreted (bottom) seismic profile across an organized roho system, western Louisiana outer shelf, showing roho reflections along the detachment for Pliocene-Pleistocene listric growth faults. A north-dipping counter-regional salt feeder is interpreted at the north end of the subhorizontal salt weld (green) Pl A, B, C = three successive Pliocene-Pleistocene levels. From Diegel et al (1995).

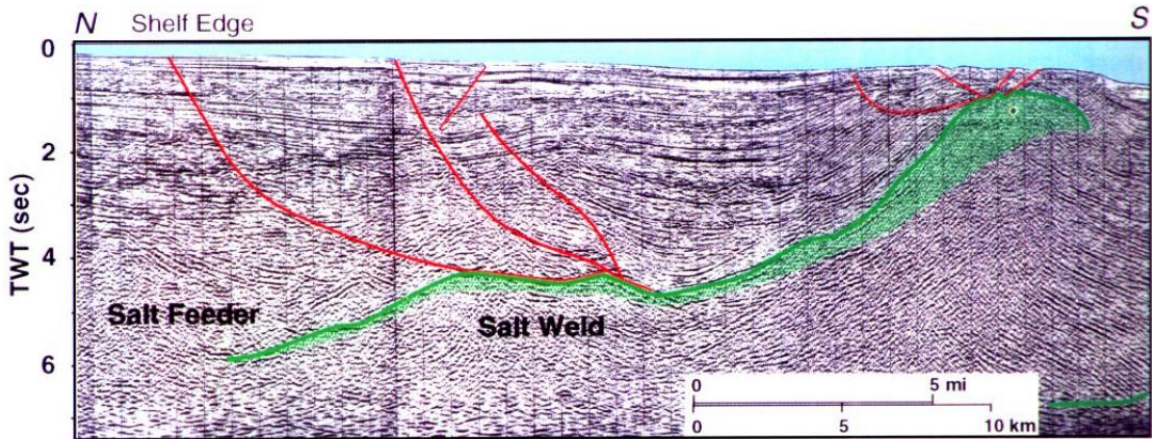


Figure 20: Counter-regional salt feeder and associated fault systems. From Diegel et al. (1995).

minibasin subsidence into a salt floor. While they concur that the common theory of density-driven subsidence is generally a valid explanation for these occurrences, they do not fully explain early history or changes in minibasin depocenters. Instead, they offer five alternatives:

1. *During diapir shortening, the squeezed diapirs inflate, leaving the intervening minibasins as bathymetric depressions.*
2. *In extensional diapir fall, stretching of a diapir causes it to sag, producing a minibasin above its subsiding crest.*
3. *During decay of salt topography, a dynamic salt bulge subsides as upward flow of salt slows, which lowers the salt surface below the regional sediment surface.*
4. *During sedimentary topographic loading, sediments accumulate as a bathymetric high above salt.*
5. *Subsalt deformation affecting the base of salt may produce relief at the top of salt.*

Evidence for each of these alternatives can be seen either above the main Whiting Dome salt structure or above the feeder and will be covered in the interpretation section.

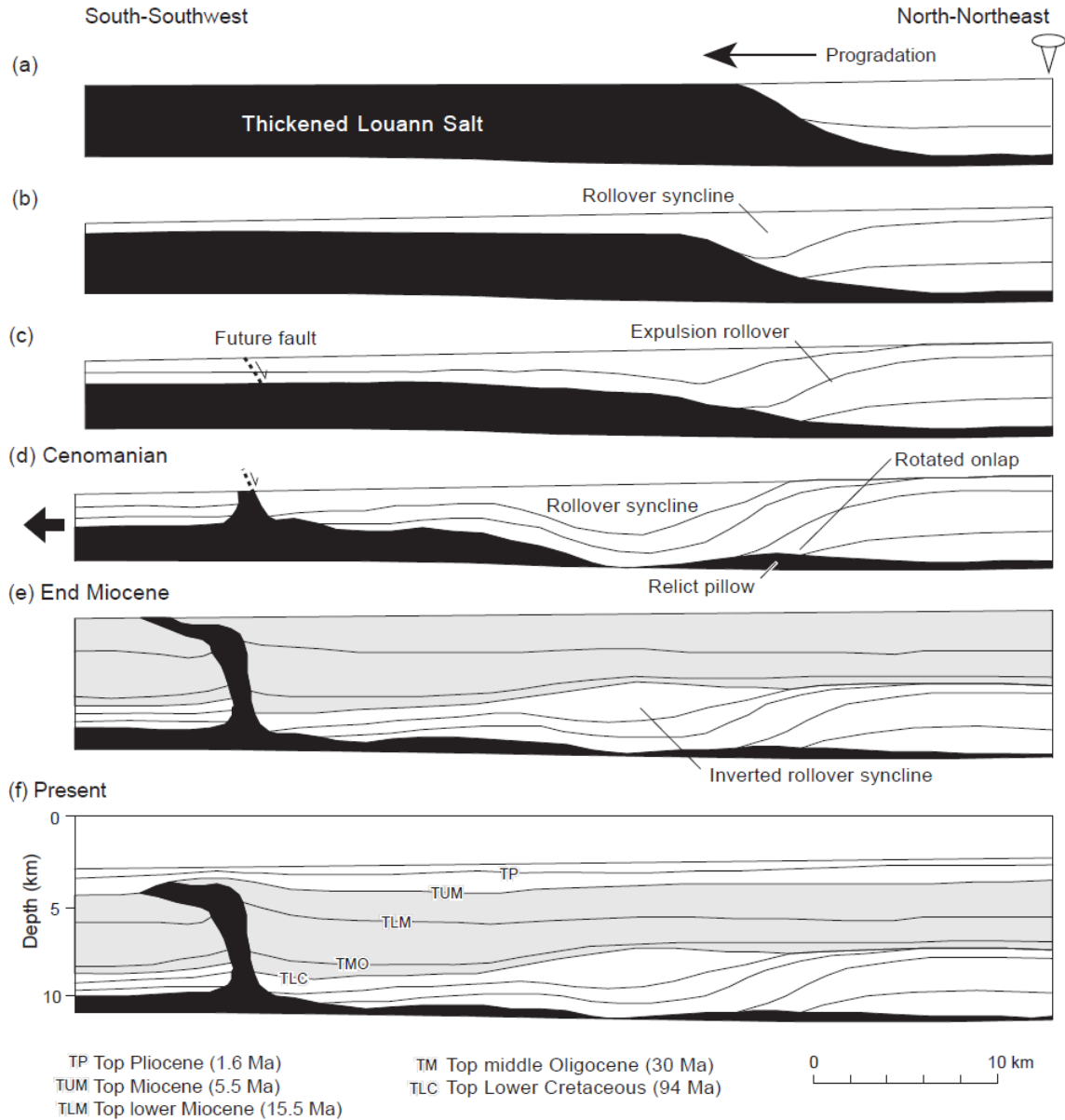


Figure 21: Reconstruction of a depth section from the northeastern Gulf of Mexico. Prograding wedges between the Upper Jurassic and the Lower Cretaceous were slightly reinterpreted based on the original seismic line. Wedges were restored to 1° initial dip; other horizons were restored to 0.5° initial dip. Section (c) was slightly shortened compared with section (d) to compensate for extensional faulting. Minor faults were omitted. From Ge et al. (1997).

1.5.3.1 Jurassic Rafts in the Northeastern Gulf of Mexico

Pilcher et al (2014) define raft tectonics as “the gravitational gliding of coherent fault-bounded blocks on a low-angle detachment (typically of thin salt), where the blocks become completely separated from each other through extreme extension.” The rafting that occurred in the northeastern GOM lasted from roughly the Upper Jurassic into the early parts of the Paleogene (Figure 6).

The syndeformational depocenters (in this case, the late Jurassic-early Cretaceous Cotton Valley Group) have a tendency to experience a change in depositional polarity, switching from landward thickening wedges associated with older regional basinward-dipping listric faults to basinward thickening wedges associated with younger counter-regional landward dipping listric faults (Pilcher et al., 2014). This phenomenon has been termed “flip-flop” salt tectonics by Quirk and Pilcher (2012). Along these counter regional faults, total extension of the system can be calculated using the fault gaps, or the distance between the pre- and syndepositional packages (Figure 22); however, interpretation of fault gaps where salt is present can make distinguishing the influence of extension versus early salt mobilization imprecise (Pilcher et al., 2014).

Of particular interest is the following interpretation by Pilcher et al. (2014) of the onset of extension:

The onset of the main episode of extension occurred immediately after Haynesville deposition and is interpreted to have been sudden and rapid because the high-angle faulted edges of the carbonate raft cores are

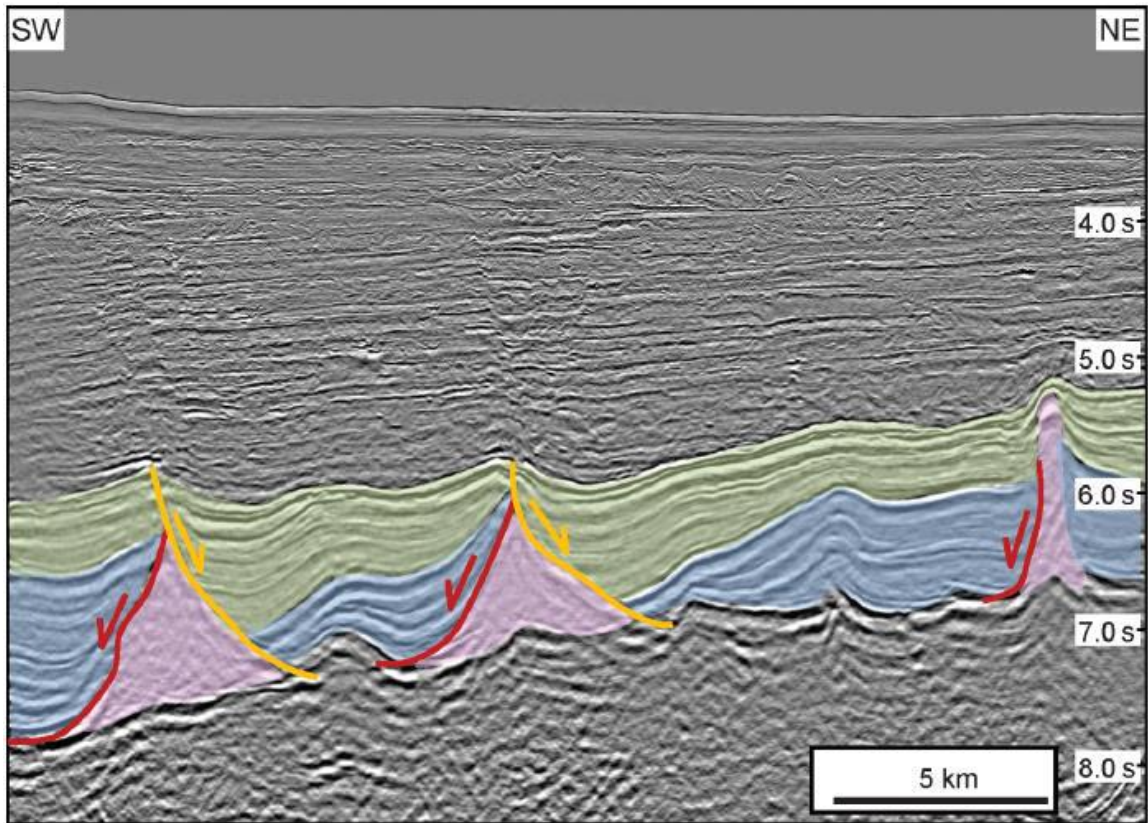


Figure 22: Seismic line showing flip-flop salt tectonics characterized by Jurassic landward-thickening wedges (blue) associated with early faults (red), followed by a polarity flip to Cretaceous basinward-thickening edges (green) associated with later faults (yellow). Salt is highlighted in pink. From Pilcher et al. (2014).

typically draped by the syndeformational strata of the Cotton Valley Group, rather than having an apparent downlap onto the fault weld as would be expected in a synkinematic sequence.

Unfortunately, such high-angle faults are not likely to be found in the study area due to a lack of high-tensile strength deposits during the requisite time period (Mayall et al., 1992; Galloway et al., 2000; Pilcher et al., 2014). This will probably limit as precise a dating of detachment in the study area. Late stage and end of rafting, however, should be as equally obvious as in the Mesozoic rafting events. Pilcher et al. (2014) note that post-

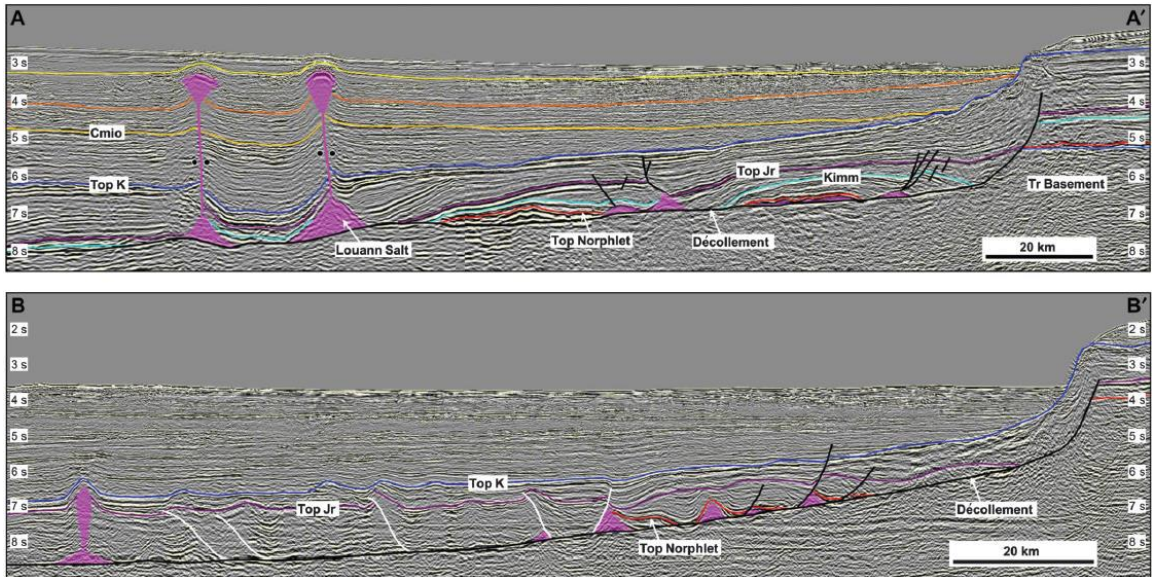


Figure 23: Visualization of structural differences between pre-, syn-, and post-raft tectonic depositional phases. Pre-raft phases are from base salt to Top Jr. Syn-raft phases are from Top Jr to Top K. Post-raft phases are from Top K to water. From Pilcher et al (2014).

Cretaceous depositional phases do not show any evidence for continued gravity gliding. Instead, younger structure tends to be predominantly based on differential compaction causing upward mobility of salt rather than horizontal spreading (Figure 23) (Pilcher et al., 2014).

CHAPTER 2: METHODOLOGY

2.1 Data Acquisition

The data for this study is divided into two major categories: geologic and geophysical. Geologic data is comprised of well information, paleontological reports, and mud log and core reports. Geophysical data is comprised of seismic data, wireline log data, and velocity surveys.

Non-seismic data was acquired through the Bureau of Safety and Environmental Enforcement's (BSEE) database (BSEE, 2017). In order to retrieve any data pertinent to this study, all information about wells lying within the study area was ordered from the BSEE database. This was done by querying the database for each block lying within the study area in both the Viosca Knoll (VK) and Mississippi Canyon (MC) Outer Continental Shelf (OCS) protraction areas. The wells with information pertinent to this study are shown in and listed in Table 1. Each block within these protraction areas is 9 square mile. These files were delivered on a DVD in .tif format and viewed using IrfanView in order to assure

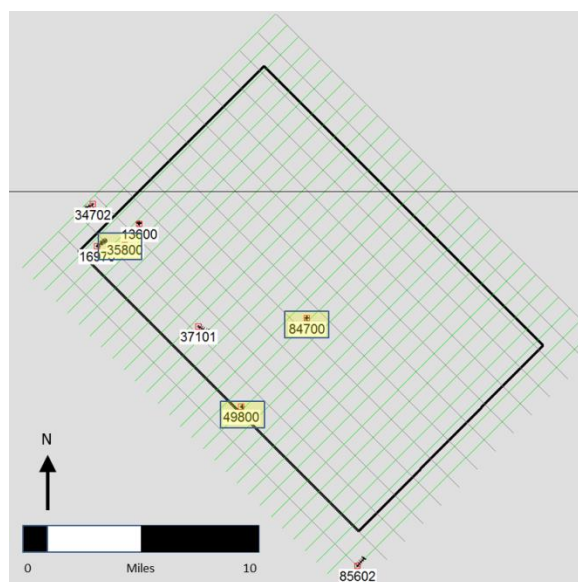


Figure 24: Well locations with final 5 digits of API number. Wells 35800, 49800, and 84700 were the wells primarily used to interpret seismic data.

the quality of each piece of data (Skiljan, 2017). Well log data was then imported into and viewed in .tif format (known as raster logs) using IHS Petra version 3.7.2. The raster logs were then digitized in order to be able to manipulate and interpret the logs easier with both Petra and the seismic interpretation software. This process is detailed more thoroughly in the section 2.1.1. Following this step, the digitized well logs were exported to the seismic interpretation software to be used as a control on the interpretation process.

Seismic data was generously provided by Tomlinson Geophysical Services, Inc. (TGS). Full specifications and deliverables can be seen in Appendix A. This data was uploaded to the seismic interpretation software, IHS Kingdom 15, and interpreted using the well log data as a control. More information regarding this process can be found in section 2.4.

API Number	Well Name	OCS	Block Number	Logged Depth (ft)	
6081740	13600	OCSG-4286 No. 1	MC	28	14640
	16970	OCS-G-4256 No. 2	MC	28	12223
	34702	OCS-G-9771 No. 1	MC	28	7700
	35800	OCS-G-9771 No. 2	MC	28	10750
	37101	OCS-G-7925 No. 1	MC	118	12239
	49800	OCS-G-7926 No. 1	MC	162	15770
	84700	OCS-G-14629 No. 1	MC	119	10475
	85602	OCS-G-18207 No.1	MC	252	11763

Table 1: Well information for wells used in this study.

2.1.1 Digitization of Raster Logs

For many decades, the industry standard visualization for well logs was in a printed, paper format. A single well log tool run could produce a stack of folded paper several inches thick. These paper logs would then be correlated through a series of steps that will not be detailed here. Technology has advanced to the point that old well logs have been scanned and can be viewed in a digital format as a raster log (Figure 25). However, this format is not easy to correlate and manipulate when performing seismic interpretation or normal log calculations. In order to increase efficiency and maximize database operations, fully digital logs began being adopted in the late 1970s and are currently the dominant type of well log. In order to convert a raster log to a fully digital well log, each individual well log curve must be ‘traced.’ In this case, tracing refers to the act of copying the original raster log curves into a digital format through a masking technique.

In Petra, this is accomplished in a multiple step process and can only be performed on one log curve at a time:

1. *Set log curve name*
2. *Set left and right track boundaries*
3. *Set depth markers*
4. *Straighten log edges*
5. *Begin digitizing log*
6. *End digitizing log*

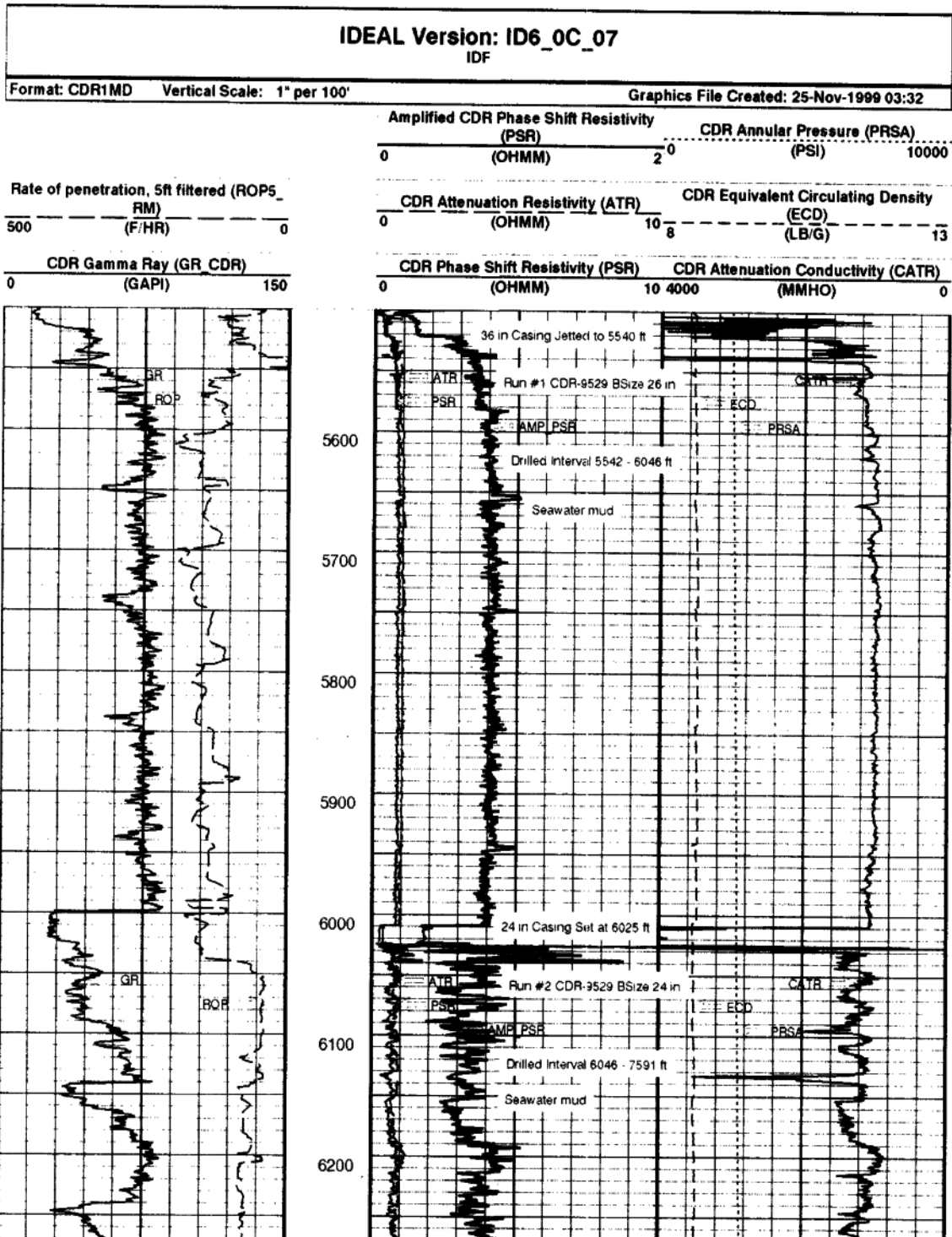


Figure 25: Example of a raster log that has not been digitized. Note the slightly off-axis tilt of the log columns.

7. *Save file*

8. *Load Curve*

There is also an auto-pick method in Petra, but it is finicky and often ineffective. It follows the same general guidelines as manually

API Number		Digitized Logs			
		GR	NPHI	DPHI	DT
6081740	13600	x	x	x	x
	16970	x			
	34702	x			
	35800	x		x	x
	37101	x			
	49800	x			
	84700	x			
	85602	x			

Table 2: List of wells and the specific logs that were digitized for this study.

digitizing a log curve and has the potential to save large amounts of time, but it often tracks off onto the grid lines behind the curve and so becomes inefficient for log curves without bold typeface.

Once the log has been digitized, it can be manipulated using many different types of features in both Petra and Kingdom, such as facies shading, log correlations, petrophysical cross-plot diagrams, and can be used to form synthetic seismograms to ensure proper well ties to seismic data.

2.2 Geologic Interpretation

While this study is primarily based on seismic interpretation of stratigraphic and structural features, the semi-ambiguous nature of seismic data is highly dependent on ground truthing (in this case, well log data) to obtain a reasonable amount of legitimacy.

Ground truthing is a general term for confirming what type of strata lay in the subsurface. This is especially important in the interpretation of seismic data as, is often the case, amplitude data can be easily misinterpreted due to amplitude data appearing

very similar in two different locations while being very dissimilar in truth. Ground truthing also helps denote faulted and non-conformable sequences in the subsurface and, conversely, sequences that may appear faulted that are actually variations in geomorphology or lithology.

The BSEE database contained 12 wells within the study area that contained relevant data. The different types of data are described in further detail in the following sections.

2.2.1 Paleontology Surveys

As mentioned earlier, the Gulf of Mexico basin relies heavily on paleontological data to define the chronozones and, thus, the seismic stratigraphy of the basin. The chronozone reference used in this study was the MMS Biostratigraphic Chart (Figure 14). In order to consolidate the information from the individual well reports, a table was created to show the depth range and corresponding system, subsystem, series, and age of each biostratigraphic marker (Table 3).

Time (mya) (not to scale)	CHRONOSTRATIGRAPHY				BIOSTRATIGRAPHY		BOEM CHRONOZONE				
	System	Subsystem	Series	Stage	Foraminiferal planktic & benthic regional and local markers	Calcareous nannoplanktic regional and local markers					
	Q u a t e r n a r y		P l e i s t o c e n e	Holocene	<i>Globorotalia inflata</i>						
				Upper	I o n i a n	<i>Globorotalia flexuosa</i>	Emiliana huxleyi (base of acme) Pontosphaera indoceanica Gephyrocapsa oceanica flood Gephyrocapsa caribbeanica flood	PLU			
0.20						<i>Globorotalia truncatulinoides</i> coiling change, right-to-left	Helicosphaera inversa Pseudoemiliana lacunosa "A" Pseudoemiliana lacunosa "B" Gephyrocapsa caribbeanica increase Gephyrocapsa omega Gephyrocapsa parallela Pseudoemiliana ovata	PLM			
0.78				Lower	C a l i a b r i a n	Trimosina "A"					
						Stilostomella antillea <i>Globorotalia incisa</i> Sphaeroidinella dehiscons acme "A" Trimosina "A" acme Angulogerina magna Hyalinea balthica / Trimosina "B" <i>Globorotalia tosaensis tosaensis</i> Sphaeroidinella dehiscons acme "B" Angulogerina "B" Uvigerina hispida	Pseudoemiliana lacunosa "C" acme Gephyrocapsa aperta acme Scyphosphaera pulcherima, Gephyrocapsa caribbeanica (large) Helicosphaera sellii Lithostromation perdurum Calcidiscus macintyreii	PLL			
1.77						P l i o c e n e	Upper	G e l i a s i a n	<i>Globorotalia crassula</i> acme, <i>Globorotalia praeirrisa</i> Cristellaria "S" <i>Globorotalia menardii</i> coiling change, left-to-right <i>Globorotalia exilis</i> <i>Globorotalia miocenica</i> <i>Globorotalia pertenuis</i> Bolivina imbricata / "P" Lenticulina 1 Textularia crassisepta / "P"	Discoaster brouweri, Calcidiscus macintyreii increase Discoaster brouweri "A" Discoaster pentaradiatus Discoaster surculus	PU
2.60									p i a c e n	Ceratobulimina pacifica Cassidulina laevigata carinata acme / "L" Haplophragmoides emaciatum Saracenaria "H" <i>Globorotalia multicamerata</i> <i>Globoquadrina altispira</i> = Valvulineria "H" Cyclammina sp. Arenaceus fauna Cibicides grosseperforatus Sphaeroidinellopsis seminulina Textularia 1	
3.58							Lower	Z a n c i l i a n		Buccella (Eponides) hannai acme Cibicides marsi <i>Globorotalia margaritae</i> Uvigerina rustica Globigerina druryi / nepenthes "B" Globigerina nepenthes Bulminella 1 Siphonotextularia jugosa / "J" Sigmoliina "P" / cf. schlumbergeri Sphaeroidinellopsis multikobata Globigerinoides mitra <i>Globorotalia plesiotumida</i> acme	Sphenolithus abies Reticulofenestra pseudoumbilica, Discoaster intercalcaris, Dictyococoides antarcticus Pseudosphenolithus abies "B" acme Sphenolithus abies "B" Amaurolithus tricorniculatus Ceratolithus acutus Discoaster quintatus
5.32									M e s s i n i a n	<i>Globorotalia menardii</i> coiling change, right-to-left <i>Globorotalia margaritae</i> primitiva <i>Globorotalia juanai</i> Textularia "X" Textularia latumi Bolivina denticulata	Discoaster quinquemurmus Discoaster berggrenii Reticulofenestra rotaria Discoaster berggrenii "A"
7.12							U p p e r	T o		Textularia 6 Bigenerina irregularis / 6 <i>Globorotalia acostaensis</i> coiling change, right-to-left Planulina renzi Reophax davepopel, Robulus "E" Bigenerina floridana / "A" Cristellaria "K" Melonis pompilioides increase Cibicides trinceransensis Uvigerina carapitana Amphistegina "E" Cyclammina 3	Discoaster neohamatus Discoaster loeblichii Minylithus convallis Catinaster mexicanus Discoaster bellus, Discoaster calcaris

Figure 26: MMS Biostratigraphic chart (only s portion of the chronozones relevant to this study are shown)

MMS Biostratigraphy		API # - Depths (FT) (6081740...)													
Chronozone	MYA	Fossils	13600	16970	34702	35800	36800	37101	37500	49800	60300	84700	85602		
PLL	0.78	Hyalinea balthica				3580									
	1.77	Discoaster brouweri									4260				
PU	2.60	Disco asymmetricus				3730									
		Globorotalia multicaemata						4620							
		Valvulineria "H"	3530			3730									
PL	3.58	Globoquadrina altispira			3800			4740					7590		
		Sphaeroi dinellopsis seminulina								5820					
		Sphenolithus abies				4360					7530				
		Reticulofenestra pseudoumbilica				4960									
		Globigerina druryi	5570	5370	4280	4900	4400			6900		6680			
		Bulimina 1	5570	5370						6900		6800	7740		
		Globigerina nepenthes			4280	5140	4940		6780					7740	
		Amurolithus tricorniculatus													
		Siphotextularia jugosa			4700	5980							7610		
		Ceratolithus acutus												9890	
MUU	5.32	Globigerinoides mitra			7130	6340	6350	8340							
		Globorotalia menardii							8980						
		Disco quinqueramus				6760	6170								
		Disco berggrenii				6820	6410					10010			
		Textularia T													
		Disco neohamatus													
		Disco loeblichii													
		Uvigerina rustica													
		Robulus "E"													
		Bigenerina "A"													
MLU	7.12	Cristallaria "K"	10550							9870					
		Discorbis 12													
		Bigenerina "B"	12590							10330					
		Globoquadrina dehiscens													
		Textularia L	13400												
MUM		Globorotalia mayeria													
		Fohsi robusta													
		Fohsi fohsi													

Table 3: Biostratigraphic markers and associated chronozones for wells in the study area according to the MMS Biostratigraphic Chart.

2.2.2 Well Log Curves

There are a multitude of well logs available in any given wireline log suite. For the purposes of this study, the most important, and most used, log curves are the gamma ray (GR), density, velocity and sonic.

Gamma ray logs are one of the best tools for interpreting the subsurface as they give a good sense of sand versus shale lithologies and often match fairly well with seismic amplitudes (Figure 27).

Velocity and density logs are necessary for the creation of synthetic seismograms. Should a velocity log or time-depth chart not be available for a well, it may be substituted with a sonic log. This process is carried out in Kingdom in order to tie the individual wells to the seismic data; the details of the process will be covered in more detail in the seismic interpretation section.

2.2.3 Log Correlation

Because of the complex structural systems around the salt body, correlating logs across the study area would not be extremely beneficial for seismic interpretation or structural and stratigraphic information. However, the logs can be successfully combined with information from the paleontological reports to distinguish general time packages of strata. Using the aforementioned paleontological data, chronozones can be fairly confidently picked and matched across the study area. A simple correlation can be seen in Figure 28.

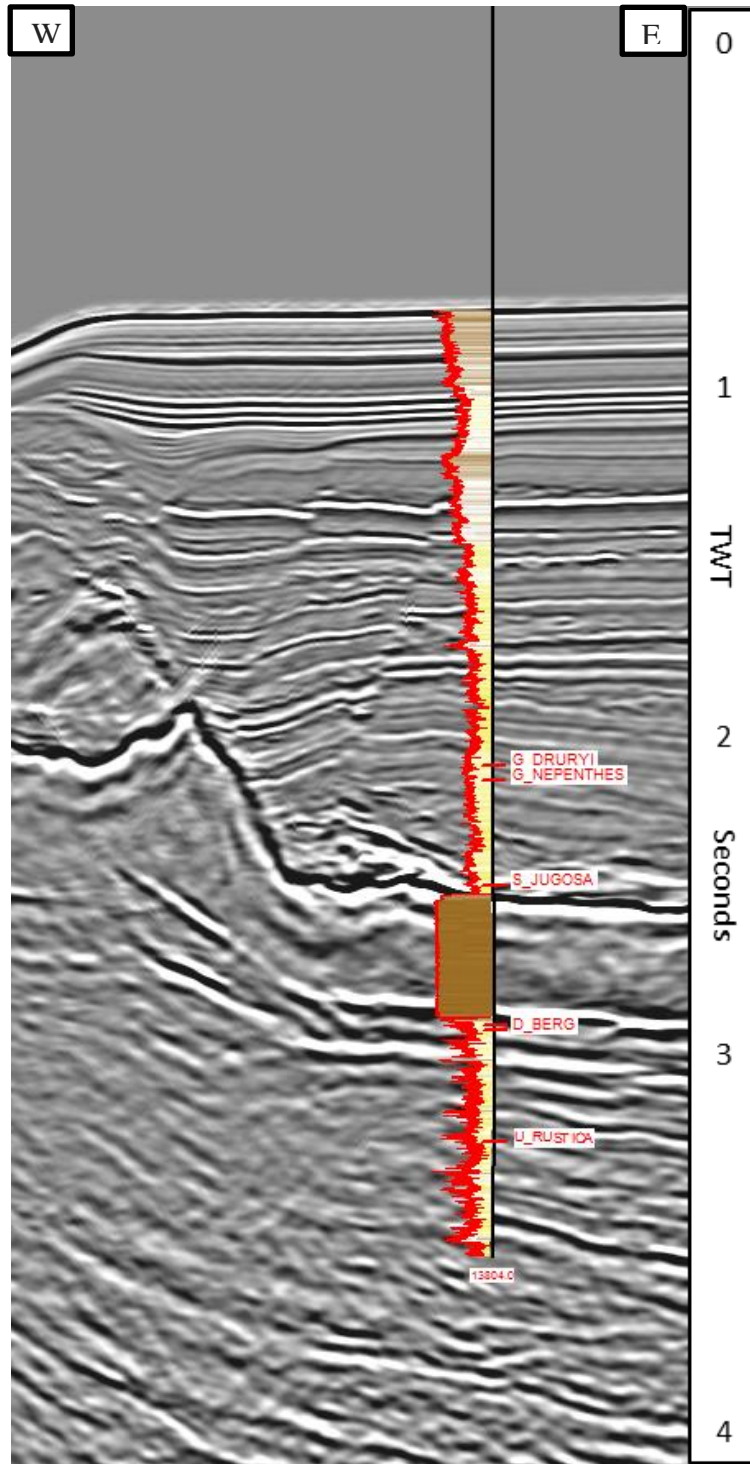


Figure 27: Gamma ray log overlain on time domain seismic data. Depth domain log data was tied to seismic data using a time-depth conversion chart generated using data found in the well log.

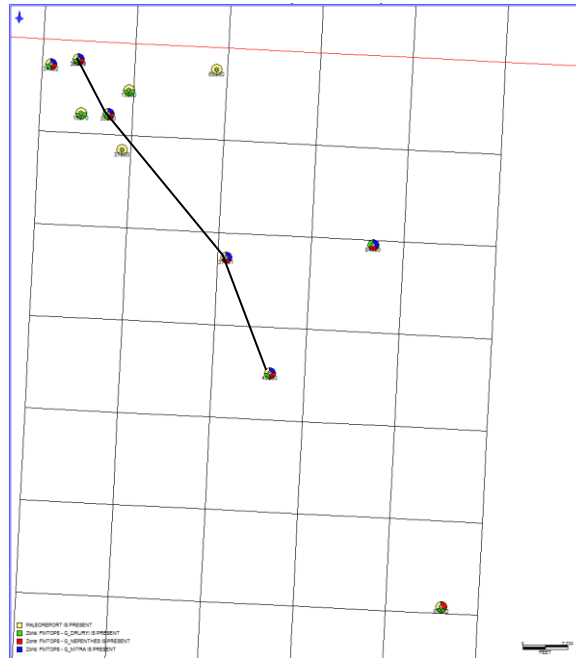
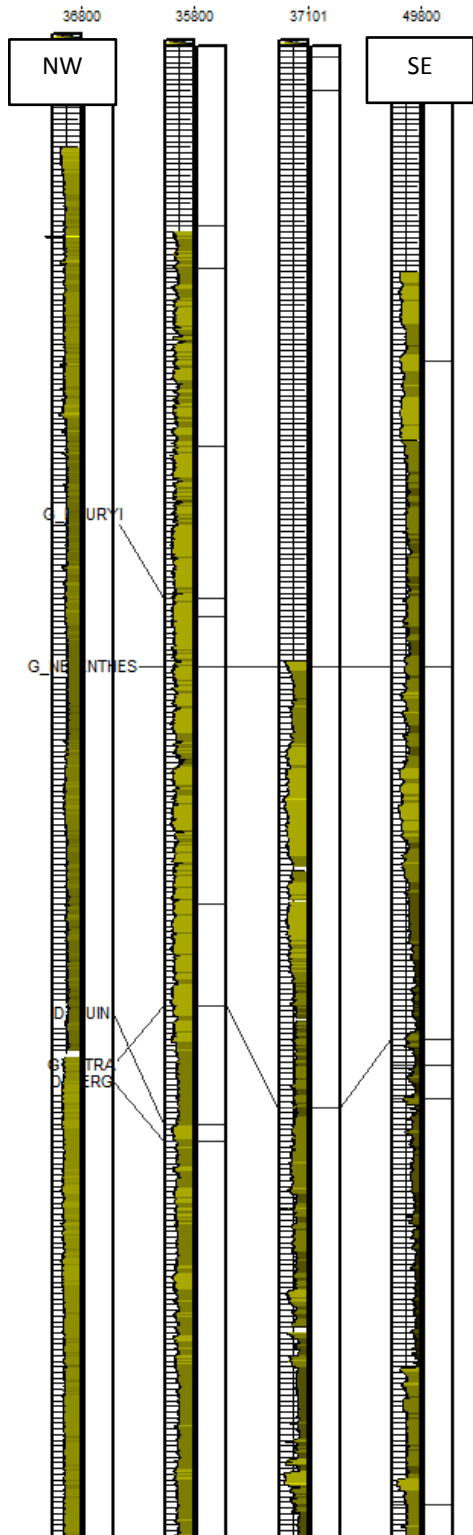


Figure 28: Simple log correlation across various well logs using gamma ray logs and paleodata. Well datums hung on *Globigerina nepenthes* foraminifera bed marker. Yellow represents sand; brown represents shale. Last five digits of well API number from NW to SE: 36800, 35800, 37101, 49800. Log correlation performed in Petra.

2.3 Seismic Interpretation

This study revolves around the interpretation of the 3D seismic data provided by TGS. Thus, the steps needed to ensure as accurate a representation as possible are of the utmost importance. Several of these steps have been covered in previous sections. Once the well log data has been analyzed and converted to a digital medium, a synthetic seismogram must be created in order to tie the well logs to the seismic data.

2.3.1 Creation of a Synthetic Seismogram

The creation of a synthetic seismogram requires three ingredients: a time-depth chart, velocity log, and density log. From IHS Kingdom's Help function:

“To generate a synthetic, you must provide a T-D Chart, a velocity curve, and a wavelet. If a velocity or density log is not available, log conversions are available to derive the curves from sonic, resistivity, or density logs. In addition, density may be set to a constant value, such as 1. Once the parameters are selected, SynPAK automatically calculates the Acoustic Impedance (AI) and the Reflection Coefficient (RC) for each sample interval.”

SynPAK is Kingdom's synthetic seismogram management attachment. The time-depth chart is self-defined; it correlates specific depths in a borehole with a specific two-way time. This allows the well logs, which are always in a depth domain, to be overlain on seismic data, which is in a time domain for this study. The synthetic seismogram used for this study can be seen in Figure 29.

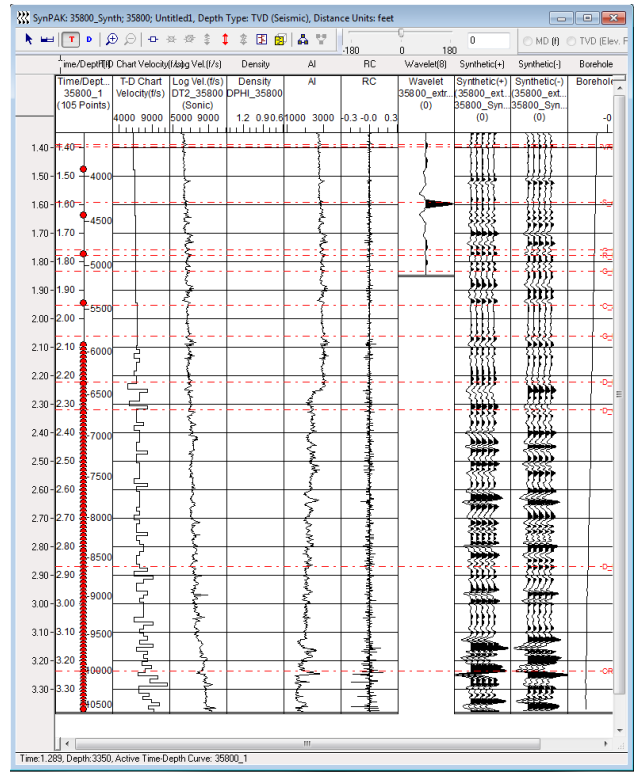
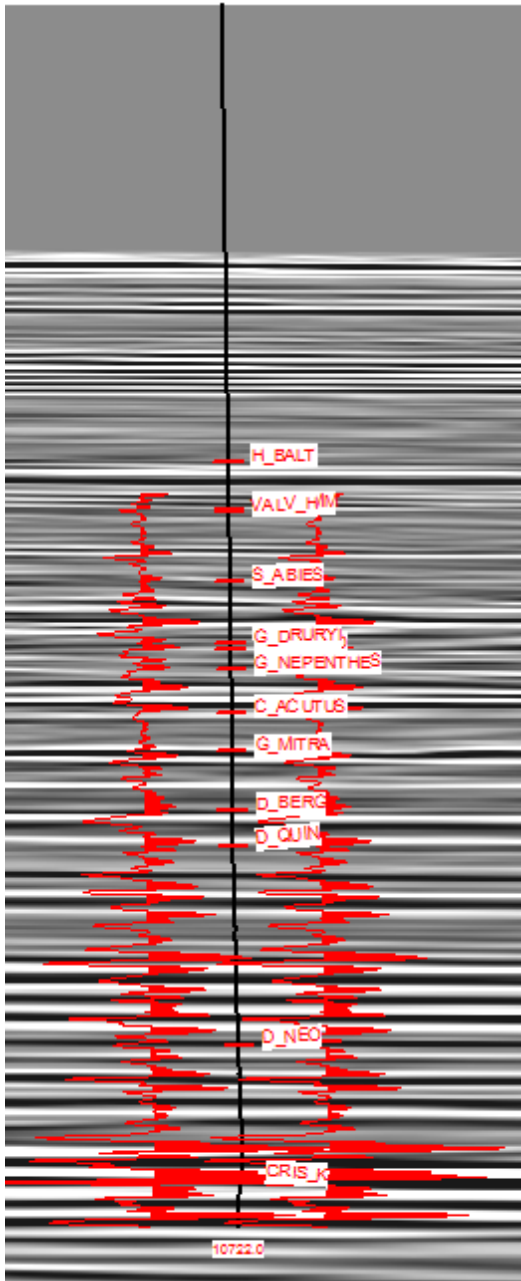
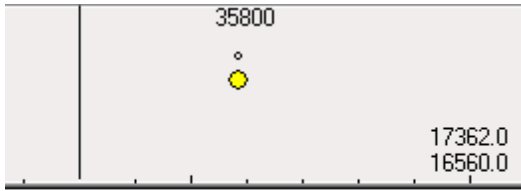


Figure 29: Right: Synthetic seismogram generator in Kingdom 15. Left: Synthetic seismogram (red) with paleomarkers overlain on time domain seismic data. Seismograms are used to validate well to seismic ties.

2.3.2 Seismic Stratigraphy

The tops picked in this study were based on the MMS Biostratigraphic Chart's chronozones and the general location of biomarkers and their relationship to the gamma ray logs in each well.

Picking stratigraphic tops in seismic data can often be extremely complicated, especially in regions as structurally complex as those around areas of salt mobilization. There are often times when amplitude horizons appear to be continuous or semi-continuous across an area when, in fact, they are not. This can be due to a variety of reasons. One of the highest occurrences is when erosion or faulting occurred and the strata in the fill or downthrown block has similar acoustic impedance statistics to the strata of older strata or upthrown block. This can only be rectified by working through the data in both directions to prevent mispicks from occurring.

2.3.3 Picking Horizons

A horizon is a generic term for a picked surface within the seismic data. This surface can range from anything as small as an amplitude anomaly within a stratigraphic unit to as large as a regional formation top. That being said, a 3D seismic block can be an immense amount of data to sift through. That is why it is best to begin picking horizons across the block in largely spaced increments (50-100 lines or crosslines) in order to get a feel for the general structure of the area. As the geometry of the study area becomes clearer, horizon picks should be made in smaller and smaller increments (1-25 line or crosslines) in order to refine the interpretation.

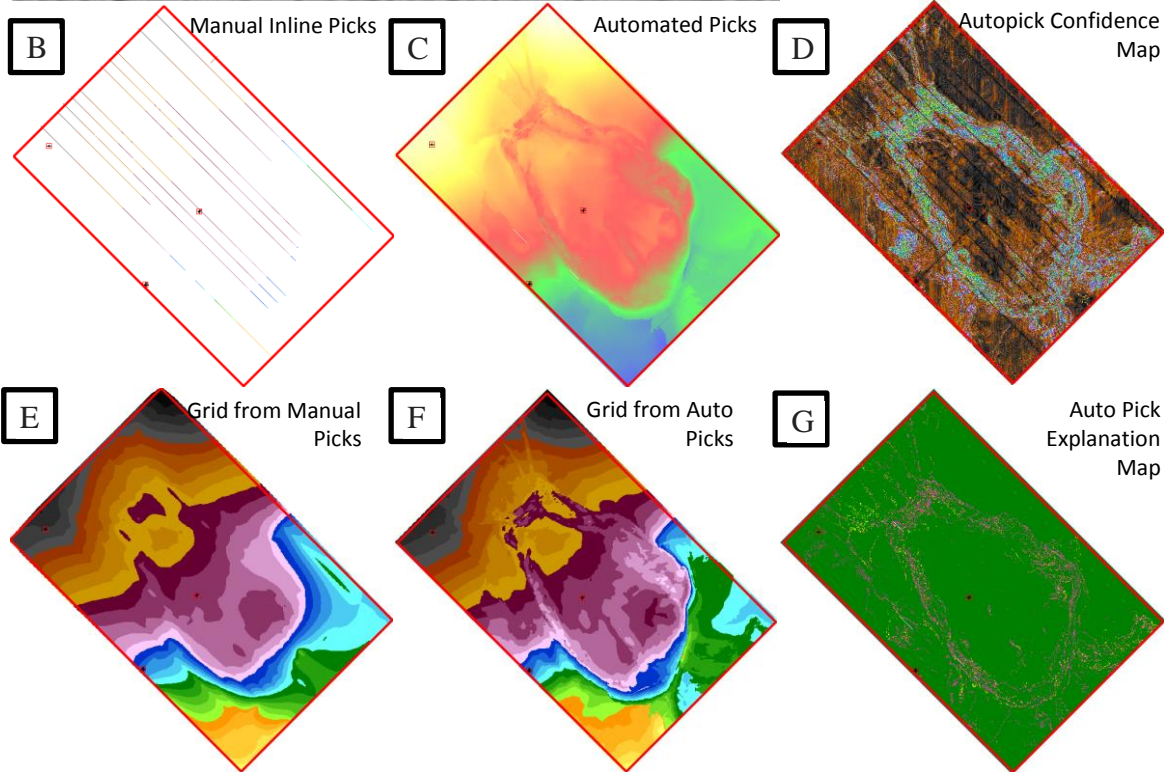
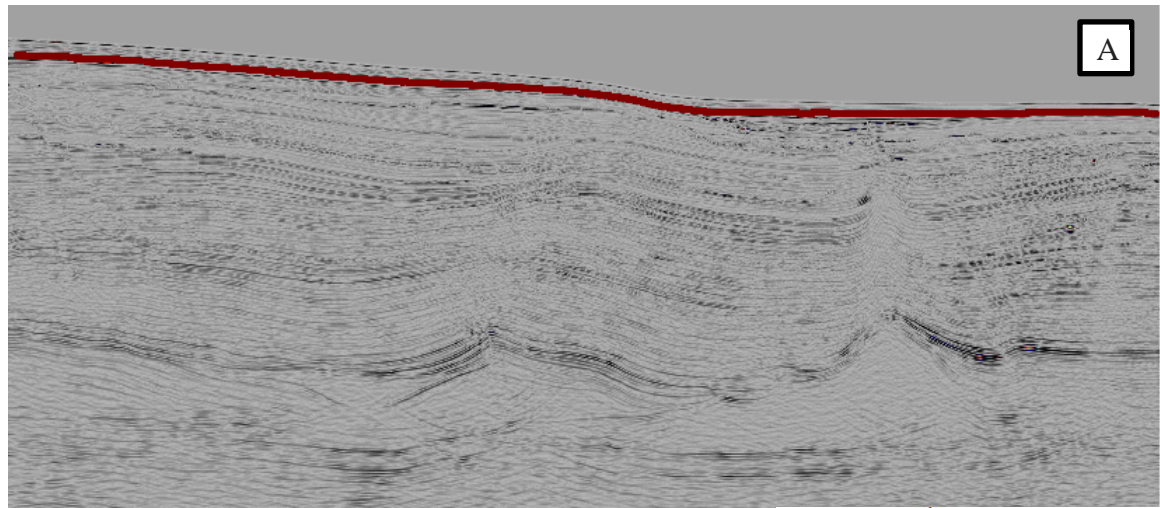


Figure 30: Example of a horizon and associated grids. (A) Horizon manually picked along high amplitude reflector (PLU). (B) Series of two dimensional lines picked across seismic survey. (C) Horizon auto-picked across entire seismic survey using initial manual picks. This method is only viable with fairly continuous reflectors, but it significantly increases the level of detail. (D) Confidence map for the autopicked horizon. Dark colors represent high confidence; light colors represent low confidence. (E) Grid generated using manual picks. (F) Grid generated using autopick horizon (G) Map showing autopick subset types.



Figure 30 gives examples for widely spaced manual horizon picks in a two dimensional domain, autopicking in a three dimensional domain, the resulting grids from each type of horizon picks, and some of the available data accrued during the autopicking process. The horizon used in Figure 30 is relatively continuous throughout the survey. This allows for high confidence automated pick results and fewer anomalies in the completed horizon.
















2.3.4 Evaluation and Imaging of Seismic Surfaces

Once an interpreter has reached a level of comfort with their picked horizons, grids may be made in order to represent the horizon in a 3D surface. This surface should easily display where any faulting or erosion has occurred and greatly assists in discerning whether the current picks for the horizon make geological sense. These grids can also be used to create isochron and isochore maps as well as other statistical models and data that add to the confidence level that the data represents a solid, geologically sound interpretation. Isochron maps are thickness maps based on the distance in two-way time between two horizons. Isochore maps are thickness maps using depth units (feet/meters). For the purpose of this study, isochore maps were generated using a constant velocity conversion from the associated isochron maps. The constant velocity for each horizon was derived using average velocities from well log data.

2.4 Restoration

Several conceptual reconstructions will be offered based on the interpretation of the horizons and their associated structural deformations throughout the seismic data.

CHAPTER 3: INTERPRETATION AND CONCLUSIONS

Tops	Stage	MYA*
 HOL	Holocene	0.0
 PLU	U. Ionian	0.12
 PLM	L. Ionian	0.20
 PLL	Calabrian	0.78
 PUU	Gelasian	1.77
 PUL	Piacenzian	2.60
 PL	Zanclian	3.58
 MUU1	Messinian	5.32
 MUU2	U. Tortonian	7.12
 MLU	L. Tortonian	9.00(?)
 MUM ¹	U. Serravallian	11.20
 TopK ²	Maastrichtian	65.00
 Louann ³	Callovian	159.40
	Salt Structures	
	Salt Weld	

* According to MMS Biostratigraphic Chart

1. Undifferentiated MUM to Top Cretaceous
2. Undifferentiated Cretaceous/Jurassic
3. Timing of Louann Salt deposition only; Evacuation into basal and allochthonous structures occurred during later periods

3.1 Interpretation and Results

This section identifies the areal extent of each chronozone shown in Figure 31. All dates provided in that figure are pulled directly from the MMS Biostratigraphic Chart except for that of the Lower Tortonian (MLU). No end date is specified for that stage in the chart. Specific time periods of salt mobilization are not identified; instead, general time periods are identified where halokinesis has a significant effect on the deposition or deformation of a stage's strata. Where applicable, subsalt strata is not mapped across the study area. It is, however, interpreted on 2D seismic lines. Figure 32 provides the locations

Figure 31: Legend for seismic block and line interpretation in Chapter 3.

of all the cross sections provided in this chapter. Smaller versions of this map will be provided as locator maps adjacent to the cross sections.

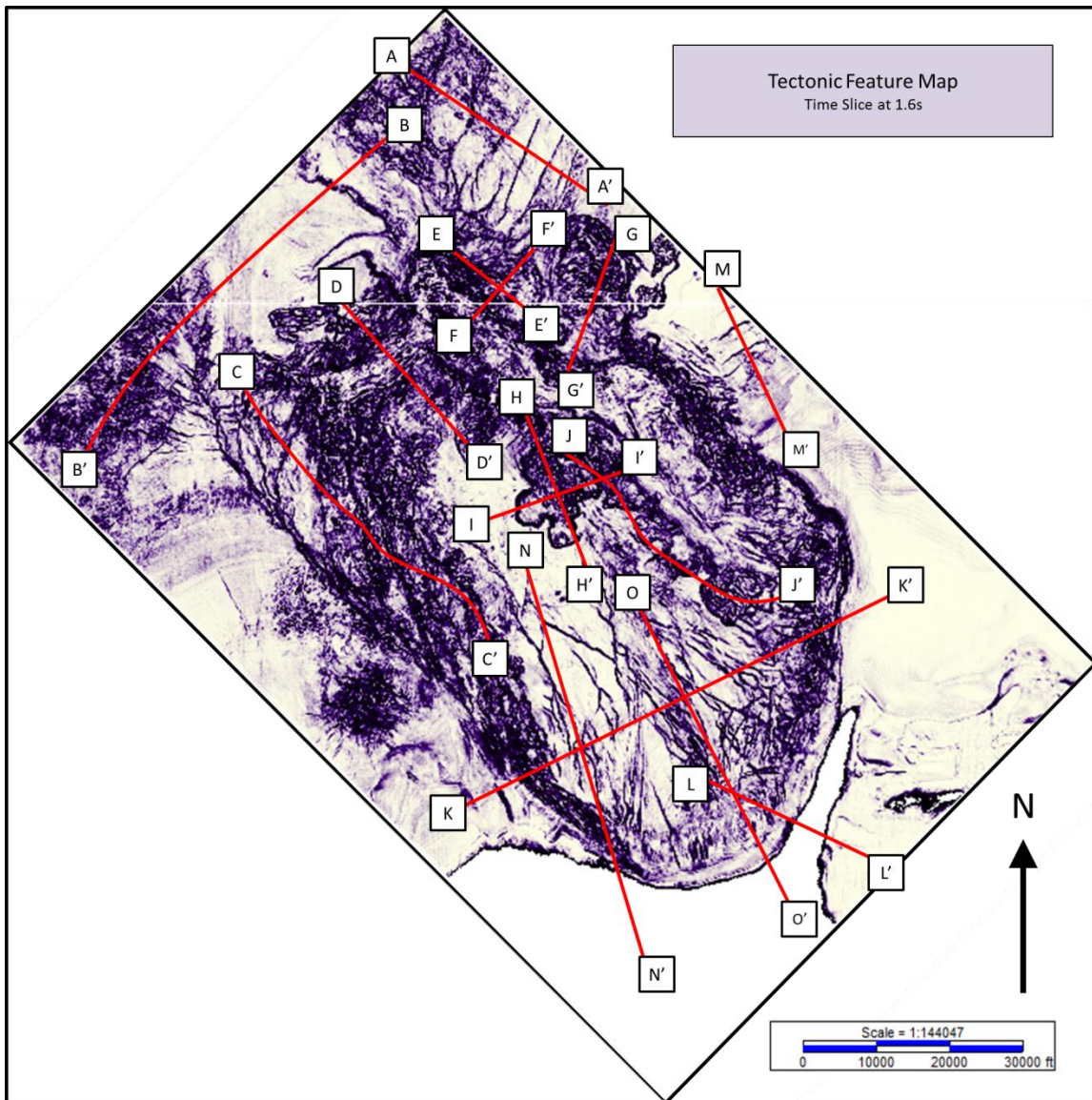


Figure 32: Location of interpreted arbitrary seismic lines shown in Chapter 3.

Allochthonous Salt

Lateral mobilization of autochthonous salt controlled development of regional and counter regional fault systems in the study area. However, the most complex structures are due to the upwelling and development of allochthonous salt and related fault systems. Figure 33 and Figure 34 provide a block model view of uninterpreted and interpreted seismic data along the north-south axis. These areas are outboard of the Whiting Dome and therefore are less structurally complex than those directly adjacent to, above, or under the salt structure. With only a few exceptions, post-Cretaceous strata outboard of allochthonous salt are parallel to sub-parallel with minor growth and offset along regional, seaward dipping faults. Most of the exceptions to this statement occur above evacuation basins above expulsing and welding autochthonous salt. These areas are especially prominent above basement lows.

The Whiting Dome salt structure's early evolution included extrusive salt glacier flow onto the sea floor above one of these developing evacuation basins (Figure 35). Differential loading of sediments onto the different salt bodies in the area and periods of fluctuating inflation, deflation, and lessening internal pressure of the salt bodies created an environment that led to an extremely asymmetrical salt structure in the Whiting Dome (Figure 36). Along with the other major named salt structure (Mitchell Dome) there are two other allochthonous bodies in the study area: a shelf-loaded diapir in the westernmost portion of the study area (Figure 37) and a very small detached diapir in the eastern

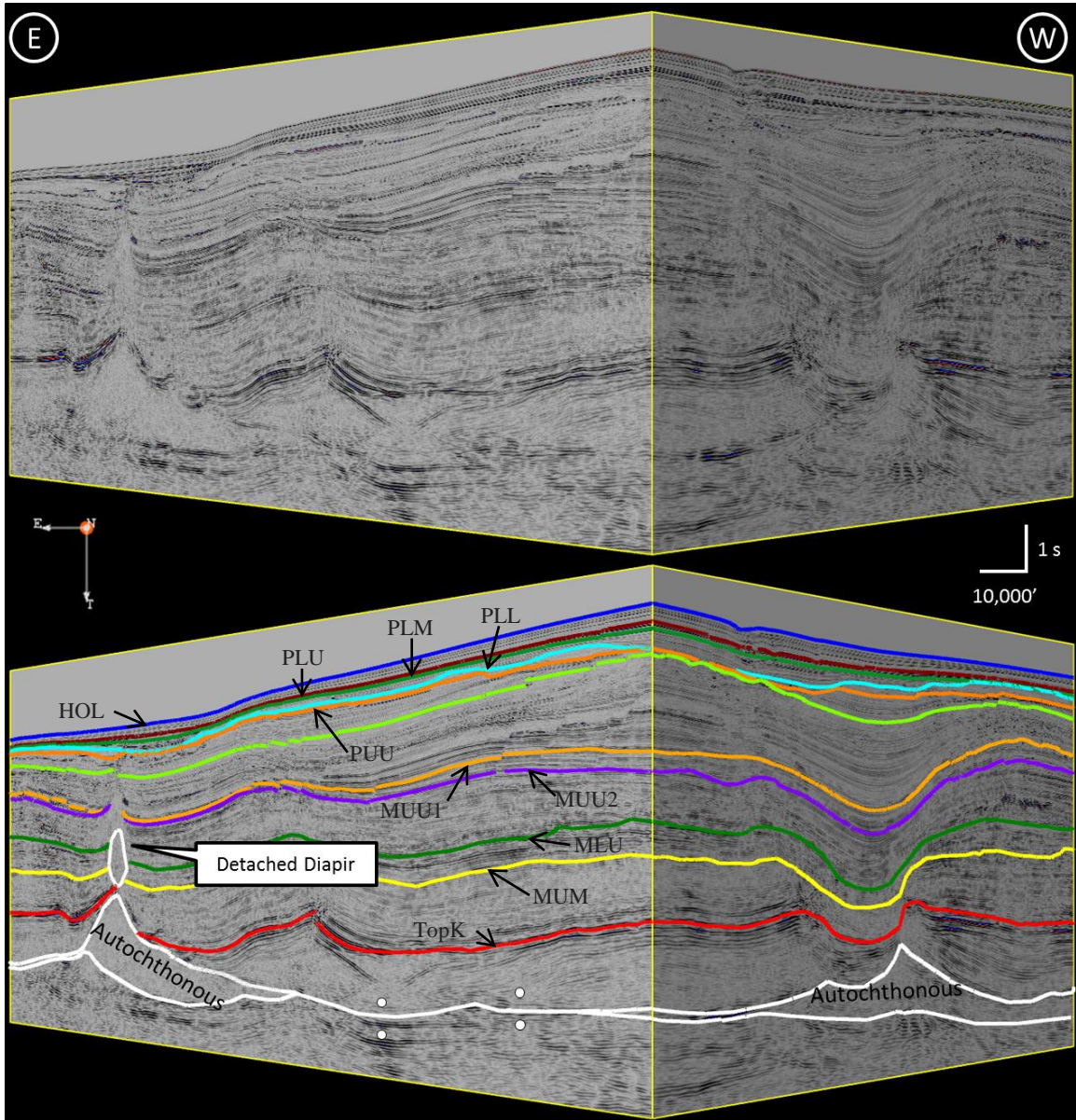


Figure 33: Uninterpreted (top) and interpreted (bottom), north oriented 3D reflection seismic block. White lines represent salt boundaries. In descending order, the other horizons (tops) represent: water bottom/HOL (blue), PLU (dark red), PLM (green), PLL (cerulean), PUU (dark orange), PL (neon green), MUU1 (light orange), MUU2 (purple), MLU (forest green), MUM (yellow), and TopK (red). Everything below the autochthonous salt is considered basement rock for the purposes of this study. Note the extensive welding and localization of salt ridge structures. Also, note the changes in depositional geometry below the TopK unconformity.

portion of the study area. All four of these structures are located above the autochthonous ridge structures.

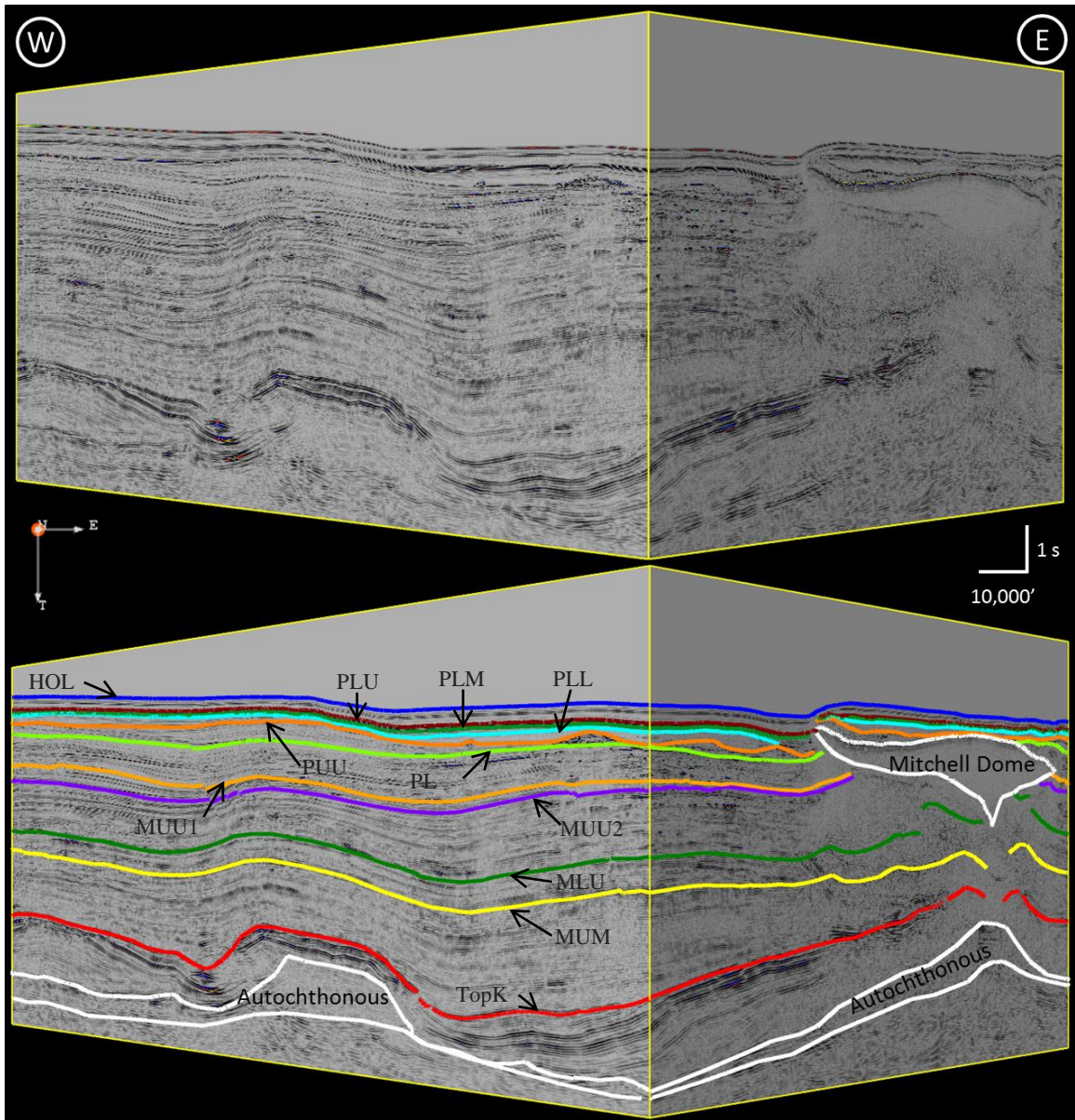


Figure 34: Uninterpreted (top) and interpreted (bottom), south oriented 3D reflection seismic block. White lines represent salt boundaries. In descending order, the other horizons (tops) represent: water bottom/HOL (blue), PLU (dark red), PLM (green), PLL (cerulean), PUU (dark orange), PL (neon green), MUU1 (light orange), MUU2 (purple), MLU (forest green), MUM (yellow), and TopK (red). Everything below the autochthonous salt is considered basement rock for the purposes of this study. Large detached diapir in the southern portion of the study area (Mitchell Dome).

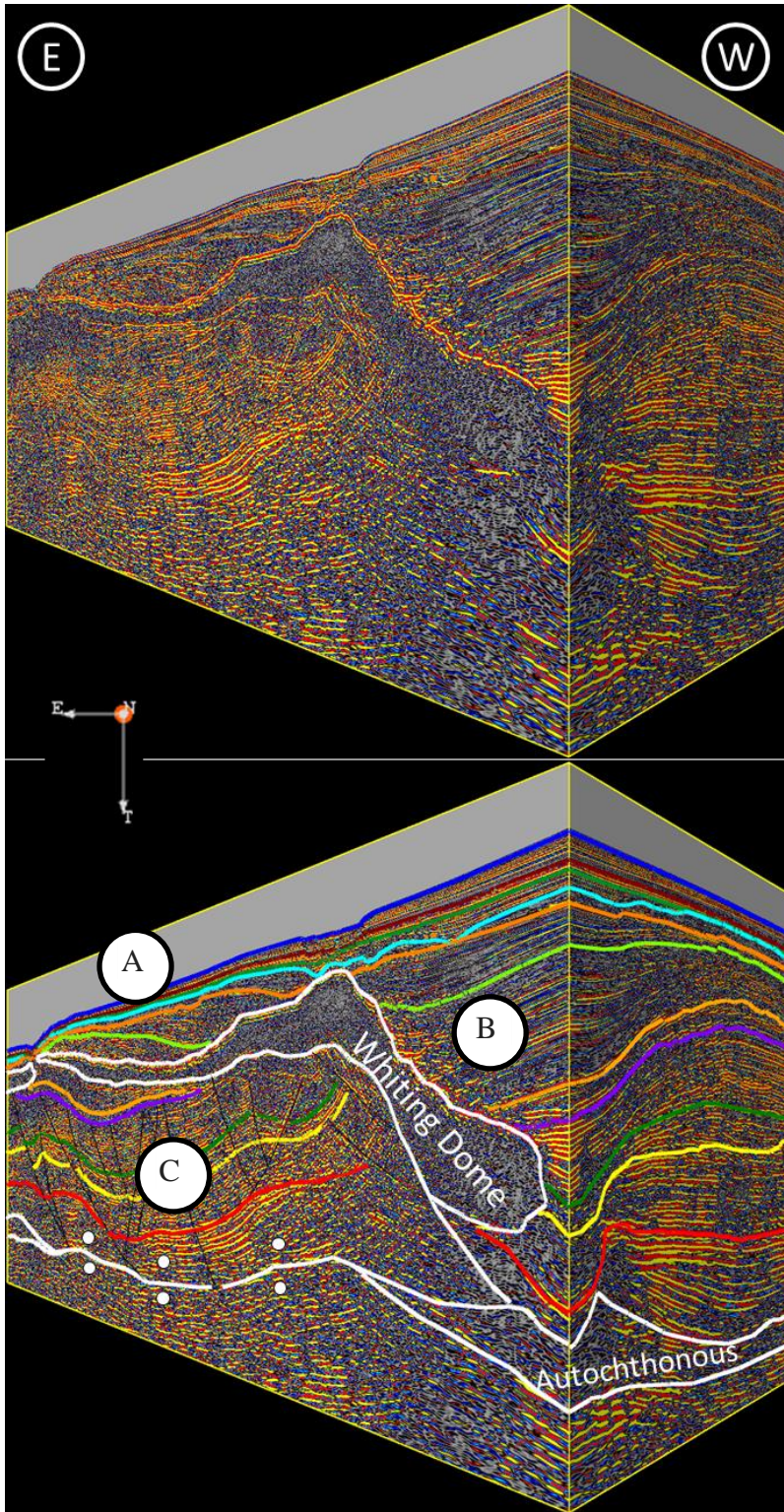


Figure 35: North oriented uninterpreted (top) and interpreted (bottom) block model showing (A) interior of Whiting Dome minibasin, (B) extensional trough above the main salt feeder, and (C) a subsalt interpretation. Whiting Dome feeder tilted basinward due to deposition rates being higher than rate of salt expulsion. Apparent sag in middle of salt structure a result of salt extrusion into simultaneously lowering subsbasin.

The Whiting Dome salt structure has characteristics of multiple salt structure types: shelf- and slope-loaded diapir structures; Roho and counter-regional autochthonous evacuation systems; minibasin and detachment stages; highly rotated, multi-phase transtensional blocks with flip-flop

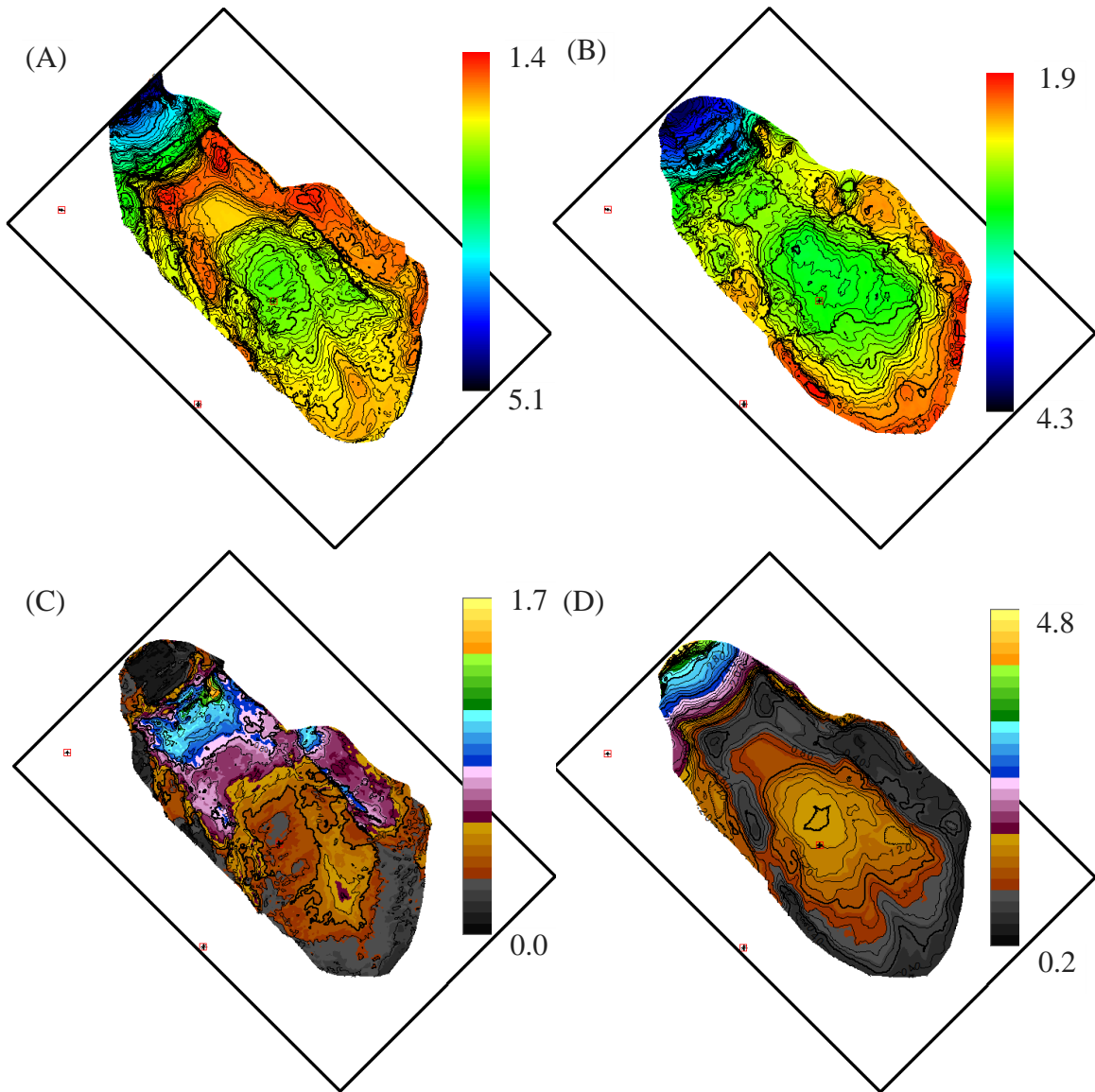


Figure 36: Computer generated grids for top and bottom allochthonous salt (Whiting Dome, only). All figures are in TWT (seconds). (A) Top salt. (B) Base salt. (C) Salt thickness (isochron) across Whiting Dome salt structure. (D) Total sediment thickness (isochron) above Whiting Dome salt structure.

tectonics, salt glacier and flooding; and salt wall inflation. These characteristics will be shown in more detail in interpreted 2D lines within the following sections.

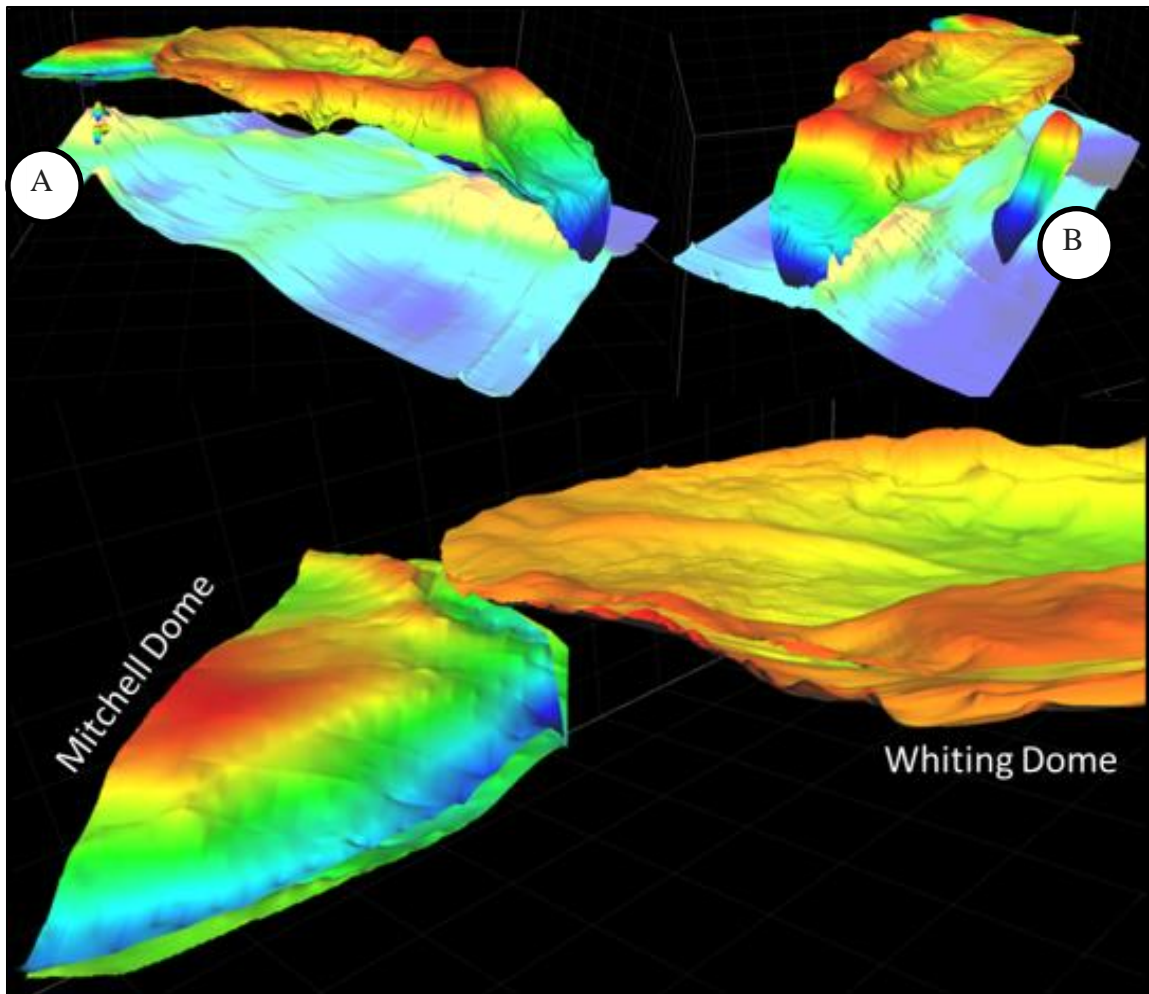


Figure 37: Three dimensional representations of top and bottom allochthonous salt (bright colors) and top autochthonous salt (washed out colors). Ridge structures in autochthonous salt are clearly visible and aligned with salt structures. Four major salt structures in the study area: Whiting Dome (tongue, minibasin, walls), Mitchell Dome (large, detached diapir), an (A) unnamed elongate diapir to the west of the Whiting Dome, and a (B) small unnamed, teardrop-shaped, detached diapir to the east of the Whiting Dome. Toe-of-slope thrusting at the distal end of the Whiting Dome appears to have deformed the top of the Mitchell Dome.

Maastrichtian – TopK (Top-Cretaceous Unconformity to top Louann salt - Figure 38)

- Prograding shelf-slope sediment and aggrading basinal sediment induce salt evacuation and basinward mobilization into ridge structures
- Active halokinesis along major counter-regional faults above rollover syncline features on proximal sides of ridge structures; counter-regional faulting appears to form on landward face of ridge structures
- Downward rotation of onlapping sediments along top of autochthonous salt during late Jurassic and early Cretaceous deposition
- Mid- to late-Cretaceous strata relatively conformable to post-Cretaceous strata in most parts of the study area
- Depositional extent of pre-TopK strata controls lateral mobilization of autochthonous salt; younger strata controls vertical autochthonous and vertical and lateral allochthonous salt mobilization

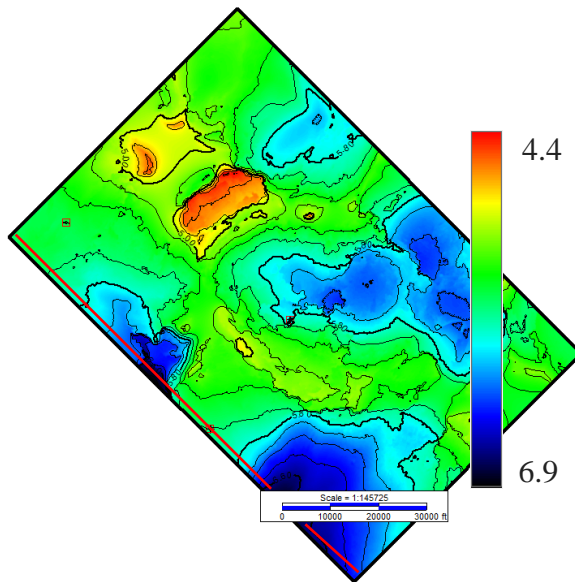
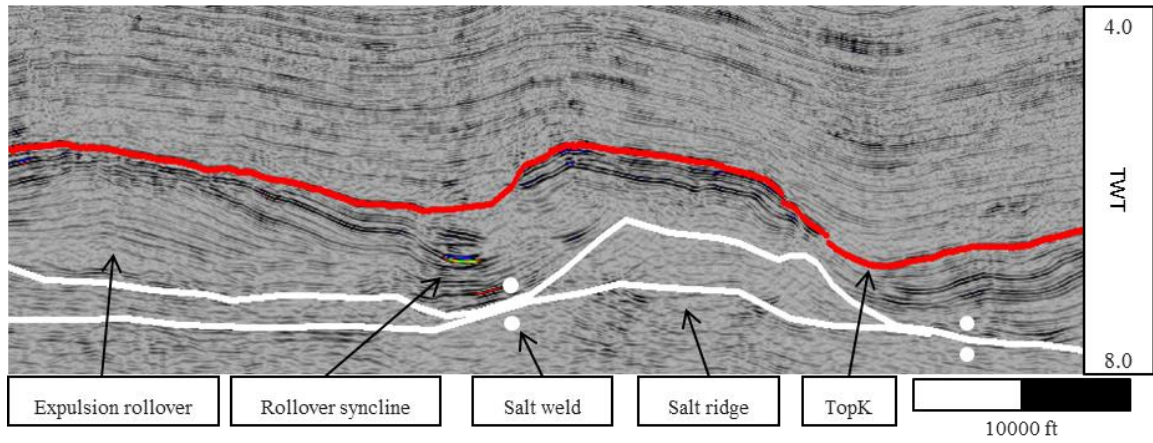


Figure 38: TopK horizon map and picks. (Top) 2D dip oriented line from southwestern section of seismic block. Top Cretaceous unconformity (red) and remnant Louann autochthonous salt (white outline) shown on 2D line. Two white dots indicate areas of salt weld. Roho structures labeled below interpreted section. (Bottom) Time map of top of TopK across the study area. Red line represents location of interpreted 2D line. The TopK closely conforms to the geometry of the underlying salt ridges.

Upper Serravallian - MUM (Middle Upper Miocene to TopK - Figure 39)

- Limited well control – picks made using high amplitude, study area-wide reflector to use for general analysis of section
- Initiation of salt inflation in main feeder causes depositional onlap in the northwestern section of the study area (Figure 40)
- Autochthonous salt flowing from southeast to northwest from the middle of the block to the main feeder created large normal fault complex in strata directly above TopK; possible fault dip polarity shift post-Cretaceous (Figure 41)
- Detachment along top of withdrawing allochthonous salt beginning in late Miocene – early Pliocene
- Halokinesis occurring at a relatively slow, albeit consistent, rate compared to the rest of the stratigraphic column; very little evidence of growth strata along faults; dip of faulting controlled by local direction of salt withdrawal and associated subsidence
- Strata significantly thicker along western shelf margin and in southern corner of study area; no major eastern depositional axis until Upper Miocene explains unbalanced shelf margin deposition; southern corner sub-basin deposits indicative of initial expulsion of autochthonous salt into proto-Mitchell Dome structure

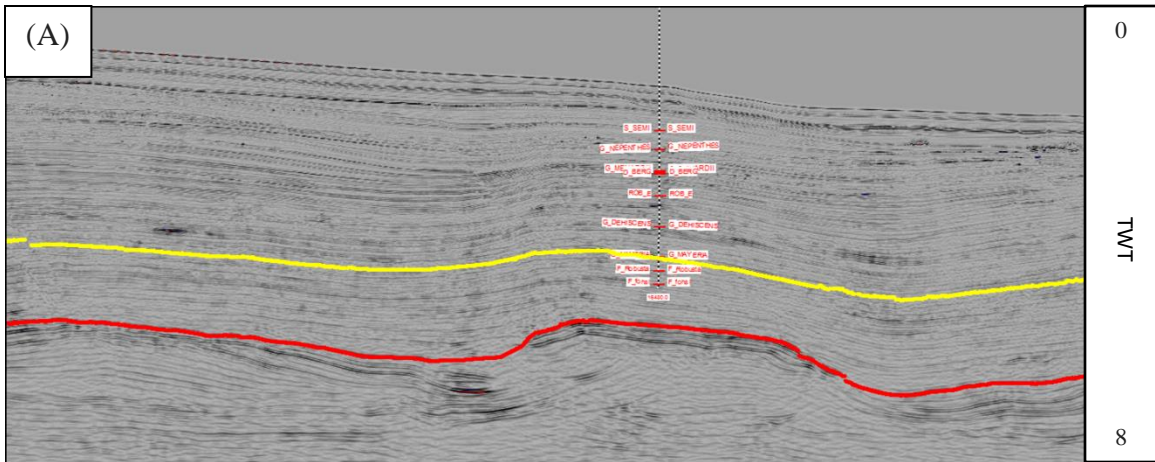
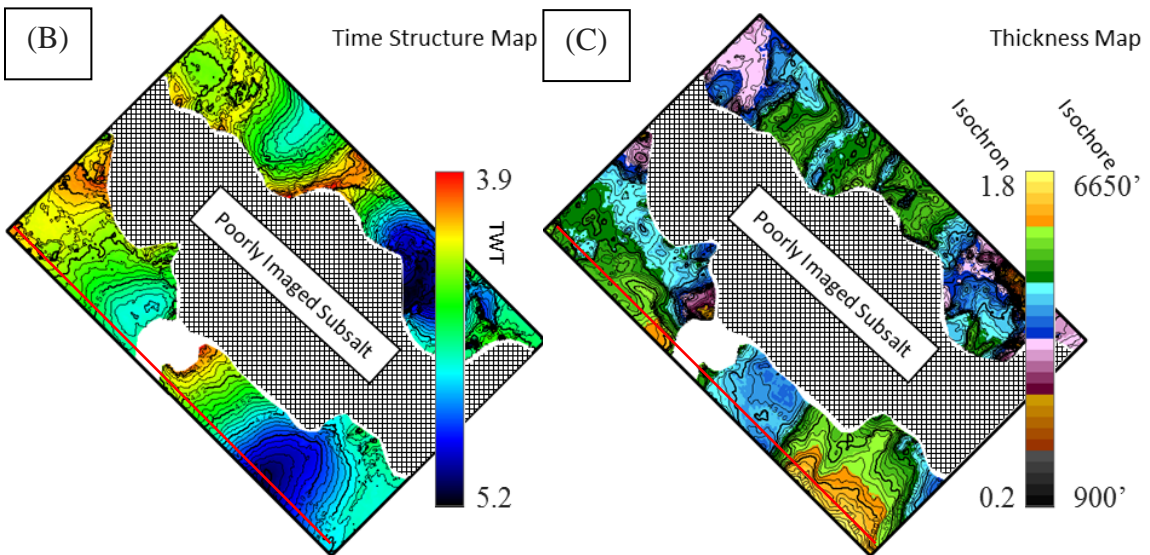


Figure 39: MUM horizon maps and picks. (A) Dip line with top MUM (yellow) and well log for BP's OCS-G 7926 #1 (API: 608174049800); top set at major reflector directly below *Globorotalia mayeri*. (B) Time-to-top map for MUM. General chronozone structure similar to that of younger strata. (C) Isochron and isochore map. Thickest areas of MUM deposition in southern corner of study area over Mitchell Dome evacuation area. Most likely signifies earlier expulsion of autochthonous salt below Mitchell Dome than that of Whiting Dome. Constant velocity of 7500 ft/s used to convert time to depth.



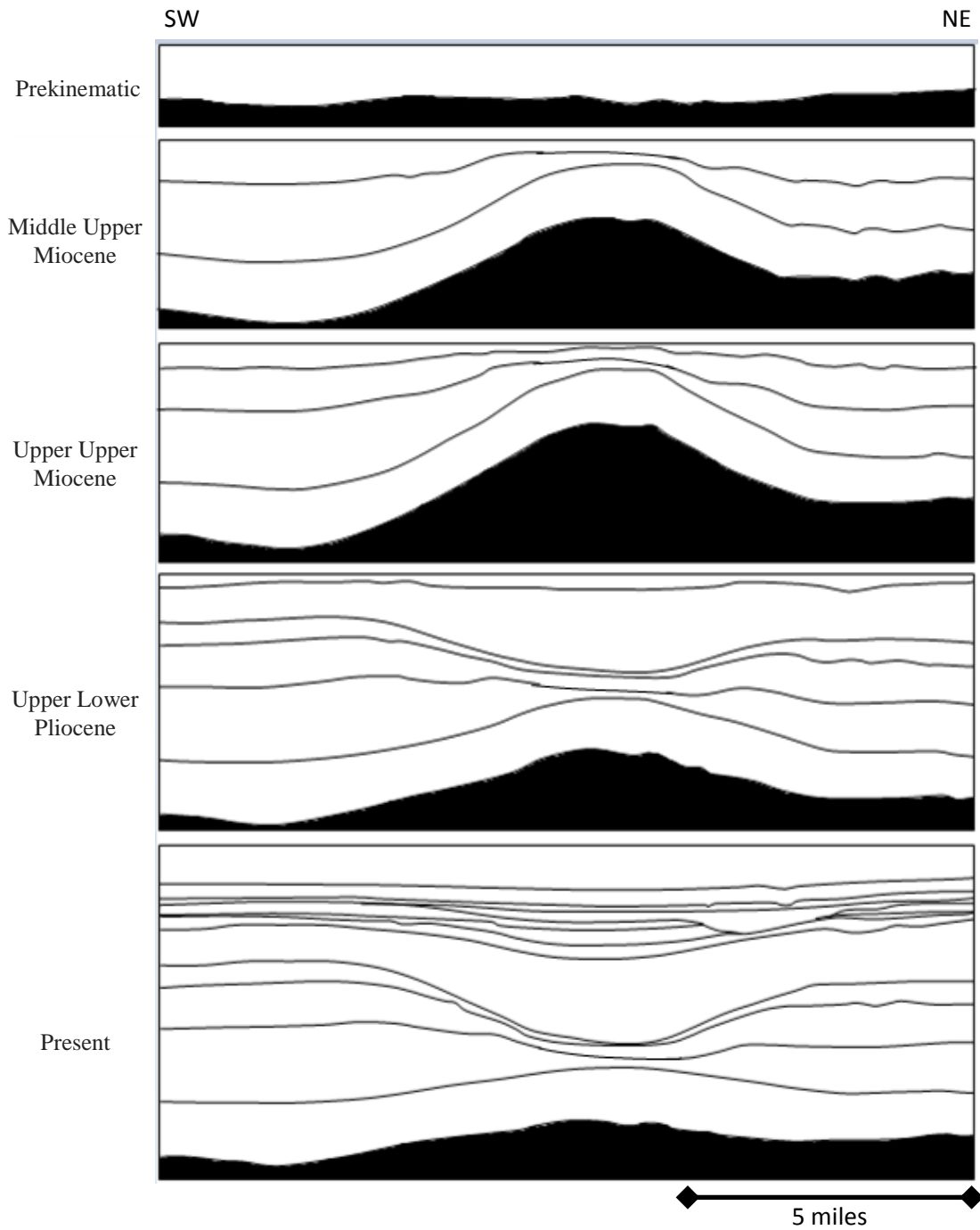


Figure 40: Non-balanced reconstruction of seismic line perpendicular to salt flow through main feeder. Evidence for inflation of salt feeder from mid-Miocene to early Pliocene, followed by rapid deflation ending in the late Pliocene to early Pleistocene.

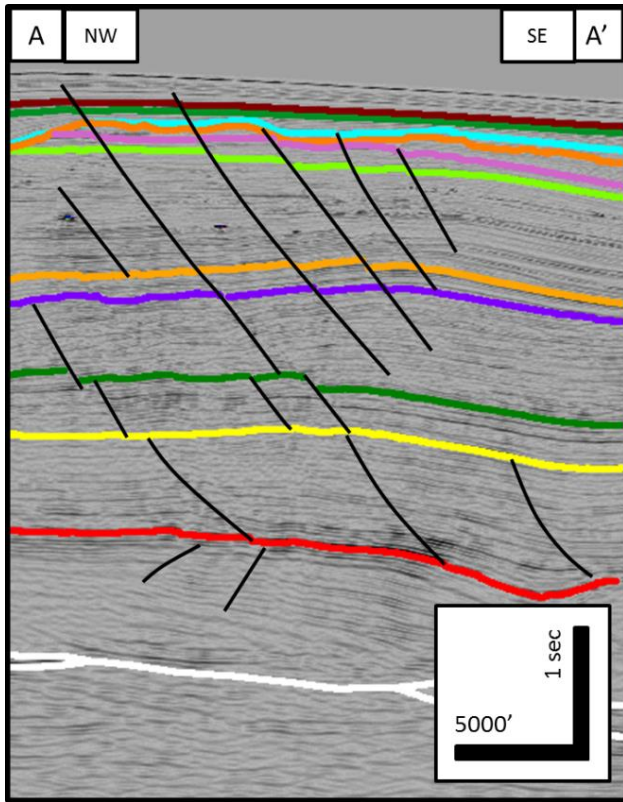
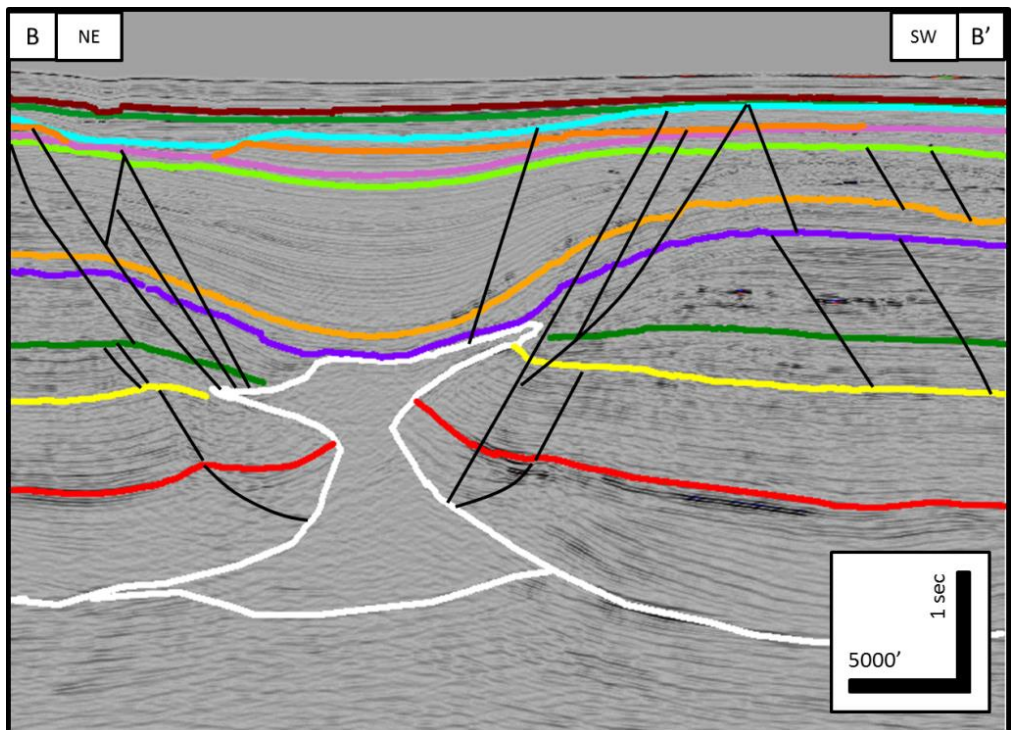
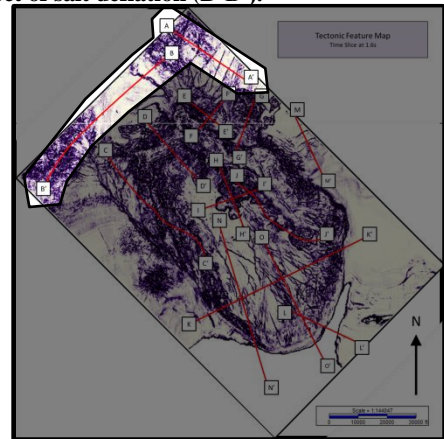


Figure 41: Dip oriented (top – A-A') and strike oriented (bottom – B-B') interpreted 2D seismic lines showing fault dip orientation outboard of the Whiting Dome. Shift from landward dipping faults during the Jurassic and Cretaceous to basinward dipping faults post-Cretaceous (A-A'). Both sets of faults are due to mobilization of salt in the area; however, the shift from primarily lateral expulsion to vertical mobilization caused a matching change in dip polarity. The faulting in the strata directly adjacent to and above the main Whiting Dome salt feeder clearly demonstrates the effect of salt deflation (B-B').



Upper Tortonian - MUU2 (Upper Upper Miocene – 7.12ma - Figure 43)

- Some well control outside of Whiting Dome; however, subsalt reflectors are heavily washed out
- First major influx of sediment from Central Mississippi and Eastern Mississippi/Tennessee River depositional axes
- Noticeable reflector offset along normal faults at shelf margin; most likely due to increased rate of salt evacuation-induced subsidence and inflation of salt feeders
- Onlap of strata onto inflating main feeder still occurring
- Non-shelf strata thickest around Mitchell Dome feeder/distal end of Whiting Dome; evidence for substantial inflation of proto-Mitchell Dome; sub-basins on flanks of proto-Mitchell Dome infilled to limit of contemporary subsidence
- Massive deposits in western half of study area in high contrast to far more restrained depisode in the eastern half; no evidence for truncation in eastern shelf region, but deposits are significantly thinner there than on the western shelf; highly tilted blocks over shelf-slope contact

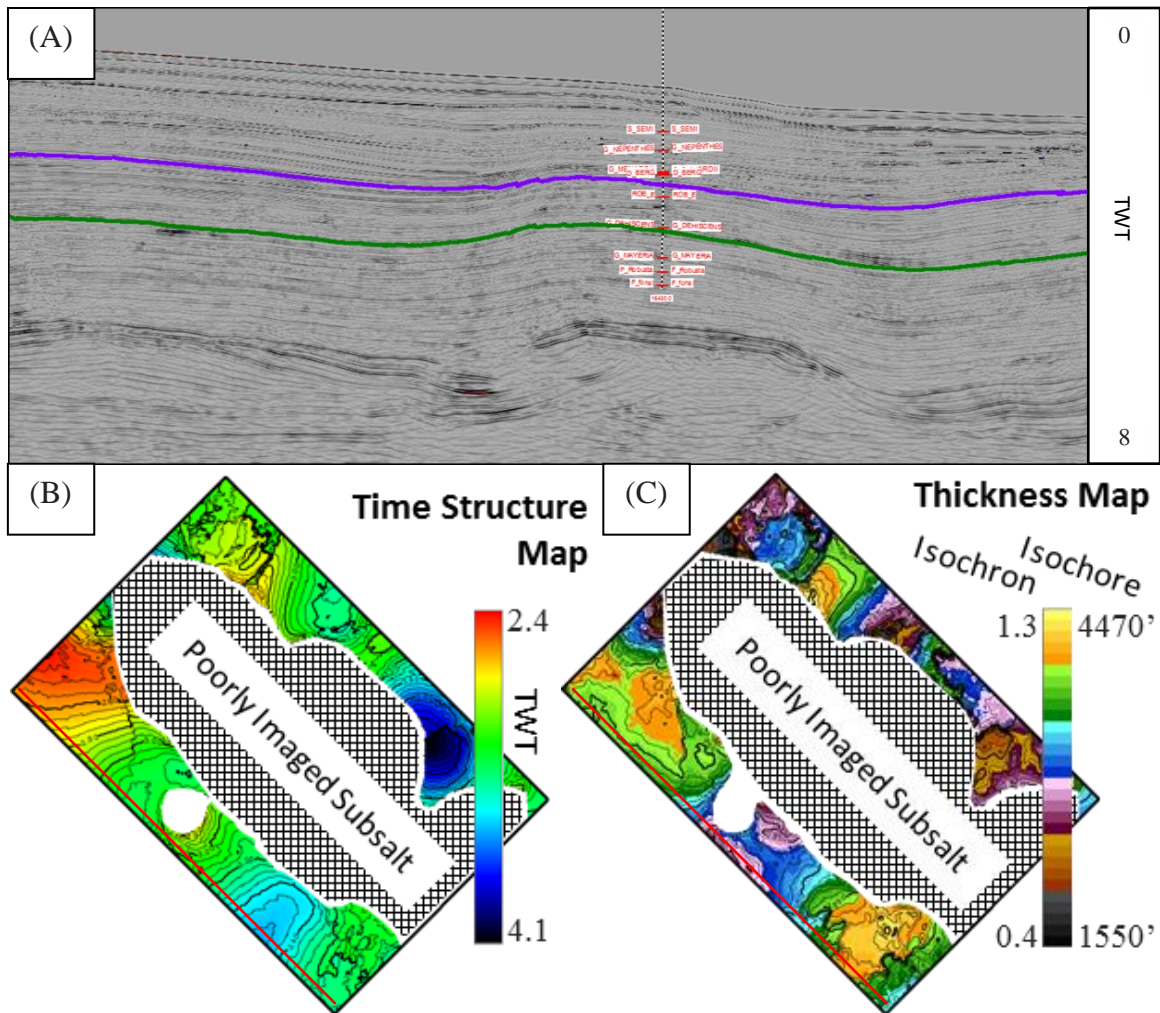


Figure 43: MUU2 horizon maps and picks. (A) 2D dip oriented seismic line showing top (purple) and base (dark green) MUU2. (B) Time structure map for the top of the MUU2 horizon. Significant difference in depths of two sub-basins on northern and western flanks of Mitchell Dome indicate extreme preferential loading due to available accommodation space above expelled autochthonous salt. (C) Isochron and isochore map: constant velocity of 7000 ft/s used for time-depth conversion.

Messinian - MUU1 (Upper Upper Miocene – 5.23ma - Figure 44)

- Good well control from MUU to PLL; one well penetrates base salt in Whiting Dome; very brief sections of PL and MUU1 strata before well completes in MUU2 strata
- Inflation of main salt feeder slows; possible initiation of salt extrusion phase during this depisode
- Continuing onlap of strata onto main feeder
- Minor deformation of strata due to inflation of salt on eastern flank of Mitchell Dome
- Strata thins to onlap in eastern half of study area near small detached diapir and associated evacuation sub-basin
- Western shelf and slope again have much thicker deposition; most likely due to continued rise of diapiric salt feeder into a paleohigh thereby effectively blocking deposition into the salt withdrawal basin

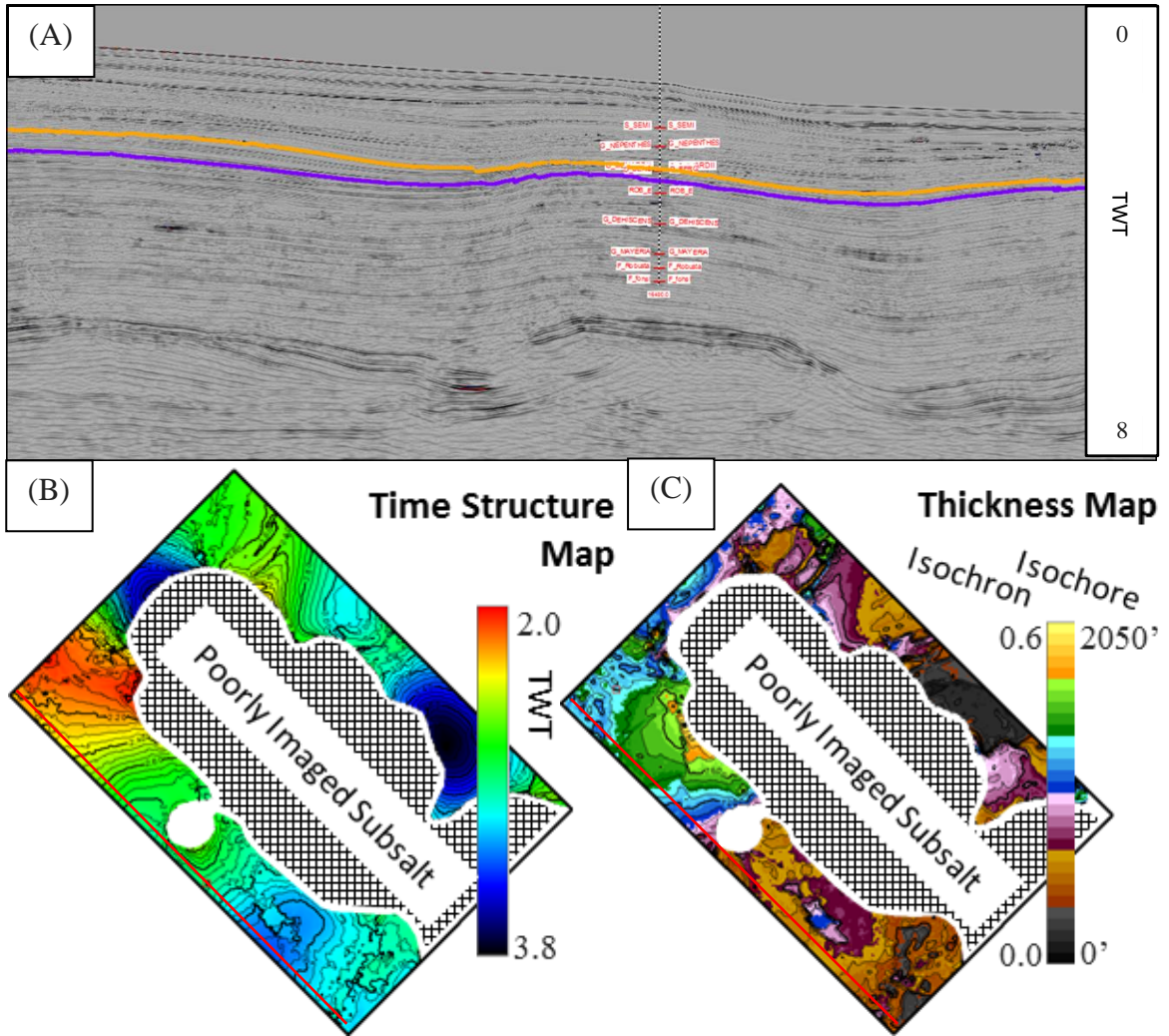


Figure 44: MUU1 horizon maps and picks. (A) 2D dip oriented seismic line showing the top of the MUU1 horizon (light orange). (B) Time structure map of top MUU1. First well-imaged depiside above deflating salt feeder. Significant landward translation of sub-PL sediments along salt detachment fault above salt feeder during Pliocene. (C) Isochron map and isochore map: constant velocity of 6800 ft/s used for time-depth conversion. Thickest sediments along western shelf margin; these are primarily aggrading features.

Zanclian - PL (Lower Pliocene - Figure 45)

- First depisode with primary deposition of sediment onto eastern half of study area
- Four major salt tectonic/depositional phases during this depisode:
 - Pre-extrusion phase: heavy sedimentation above salt feeder and into remnant salt evacuation basin induces increased salt flow during early PL; diapiric feeder breaches the sea floor and begins to fill remaining accommodation space in evacuation basin
 - Syn-extrusion phase: transition to deflation of main salt feeder as salt flow rate dips below rate of deposition; extreme subsidence and creation of minibasin along northern face of feeder (extensional trough); some early to mid-PL deposits around flanks and distal end of extending salt tongue
 - Pre-gliding phase: eventually, mid- to late-PL deposits crest proximal end of new salt tongue and deposit onto relatively flat surface; initiation of PL strata sinking into salt tongue
 - Syn-gliding phase: continuing deposition of late PL strata prompts pre-gliding PL strata migration basinward on top of salt while simultaneously sinking into top of salt tongue; this translation begins development of growth faulting on both landward and basinward sides of feeder

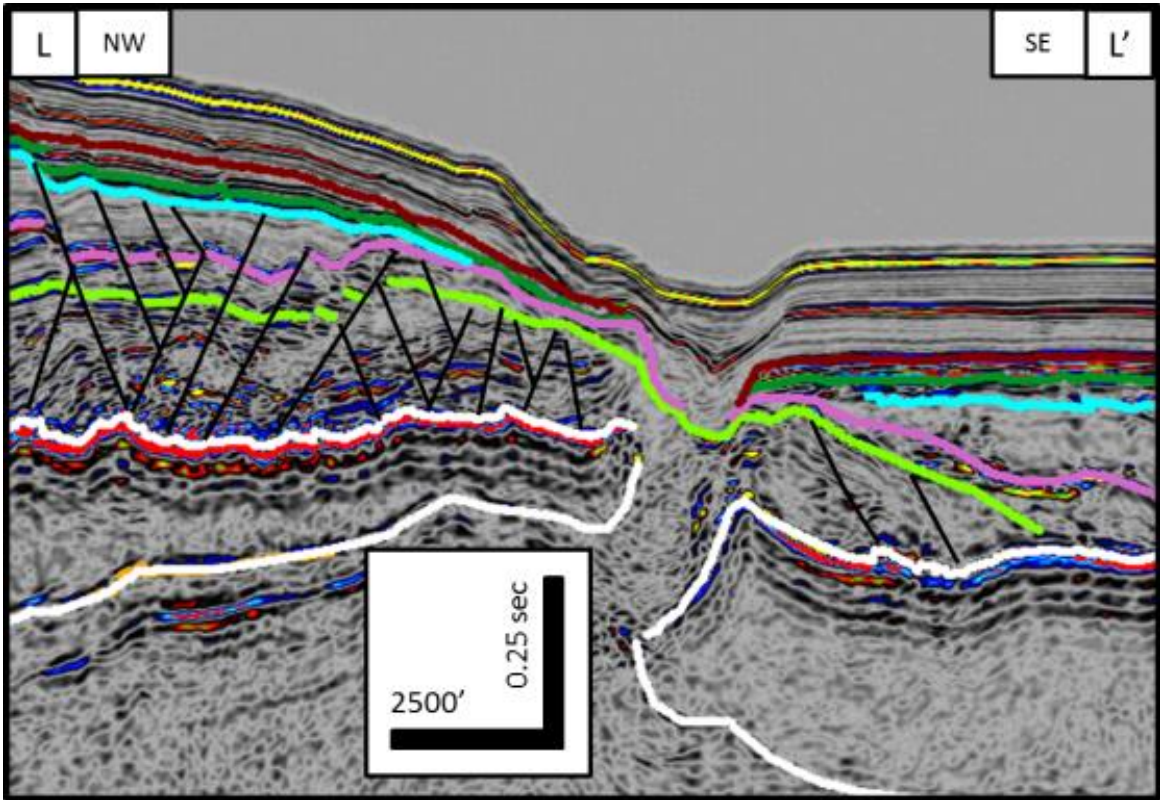


Figure 46: Collision of gliding Whiting Dome (left) into expanding Mitchell Dome (right). Sediments heavily deformed between the two salt structures.

- This transition is also marked by the development of dendritic faulting; these faults are generally seen as markers for orogenic (thrust) activity; in this incidence, they were more than likely developed by toe of slope compressional stressors due to density driven subsidence of the PL growth strata and related rotation of overlying strata. Evidence for reverse offset is difficult to ascertain as these faults have currently reactivated as normal faults due to the underlying salt's subsidence
- Rotated block above proximal end of Mitchell Dome is very similar to seismic signature of Pliocene deposits (PL to PUU)(Figure 46). This could signify prior

continuity of salt between two salt structures. However, it is more likely that the Whiting and Mitchell Domes were never a single, continuous structure. Due to concurrent emplacement of both salt structures, higher sediment load around the Whiting Dome, and the Whiting Dome's "protection" of the Mitchell Dome from incoming deposition, the most likely scenario involves the Whiting Dome being emplaced, stretched, and eventually moved closer to the Mitchell Dome. This scenario is supported by evidence for current toe of slope thrusting of

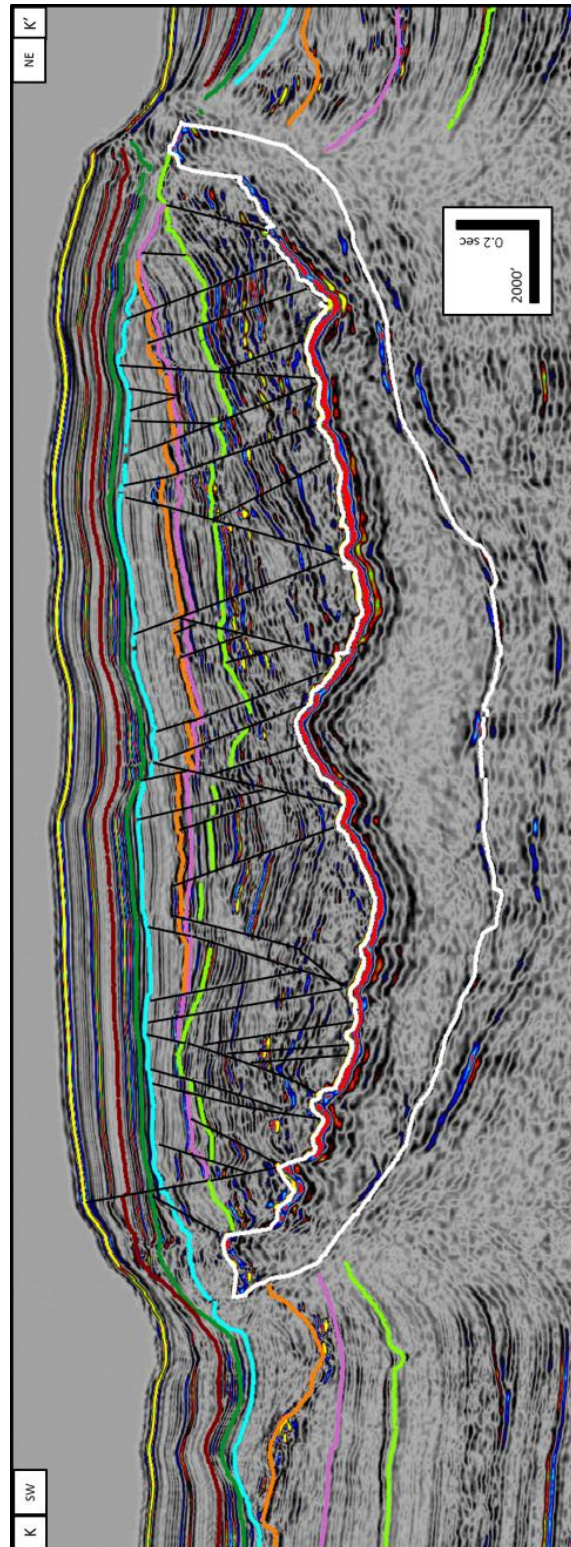


Figure 47: Cross-section of western and eastern sub-basins with the Whiting Dome minibasin.

sediment on the distal edge of the Whiting Dome being thrust over the proximal edge of the Mitchell Dome due to basinward gravity gliding of the Whiting Dome salt structure (Figure 35) and the division of the Whiting Dome minibasin into two roughly equivalent sub-basins where the gliding sediments impacted the Mitchell Dome (Figure 47, Figure 48, Figure 49, Figure 50).

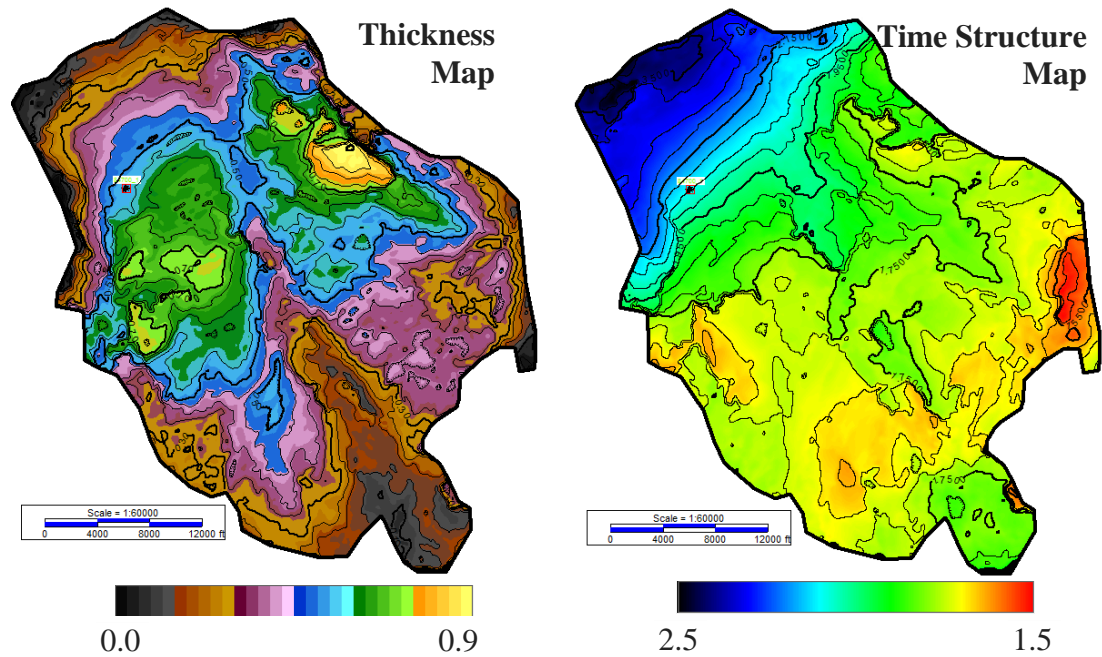


Figure 48: Whiting Dome minibasin suprasalt PL maps. The minibasin province is divided into two subequal halves: eastern and western. (Left) Isochron. (Right) Time structure.

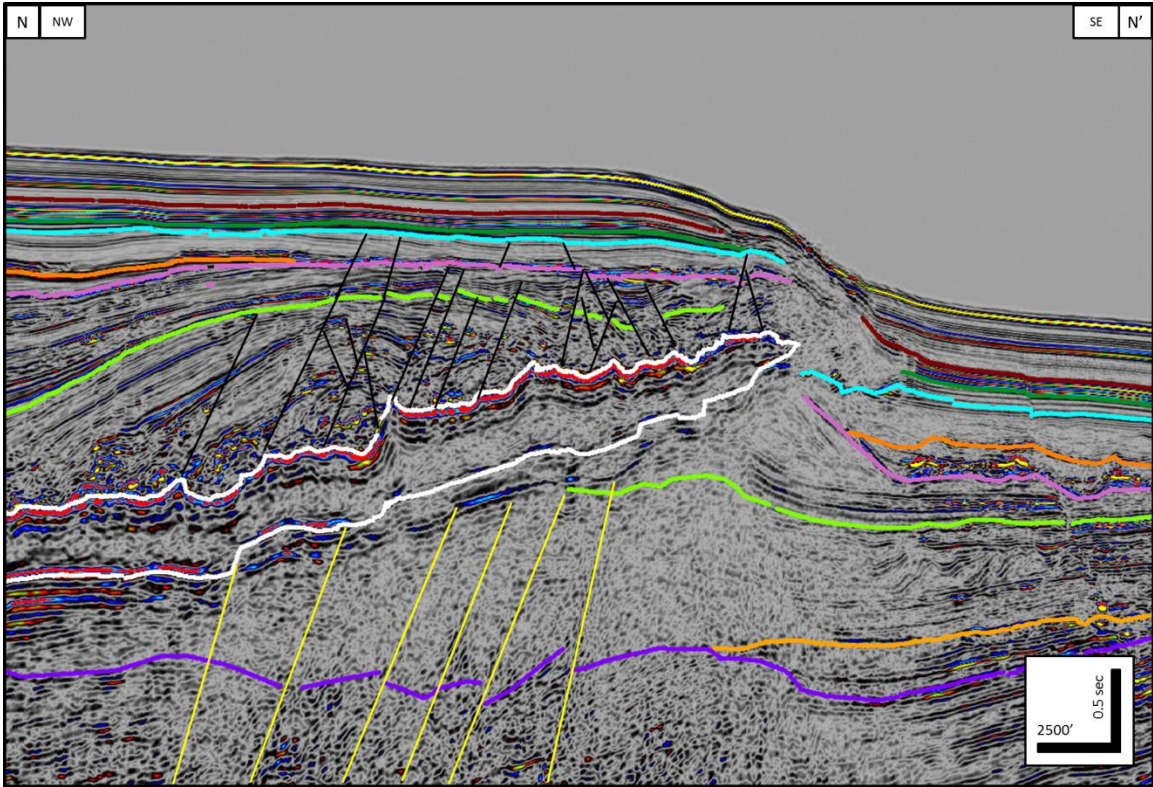


Figure 49: Dip oriented line through the center of the western sub-basin within the Whiting Dome minibasin. Note the relatively high amount of suprasalt deformation and low amount of subsalt deformation as compared to their counterparts in the eastern sub-basin.

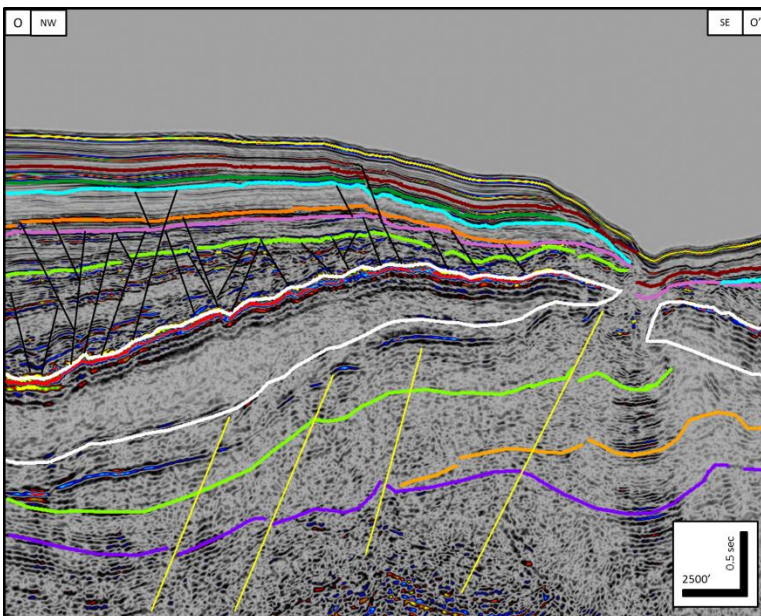


Figure 50: Dip oriented line through the center of the eastern sub-basin within the Whiting Dome minibasin. Extensive deformation of subsalt strata but relatively little visible deformation of suprasalt strata, especially when compared to that of the western sub-

Piacenzian - PUL (Lower Upper Pliocene - Figure 51)

- Subsidence in extensional trough above salt feeder continues but slowing
- Thickest section is in interior of minibasin above salt tongue
- Thins above PL high in middle of salt dome, but evidence for extended deposition onto Mitchell Dome

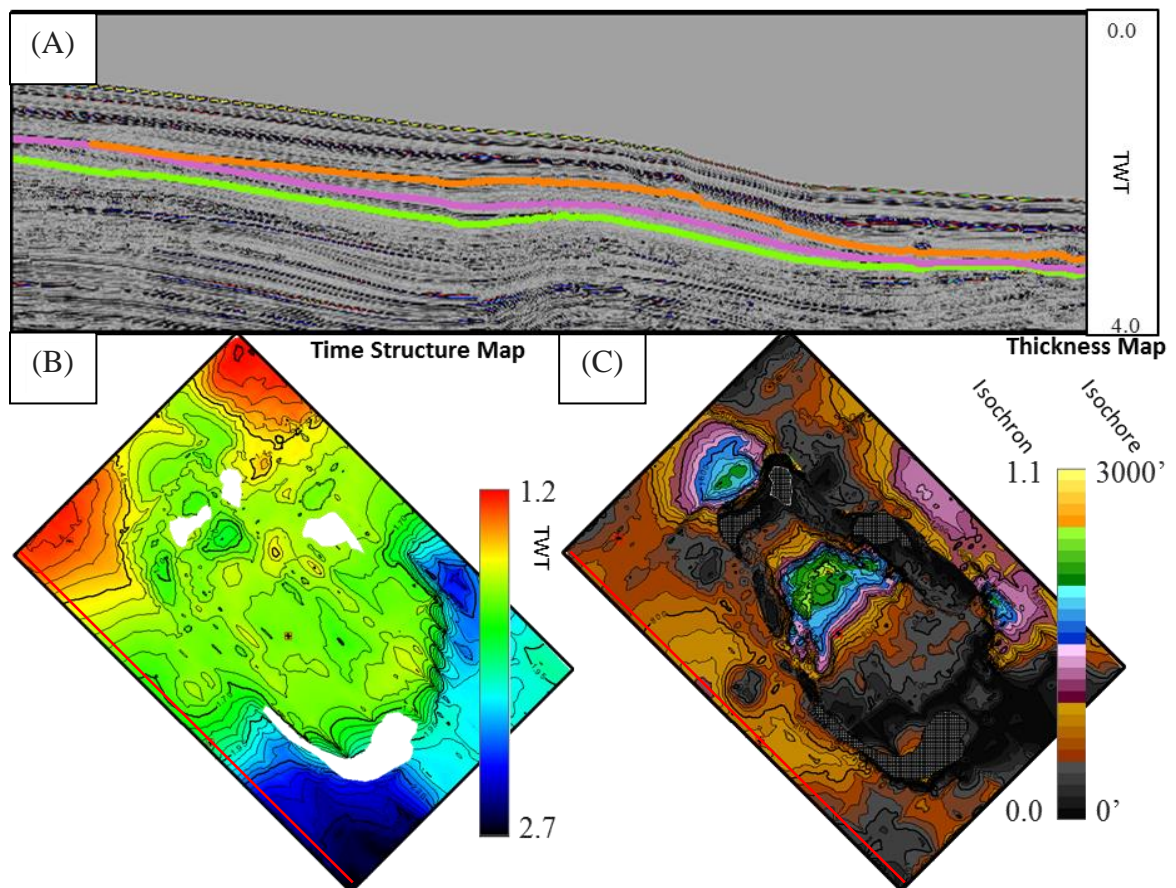


Figure 51: PU horizon maps and picks. (A) 2D dip oriented seismic line showing the top of the top PUL, top PUU, and base PU horizons (medium orange, pink, and bright green). (B) Time structure map for top PU. Southward translation of minibasin sediments has significantly slowed by the end of the Pliocene. Heavy truncation of already thin Upper Pliocene deposits at distal end of structure. (C) Isochron and isochore map: constant velocity of 5450 ft/s used for time-depth conversion. Primary deposition located above the two detachment zones above salt. A secondary depocenter exist along the eastern edge of the study area.

- Continuing trend of listric fault fueled growth strata. The interior of the Whiting Dome minibasin is, by far, the thickest PUL deposit within the study area. In the area immediately between the twin peaks near the proximal end of the salt complex, there is a noticeable shift in the depocenter of the minibasin mouth. The west to east shift marks a failure of the eastern salt horn to migrate any further vertically, thereby triggering more rapid subsidence on that side and increased inflation of the western flank. Onlapping strata terminate onto PL structural high at the distal end of the minibasin.
- Infilling of rotated PL graben structures in the distal end of the transtensional zone on the western flank of the Whiting Dome salt structure but significant lack of infill in the proximal portion indicates at least a two phase sequence for the zone (Figure 53).

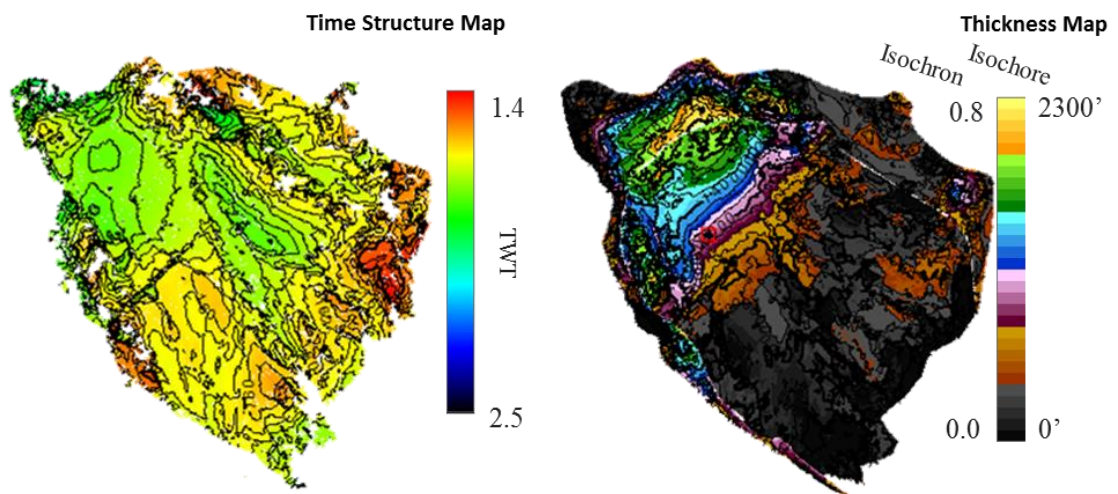


Figure 52: Time structure (left) and thickness map (right) of suprasalt PUL deposits.

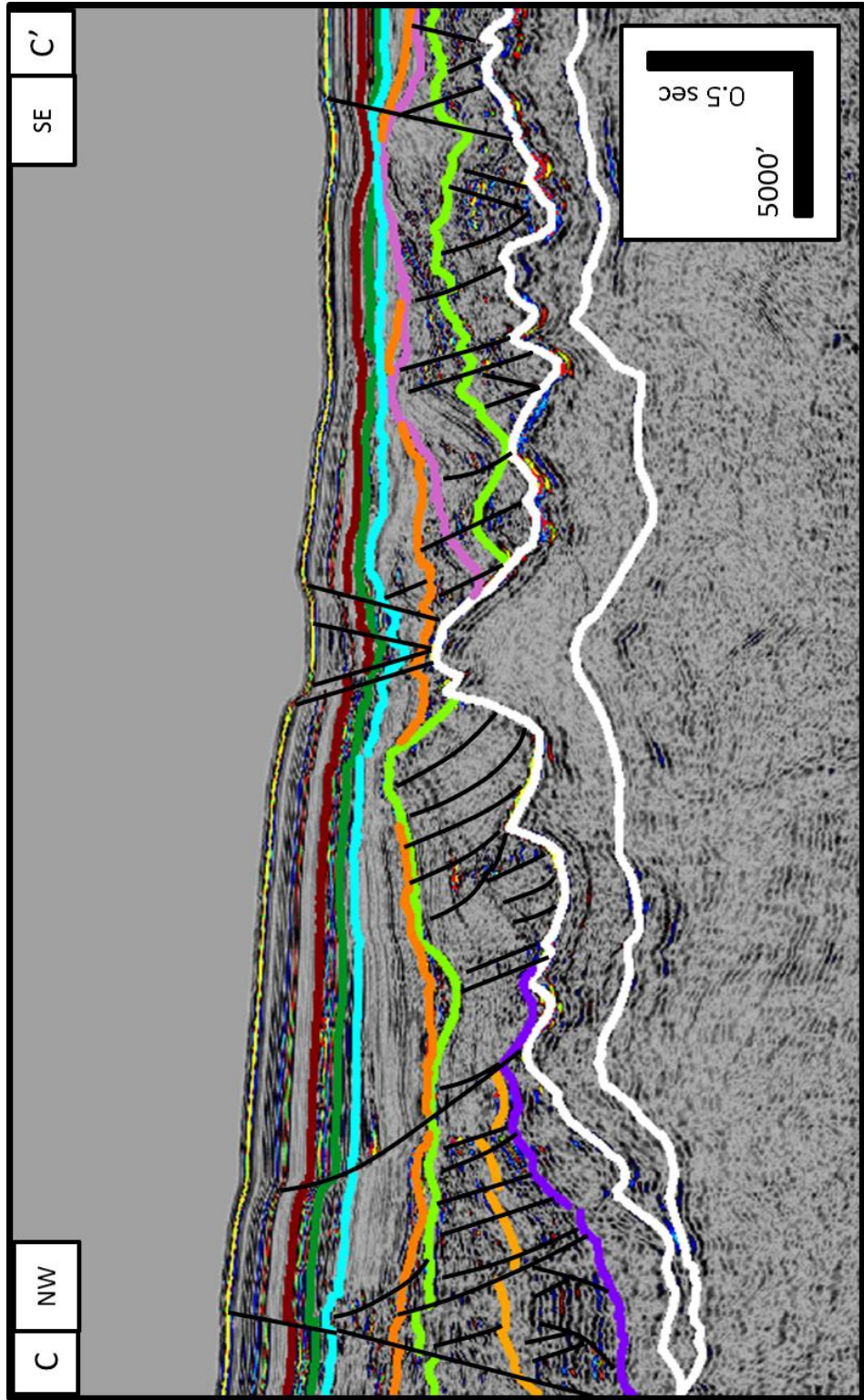


Figure 53: Transensional zone along western flank of the Whiting Dome salt structure.

Gelasian - PUU (Upper Upper Pliocene - Figure 51)

- Subsidence above salt feeder continues but slowing
- Relatively thick sequence across middle of study area and extreme thinning and truncation in south
- Final major growth sequence in minibasin above salt tongue
- Proximal growth trend continues but slows by the end of the PUU (Figure 54). Deposition thins above the PL structural high, and is

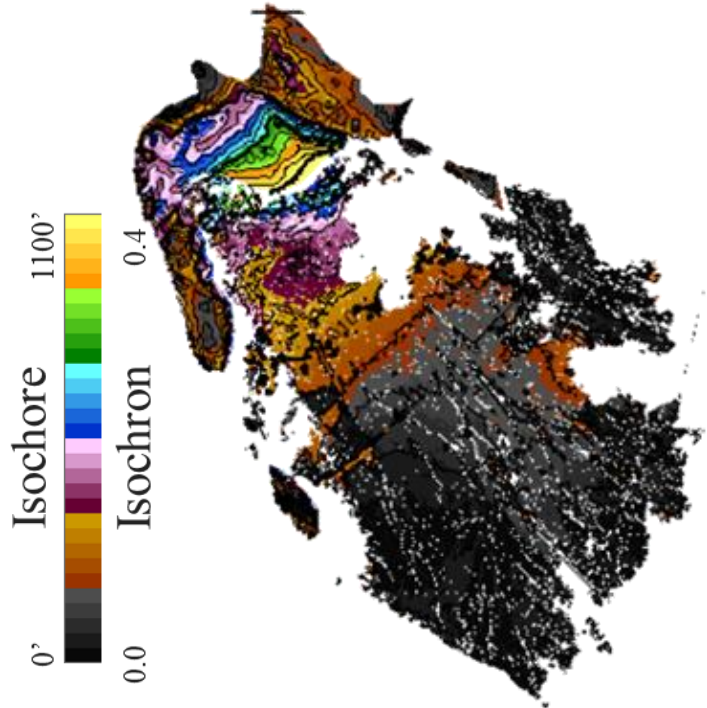


Figure 54: Thickness map of suprasalt PUU deposits in Whiting Dome structure. Note the absence of significant amounts of strata along the eastern flank. These areas are decimated by slump scarring caused by release of hydrostatic pressure during the transition to a significant drop in sea level at the beginning of the Pleistocene.

heavily truncated by PLL deposits and slump scars (Figure 55). Similar to the PUL, there is a dramatic depocenter shift; this time the center of the mouth shifts back to the west. This is caused by stabilization of the proximal end of the salt structure as salt flow from the feeder slows.

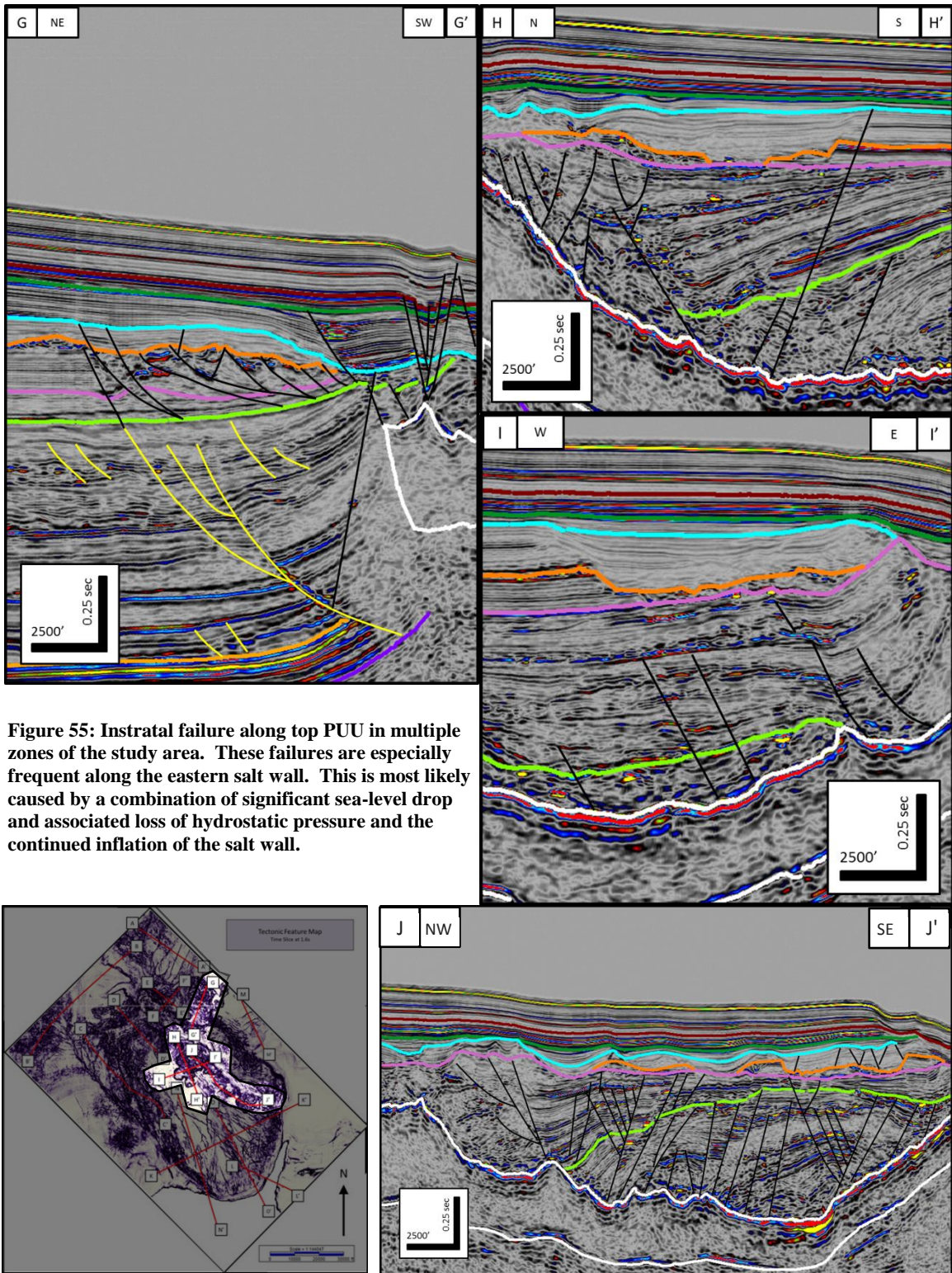


Figure 55: Intratrustal failure along top PUU in multiple zones of the study area. These failures are especially frequent along the eastern salt wall. This is most likely caused by a combination of significant sea-level drop and associated loss of hydrostatic pressure and the continued inflation of the salt wall.

Calabrian - PLL (Lower Pleistocene - Figure 56)

- Relatively thin deposition across study area
- Subsidence above main feeder has ceased
- Erosional horizon at top of sequence
- Possible deep water fan system (three lobes) on western flank of Mitchell Dome
- Beginning of PLL marked by massive amount of subsidence at proximal end of the minibasin. This subsidence appears to be caused by subsalt faulting and subsequent dropping of the thickest non-diapiric portion of the proximal salt structure
- Base PLL-top PUU is conformable outside of structure but visibly disconformable in areas directly around and above the Whiting Dome. Large amounts of accommodation space are created during this time

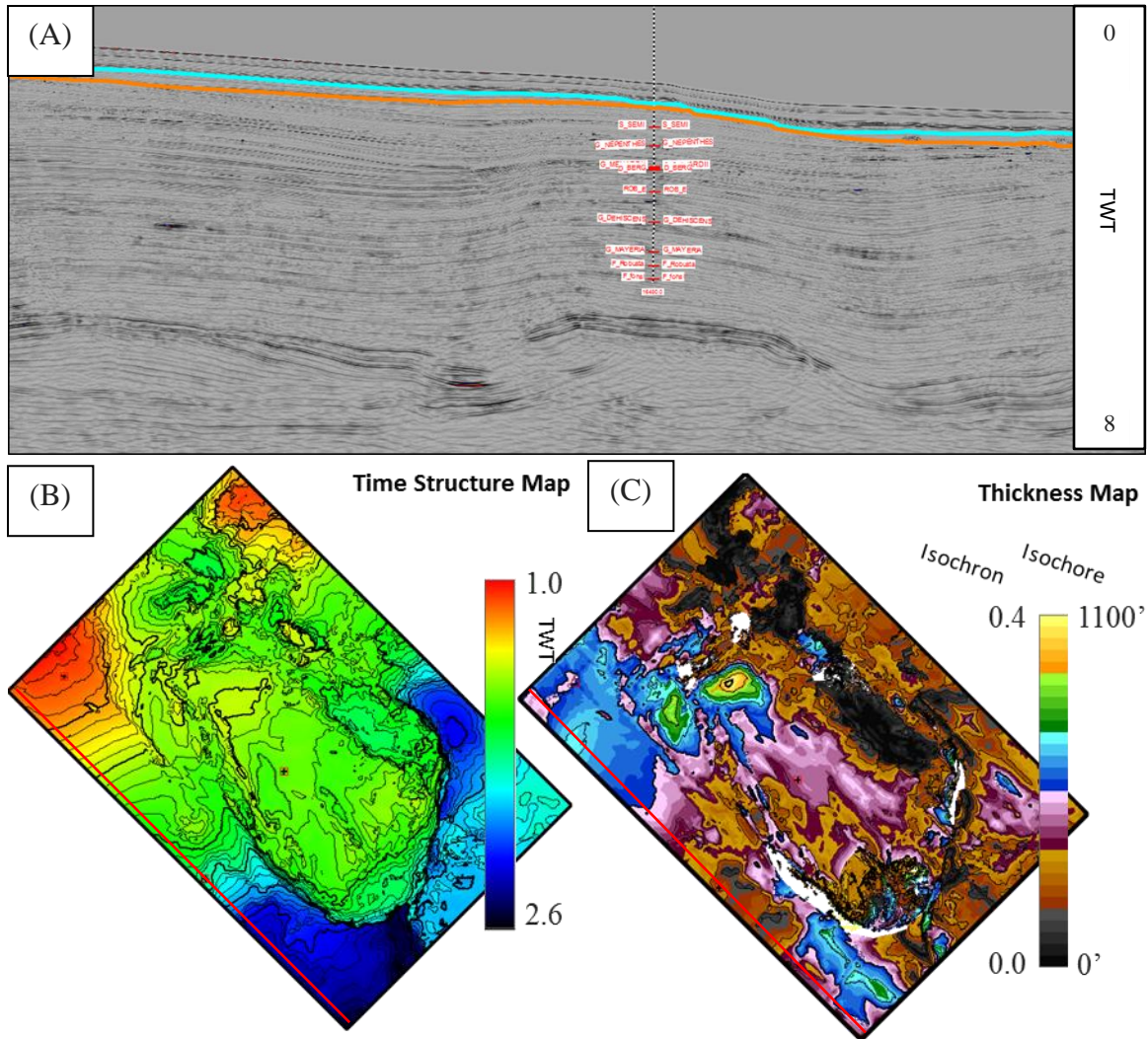


Figure 56: PLL horizon maps and picks. (A) 2D dip oriented seismic line showing the top (cerulean) and base (dark orange) of the PLL horizon. (B) Time structure map for top PLL. Southward translation of minibasin sediments has ceased by the end of the Lower Pleistocene. Significant aggradational unit; very little to no progradation in study area. (C) Isochron and isochore map: constant velocity of 5300 ft/s used for time-depth conversion. Final major depositional sequence in extensional troughs above detachment zones. Deposition has shifted back to the western half of the study area.

Lower Ionian - PLM (Middle Pleistocene - Figure 57)

- Extremely thin deposition across most of study area
- Thick depocenter between two peaks at northwestern end of Whiting Dome; salt withdrawal from center inflates up peaks, creates another very small minibasin
- Second depocenter at southeast end of Whiting Dome
- Tertiary depocenters located along western flank of Mitchell Dome and a small base of slope fan/channel system off the southwest flank of the Whiting Dome
- Primarily infilling deposits above Whiting Dome. Can be seen above PUU slump areas and incising PLL deposits in extensional trough above Whiting Dome feeder

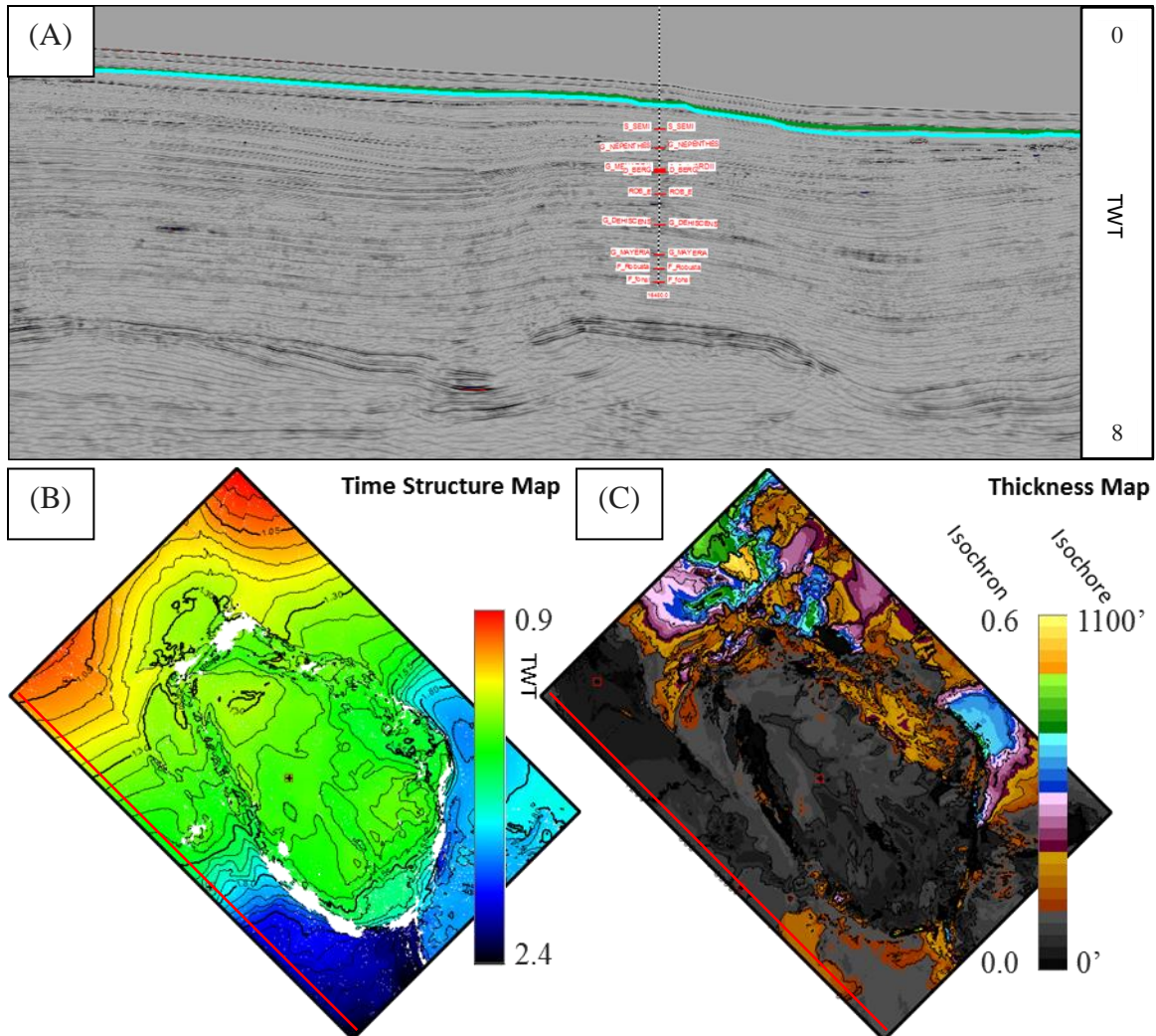


Figure 57: PLM horizon maps and picks. (A) 2D dip oriented seismic line showing the top (dark green) and base (cerulean) of the PLM horizon. (B) Time structure map for top PLM (C) Isochron and isochore map: constant velocity of 5200 ft/s used for time-depth conversion. Primarily infilling deposide with initial development of canyon structures in northern section of study area; can be seen above PUU slump features and incising PLL deposits in extensional trough area. Deposition has shifted back to the eastern half of the study area.

Upper Ionian - PLU (Upper Pleistocene - Figure 58)

- High amplitude band across much of study area; possible shore zone/shallow submarine depositional system in accordance with Galloway maps
- Continued development of minor bypass channels in northern portion of study area and along flanks of Whiting Dome structure

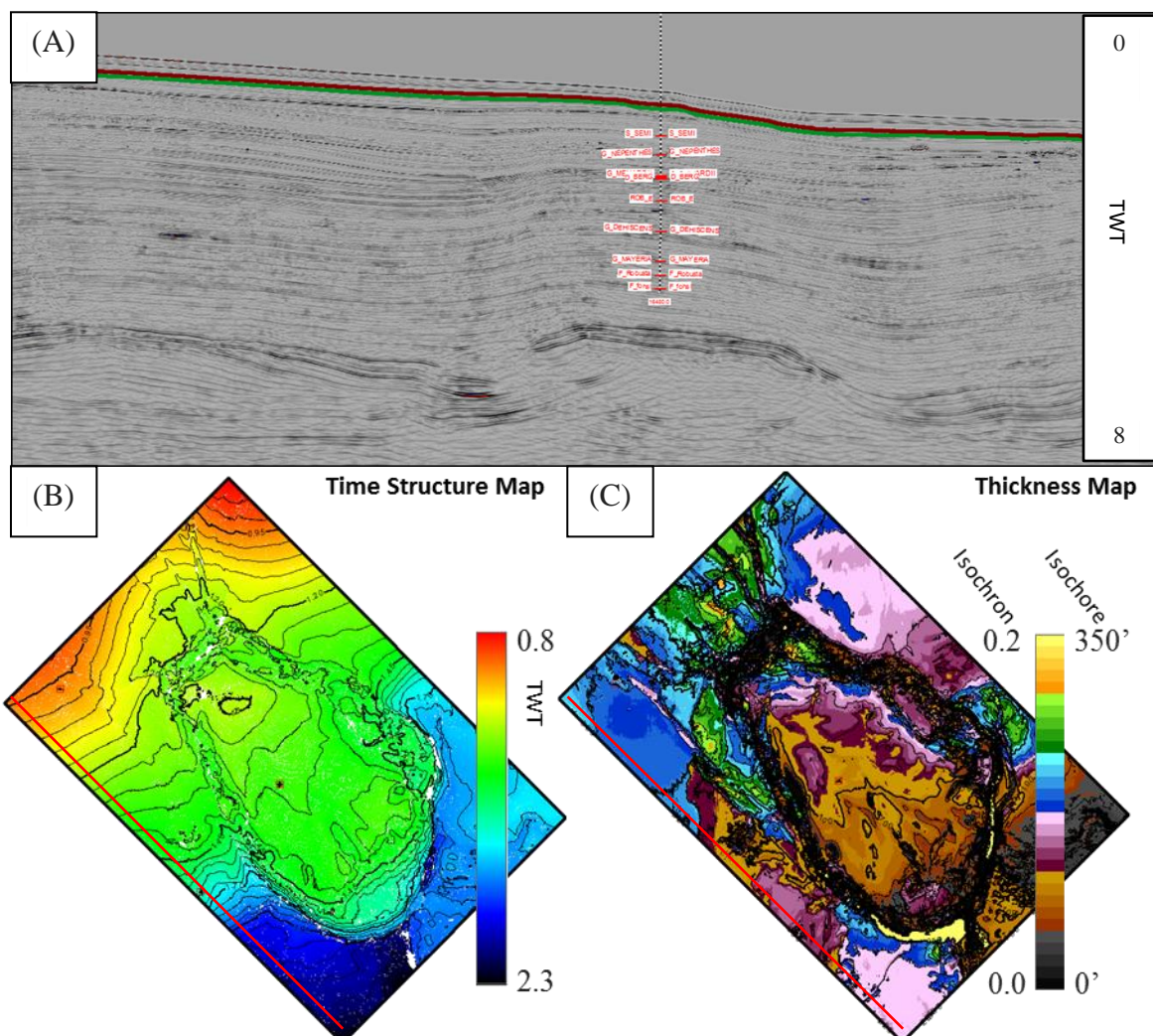


Figure 58: PLU horizon maps and picks. (A) 2D dip oriented seismic line showing the top (dark red) and base (dark green) of the PLU horizon. High amplitude sands across much of the study area. Represents significant geohazard for hydrocarbon exploration. (B) Time structure map for top PLU (C) Isochron and isochore map: constant velocity of 5100 ft/s used for time-depth conversion.

- PLU covers the majority of the study area in a relatively consistent layer. Thins at toe of Whiting Dome bulge. Limited structural activity during this time period. Some growth strata seen in crestal fault system above diapir structures near proximal end of Whiting Dome (Figure 59)

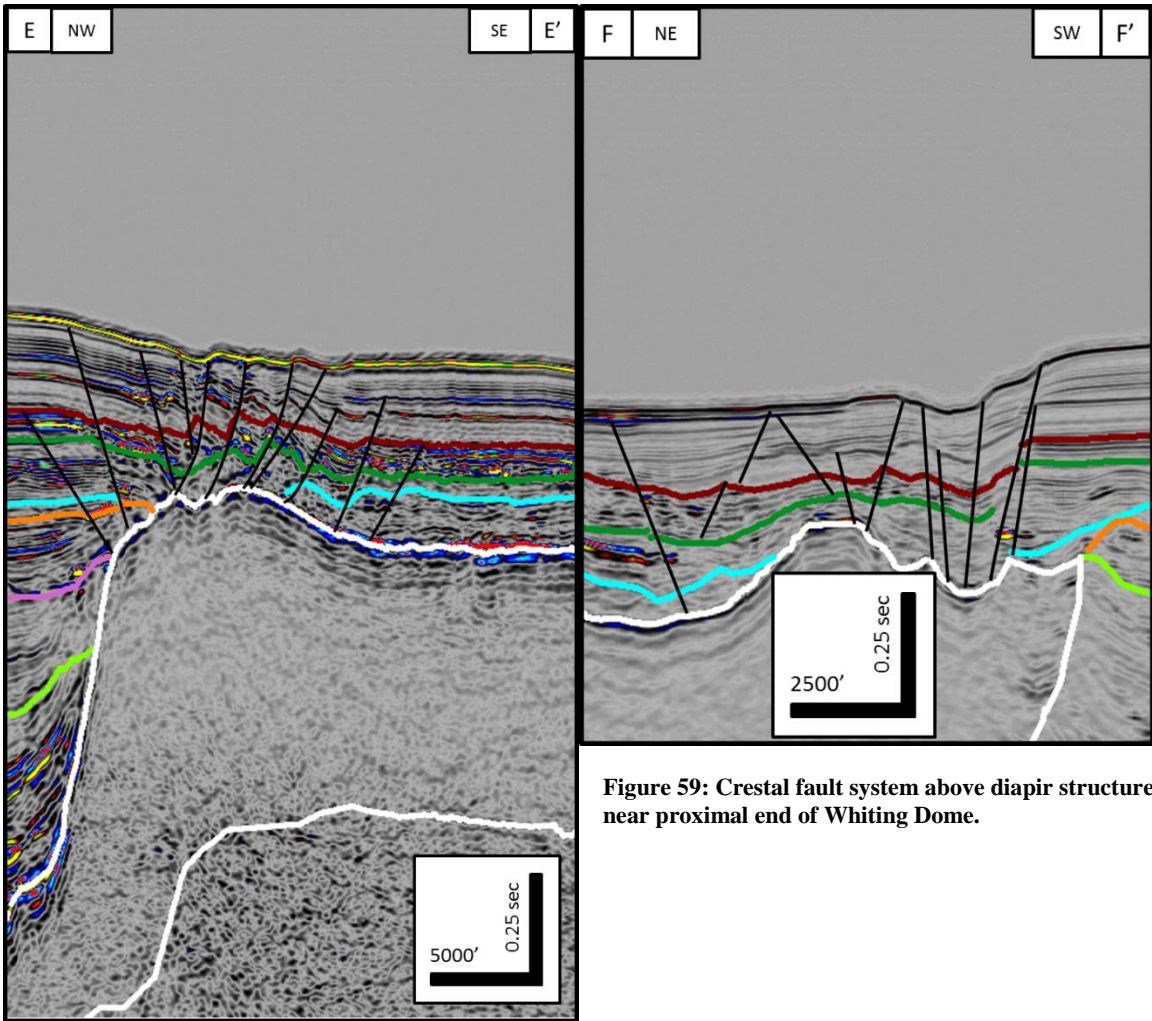


Figure 59: Crestal fault system above diapir structure near proximal end of Whiting Dome.

Holocene - HOL (Figure 60)

- Extremely high rates of deposition except directly above Whiting Dome
- Continued development of Pleistocene channel systems; apparent incising into currently forming distal end of Mississippi Delta Lobe
- Subsidence still occurring in withdrawal minibasin on outer eastern flank of Whiting Dome structure
- Crestal faulting around peaks and above mouth minibasin at proximal end of Whiting Dome. Most likely related to continued deflation of salt underlying minibasin mouth and inflation of salt rim.

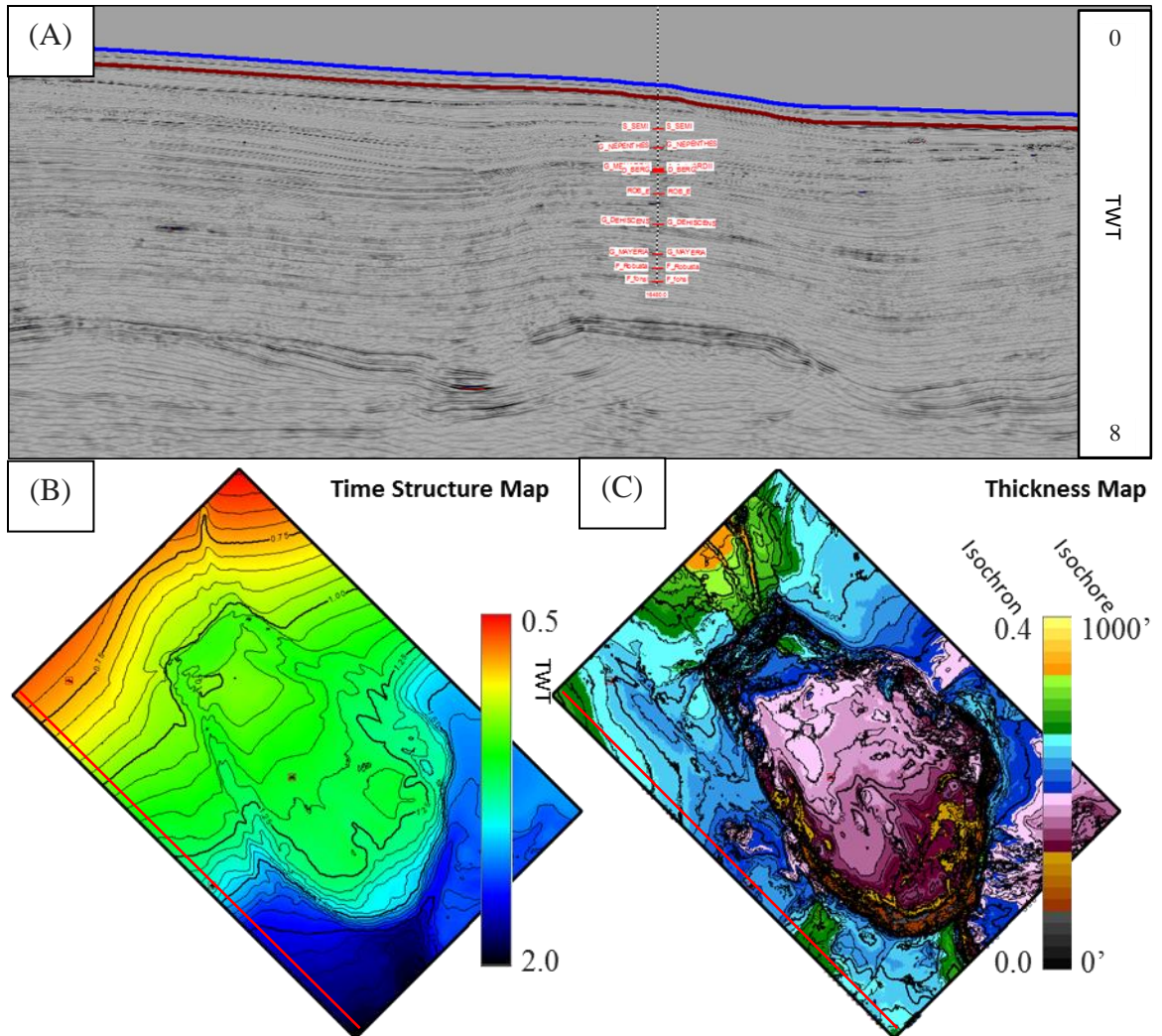


Figure 60: HOL horizon maps and picks. (A) 2D dip oriented seismic line showing the top (dark blue) and base (dark red) of the HOL horizon. Represents current seafloor bathymetry. (B) Time structure map for top HOL (C) Isochron and isochore map: constant velocity of 5000 ft/s used for time-depth conversion.

3.2 Conceptual Reconstruction

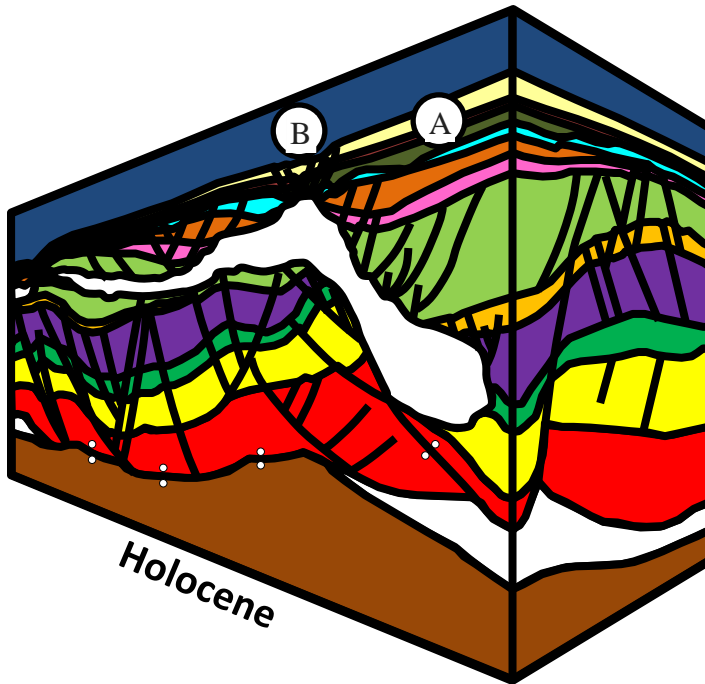


Figure 61: Current composition of Whiting Dome salt structure. Middle and late Pleistocene deposits primarily pelagic drape over salt structure, ponded deposits in extensional trough, with (A) incised channel/levee systems and turbidite flows outboard of salt. There are minimal tectonic features initiated during this time frame. These are mostly confined to (B) active extensional troughs above the rim of the salt structure.

Major events for future consideration include: continued loading of shelf deposits above the salt feeder will eventually lead to expulsion of the remaining salt within and large, channelized erosion around the flanks and distal end of the salt structure could weaken the lithology to the point that more significant sliding could occur. If further sliding does not occur, continued loading onto the top of the salt structure will eventually weld the minibasin floor with all remaining salt being evacuated into the salt walls on the flanks and the currently forming diapiric structures on the proximal end of the structure.

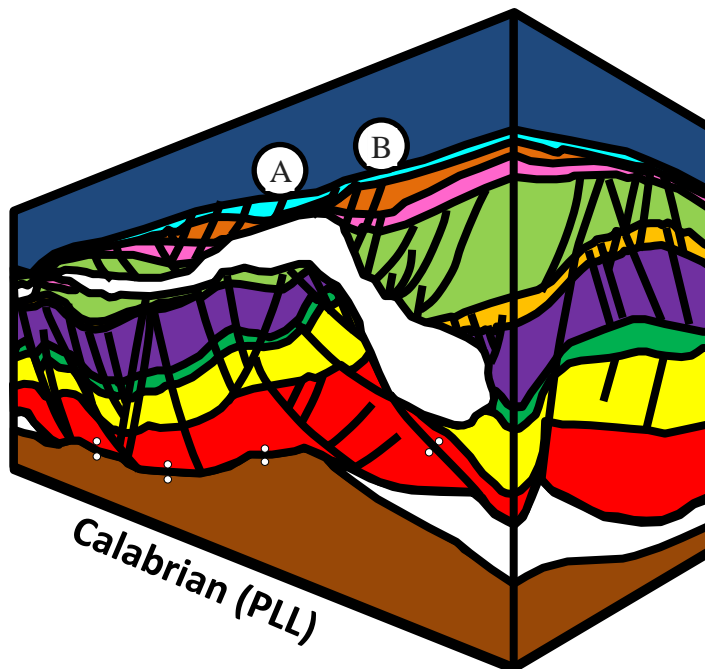


Figure 62: Salt structure at the end of the Calabrian (PLL) stage. This stage is defined by (A) significant truncation of top Pliocene strata and (B) slowing subsidence of the extensional trough above the main feeder. Significant slump scarring of PUU strata along the inner western flank of the minibasin signifies increased and abrupt inflation of the salt wall during the early PLL. Evidence for this can also be seen outboard of the salt where there is massive failure of PUU strata along the top of the PUL (Piacenzian) sequence boundary with detached blocks rotating away from the Whiting Dome. These tectonic events were probably aided by rapid lowering of sea level and associated decrease in hydrostatic pressure, thus lessening intrastatal strength of the uppermost deposits.

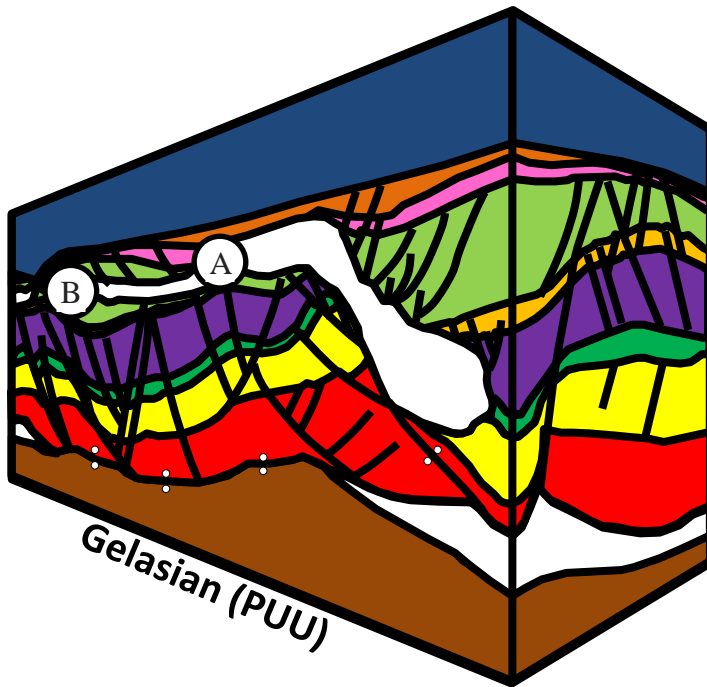


Figure 63: Salt structure at the end of the Gelasian (PUU) stage. (A) End of major salt gliding event. Stabilization of minibasin and beginning of salt wall inflation. (B) Little to no deposition on distal end of salt structure during PUU; what little deposition existed was heavily truncated during the Pleistocene. Deposition of PUU strata outboard of salt was dominated by prograding shelf margin – upper slope sediments.

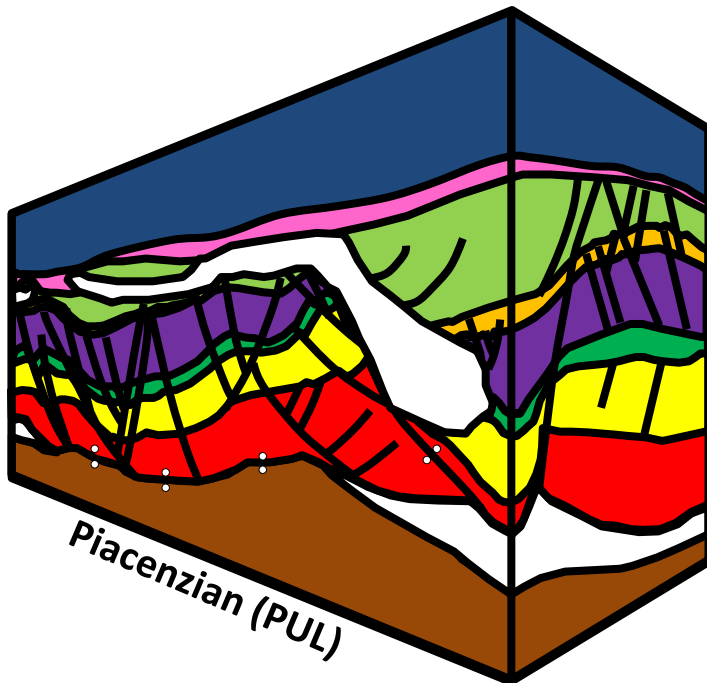


Figure 64: Salt structure at the end of the Piacenzian (PUL) stage. (A) This stage marks the youngest deposits beneath the distal end of the Whiting Dome salt structure. That small area of PUL deposition was heavily deformed by the conjunction of late inflation of the Mitchell Dome and the basinward gliding of the Whiting Dome minibasin. (B) Suprasalt PUL deposits are far less deformed due to less intra-minibasin compactional tectonics. By the end of the Piacenzian, the majority of minibasin movement due to salt gliding had been completed.

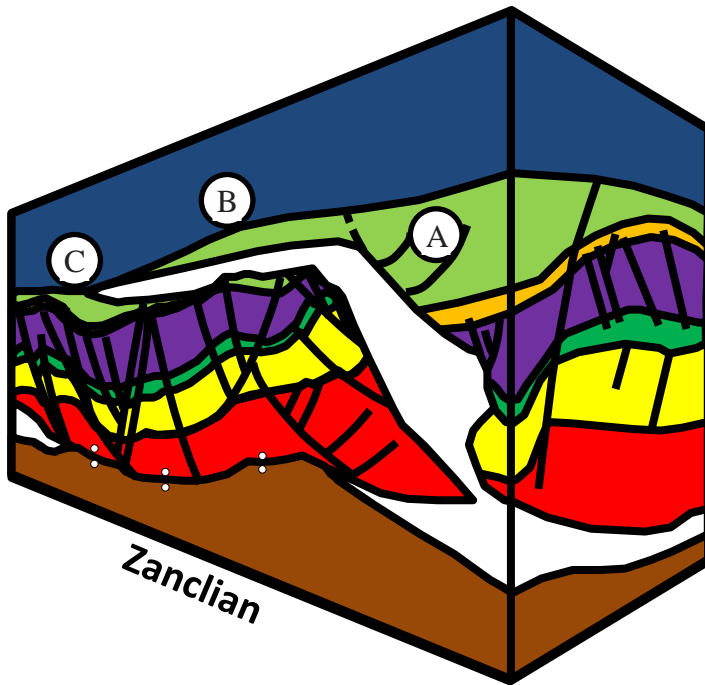


Figure 66: Salt structure at the end of the Zancian (PL) stage. There are four major phases of deposition and tectonics during the PL: pre-extrusion, syn-extrusion, pre-gliding, and syn-gliding. Early PL deposits continue infilling of salt evacuation basin as last vestiges of allochthonous salt move toward ridges and salt feeders and weld out (pre-extrusion). Continuous heavy deposition causes salt diapir piercement at shelf margin and produces a salt glacier/flooding of remnant evacuation basin. (A) Evacuating salt feeder creates copious accommodation space above feeder (syn-extrusion) and blocks. This sequence is aided by continuing evacuation of up-dip allochthonous salt, whereby (B) older outboard strata continue to detach and migrate shoreward. (C) Older subsalt strata is heavily faulted due to further settling and welding process and simultaneous effects of salt glacier movement. Diminishing salt flow allows PL sediments to crest salt tongue and begin depositing on top of structure (pre-gliding). Steady, but slowing, late PL deposition begins proximal extension and detachment phase (syn-gliding) and eventual collision and contractual deformation of proximal Mitchell Dome salt and sediments. This collision split the Whiting Dome minibasin into two roughly equivalent sub-minibasins, with the western half showing much more folding and apparent minor rotation around the western half of the Mitchell Dome.

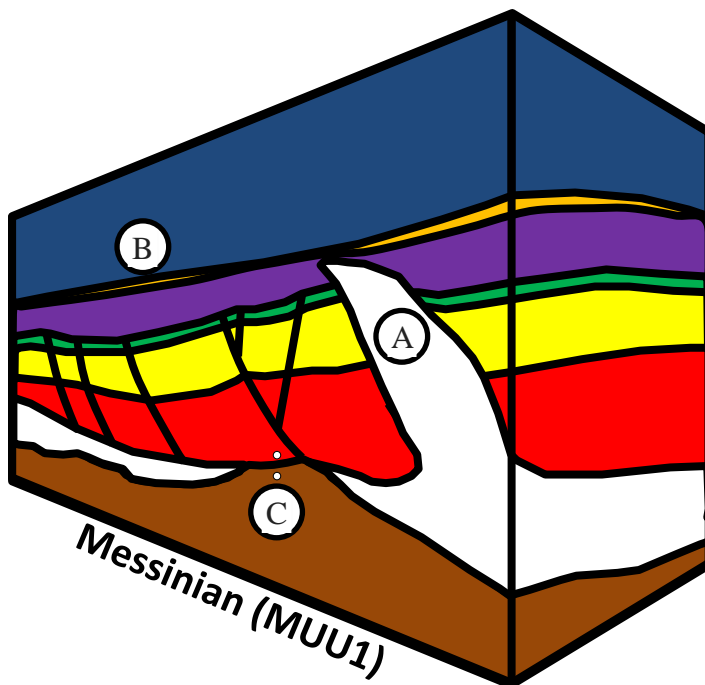


Figure 65: Salt structure at the end of the Miocene (MUU1). (A) Large, shelf-loaded diapir near piercement phase restricts down-dip access to already thin Messinian deposits. Sub-Whiting Dome Upper Tortonian (MUU2) and Messinian (MUU1) sediments are deposited into (B) an evacuation basin controlled by welding autochthonous salt. This marks the rising dominance of the Eastern Mississippi depositional axis. Strata in this chronozone are mostly slope apron and fan sediments. Continuing progradation of the shelf margin further evacuates autochthonous salt and most likely results in the (C) first salt welds in the study area.

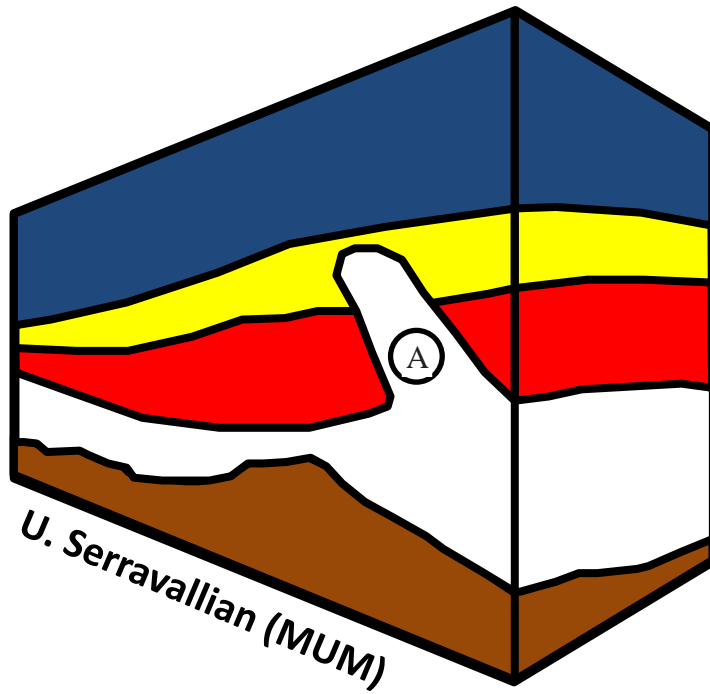


Figure 67: Salt structure at the end of the Upper Serravallian (MUM) stage. Study area primarily dominated by basinal deposits from the Cretaceous to Middle Miocene. The Upper Serravallian (MUM) marks the initial phase of the McAVLU fan, the thin flanks of which more than likely occupy the majority of the study area. (A) Earliest vertical salt structure forms along counter regional fault system.

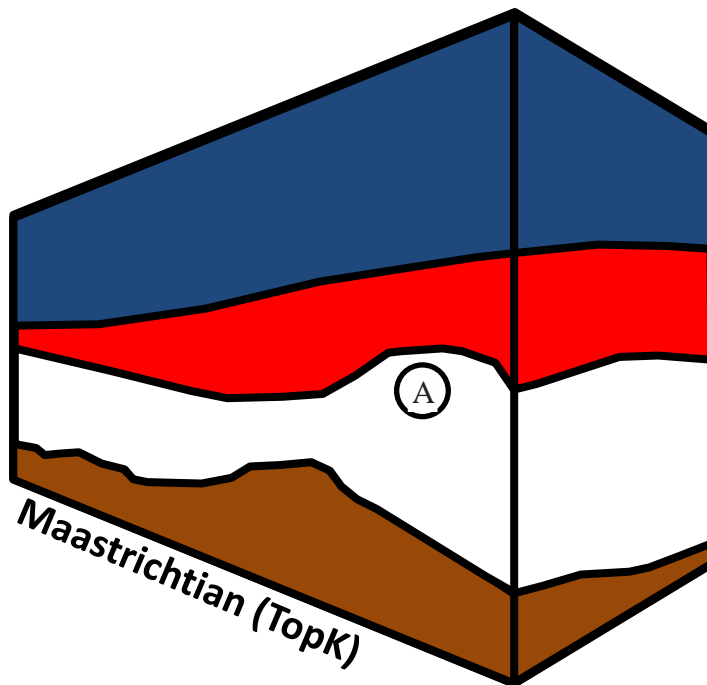


Figure 68: Salt structure at the end of the Maastrichtian (TopK) stage. Progradation of late Jurassic and early Cretaceous shelf-slope sediments and aggradation of basinal sediments begins forming (A) ridge structures in autochthonous salt. By the end of the Cretaceous, the ridge system in the study area had been set. This is highly evident in seismic when viewing pre- and post-Cretaceous unconformity strata. Pre-unconformity strata has significant onlap rollover, whereas late Cretaceous and post-Cretaceous strata is fairly conformable.

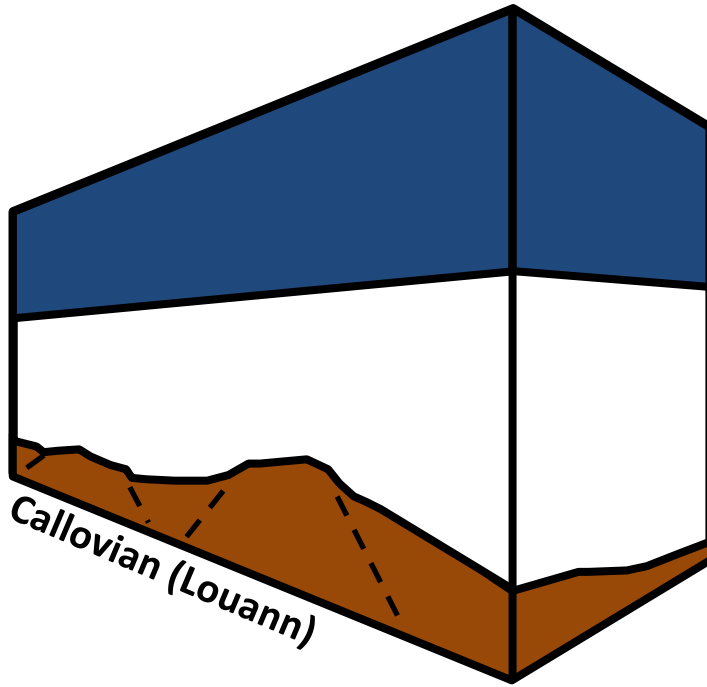


Figure 69: Salt structure at the end of the Callovian (Louann) stage. The world is salt and salt is the world. Louann Salt deposition fills basement lows and forms extremely thick salt layer across the Gulf of Mexico basin. Basement appears to be extensional graben and half graben system caused by rifting and attenuation phases.

3.3 Discussion and Conclusions

The Whiting Dome is an extremely complex structure by any measure. It has elements of compressional, tensional, and transtensional events that are further compounded by erosional events, subvertically rotated blocks, and subsalt imaging issues. This complexity has led to significant uncertainty during interpretation of many areas within the interior of the minibasin portion of the study area. However, the interpretation of broad, sequence-based events given in this study is logical, rational, and fully supported geologically, geophysically, and seismically.

Even in a visual examination of the time seismic data, the post-salt stratigraphic column in the study area is dominated by Miocene- and Pliocene-aged deposits and a not insignificant amount of Pleistocene and Holocene deposition. This is squarely in line with Galloway et al.'s (2000) synthesis of Cenozoic depositional history in the region. The predominance during these chronozones is primarily due to a shift in depositional axes away from the Red River to the Central and Eastern Mississippi delta systems during the middle and upper Miocene. This influence of the Eastern Mississippi depositional axis is evident in the large, relatively continuous stratigraphic packages in the study area. Study-area wide truncations in post-MUM strata are relatively limited, especially outboard of the major salt structures. There are two major exceptions to this statement. The top of the upper Pliocene and the top of the Lower Pleistocene both show extensive erosional features, especially above the Whiting Dome. The events in both chronozones are more than likely related to a combination of high frequency sea-level

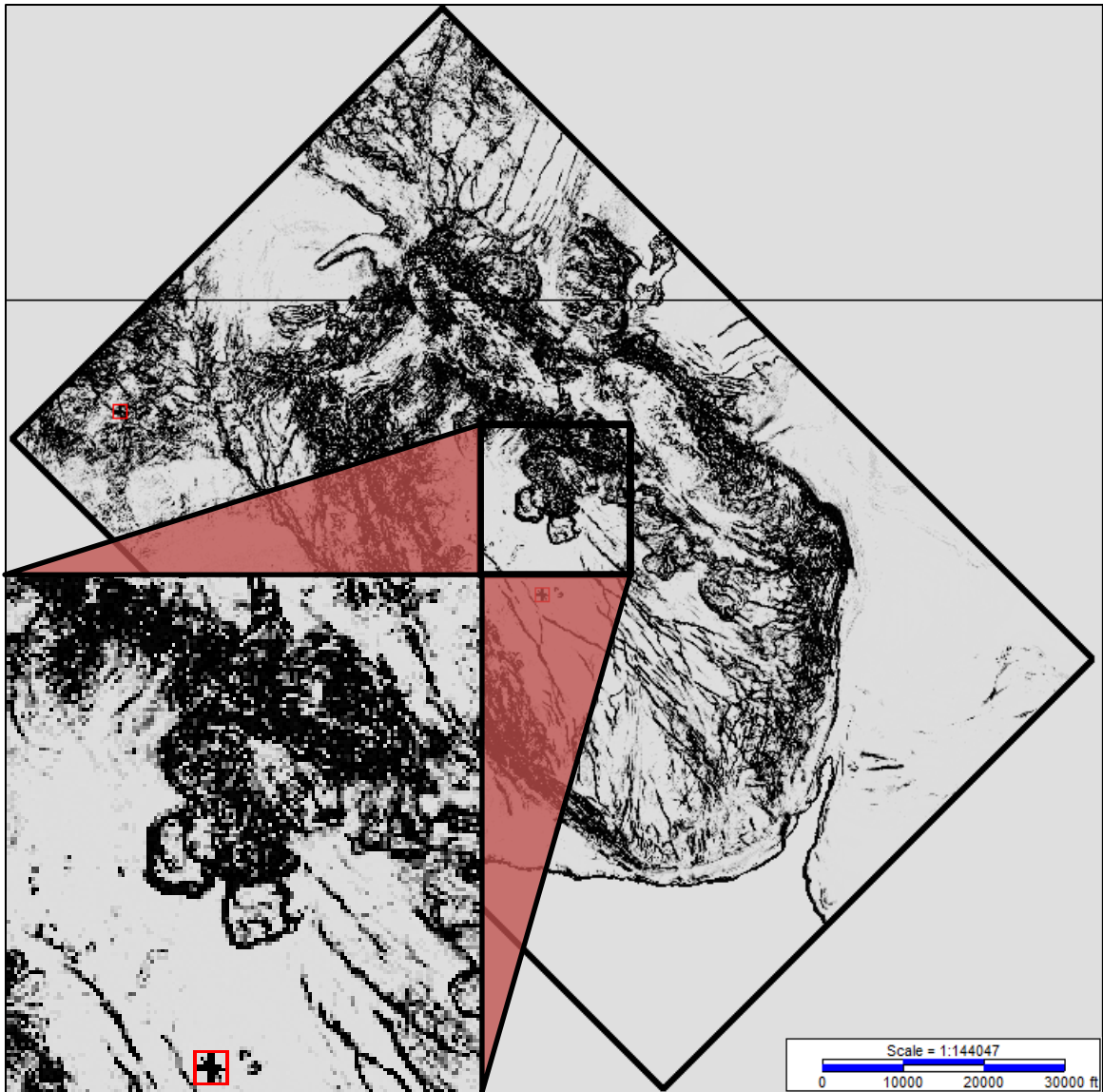


Figure 70: Time slice of Fault Attribute data generated from 3D PSTM reflection seismic block. Clover-leaf collapse structure at top of PUU highlighted.

cyclicality caused by the geologically rapid periods of Pleistocene glaciation and rapid inflation of the eastern salt wall along a major strike-slip fault. The associated lowering of hydrostatic pressure during these periods resulted in a significant decrease of intrastratal strength and helped induce collapse structures in large numbers in upper

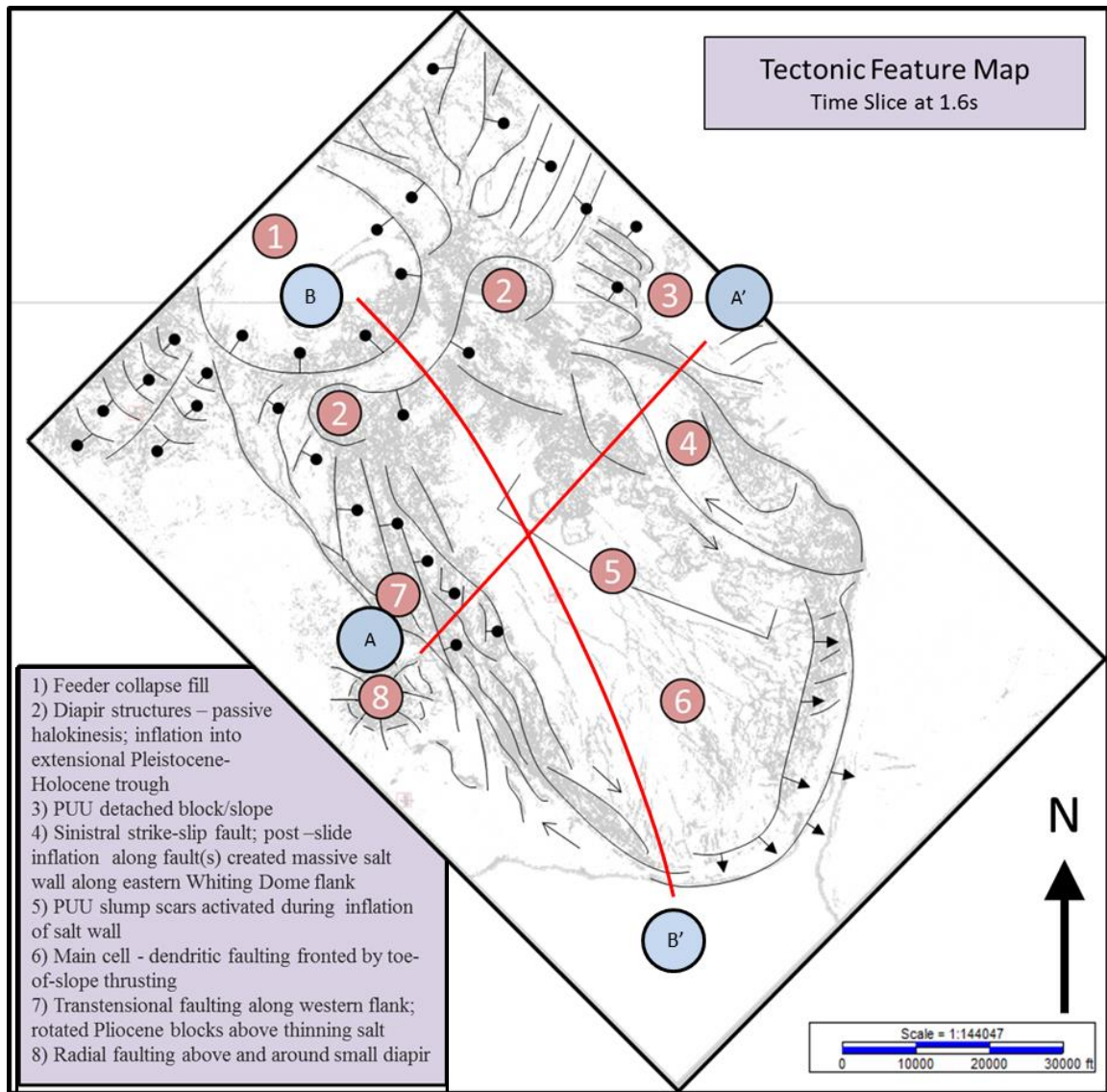


Figure 71: Structural interpretation of time slice using Fault Attribute data (edge detection cube).

Pliocene deposits. Circular and arcuate collapse structures are located within the Whiting Dome minibasin along the eastern salt wall and rotated block collapse structures are located on the northeastern flank of the eastern salt wall. A particularly unique four-leaf clover shaped collapse structure can be seen in Figure 70.

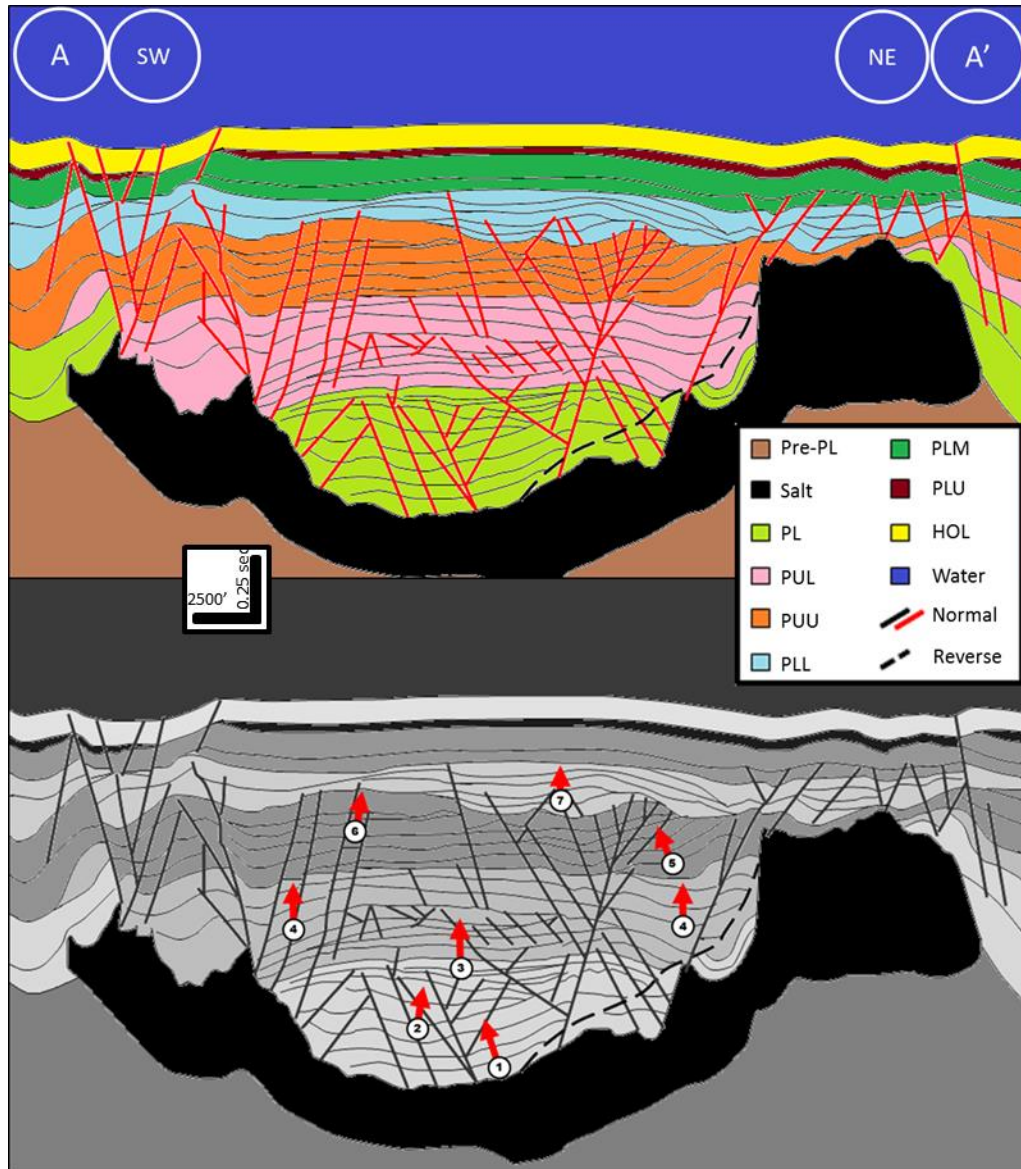


Figure 72: Strike oriented stratigraphic interpretation (top) and interpretation of depocenter shifts (bottom) of supra salt strata near the center of the Whiting Dome minibasin. There are seven discernable depocenter shifts from the Lower Pliocene to the Lower Pleistocene (minibasin subsidence ends at the beginning of the Middle Pleistocene): (1) Depocenter near middle of minibasin - density driven subsidence; (2) Unequal inflation of salt walls and associated shortening creates non-centered depocenter on western half of minibasin; (3) Balanced expulsion of salt returns depocenter to near-center position; (4) Inflation of salt walls exceeds rate of deposition and subsidence – Lower Pliocene strata inverted and dual depocenters form on minibasin flanks; (5-6) Unbalanced inflation of each salt wall shifts depocenter from side to side; (7) Balanced, slowing expulsion of base salt returns depocenter to near-center position

Structurally, Peel et al.'s (1995) basic interpretation of the Whiting Dome (Chapter 1.4, Figure 3) has been confirmed during this study. A more detailed interpretation of the general structure and synthesis of seismic interpretations of the Whiting Dome complex (Figure 71) and an interpretation and summary of the salt mobilization phases through analysis of depocenter shift within the salt of the Whiting Dome minibasin (Figure 72) are offered here.

Complex mobilization of the underlying salt structure lead to multiple series of deposition within the Pliocene (Figure 73) and formation of several interesting internal structures in the minibasin province. The salt tectonic and depositional phases of the Whiting Dome structure have been divided into 5 separate periods (Figure 74).

From the data and figures presented in this study, it can be reasonably concluded that mobilization and present day distribution of salt in the study area can be attributed to a repeating sequence: differential loading of sediments forces adjustment of underlying salt; salt deforms, creating new accommodation space; new sediment infills accommodation space further deforming salt. This sequence has been in effect since the Louann Salt finished depositing and the first sediments began loading onto it and has continued, with varying results, into modern times.

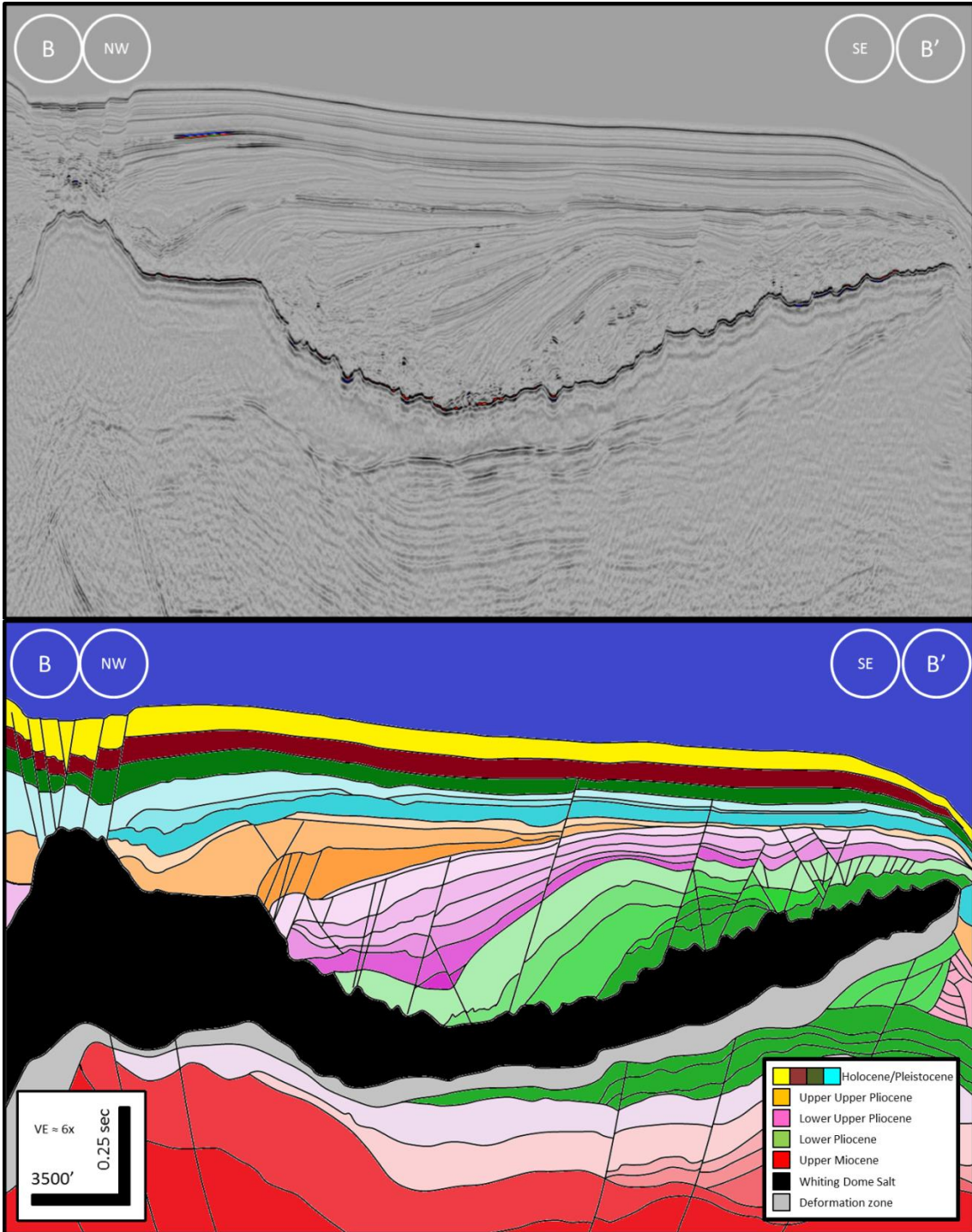


Figure 73: Uninterpreted (top) and interpreted (bottom) dip line from proximal end of salt structure through western sub-basin in minibasin portion of Whiting Dome.

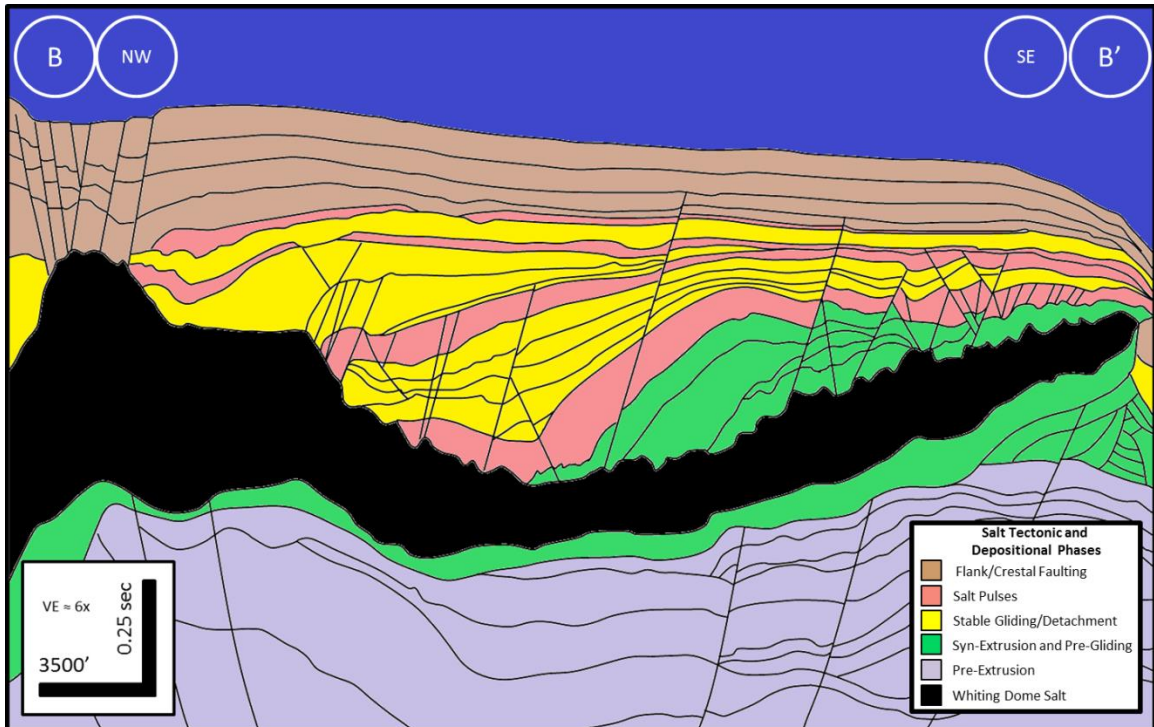


Figure 74: Salt tectonic and depositional phases of western sub-basin of minibasin portion of Whiting Dome salt structure. Syn-extrusion strata is highly inverted in the suprasalt section with some thrust/fold structures in the distal subsalt strata. Syn-gliding strata is dominated by infill above the salt detachment zone but is interrupted by large salt expulsion pulses. These pulses cause significant faulting akin to slope failure mechanisms within very narrow windows of time. The uppermost strata in the minibasin is structurally quiescent; the only significant deformation during this time is due to crestal faulting and extension above the rim of the salt structure.

3.3.1 Future Recommendations

As with any large dataset, there is a great deal more work that can be done. In terms of technological advancement, this dataset can be greatly enhanced using the most current imaging methods to better identify subsalt structures and timing events. While noted briefly throughout this study, a more in depth analysis of the geomorphology and the influence of halokinesis on its development would be extremely intriguing and a massive undertaking in its own right. Each major sequence would need to be assessed in as much, if not more, detail than this study presented for the general area. This dataset

also has a depth migrated (PSDM) version that could be evaluated using the interpretation of the higher amplitudes available in this time (PSTM) version.

Other possible avenues of research include incorporation of sidewall cores and other data available through the BSEE to the seismic data in order to more fully interpret sedimentation in the evacuation trough above the main Whiting Dome feeder. Similar areas of interest include the lobate structures seen in the top Pliocene – base Pleistocene section in the southern quadrant of the study area.

While this study provides a framework for stratigraphy in the area, much more detailed mapping of the Upper Miocene, Pliocene, and Pleistocene could add significant amounts of information towards the development of the area.

REFERENCES

- Andrews-Hanna, J. C., 2009. Planetary science: A mega-landslide on Mars. *Nature Geoscience*, 248-249.
- Bose, S., & Mitra, S., 2014. Structural analysis of a salt-cored transfer zone in the South Timbalier Block 54, offshore Gulf of Mexico: Implications for restoration of salt-related extensional structures. *AAPG Bulletin*, 98(4), 825-849.
- Bouroullec, R., Weimer, P., & Serrano, O., 2004. Salt Tectonic History of the Northeastern Deep Gulf of Mexico. *Gulf Coast Association of Geological Societies Transactions*, 54, 63-79.
- Broussard, R., & Sarwar, A. K., 2014. A Palinspastic Restoration for the Evolution of the Green Knoll Salt Dome in the Gulf of Mexico. *GCAGS Transactions*, 64, 59-79.
- Brun, J.-P., & Fort, X., 2011. Salt tectonics at passive margins: Geology versus models. *Marine and Petroleum Geology*, 28, 1123-1145.
- Buffler, R. T., 1991. Seismic stratigraphy of the deep Gulf of Mexico basin and adjacent margins. In A. Salvador (Ed.), *The Gulf of Mexico Basin* (Vol. J, pp. 353-387). Boulder: Geological Society of North America.
- Diegel, F. A., Schuster, D. C., Karlo, J. F., Shoup, R. C., & Tauvers, P. R., 1995. Cenozoic Structural Evolution and Tectono-Stratigraphic Framework of the

- Northern Gulf Coast Continental Margin. In M. P. Jackson, D. G. Roberts, & S. Snelson, *Salt tectonics: a global perspective: AAPG Memoir 65* (pp. 109-151).
- Duval, B., Cramez, C., & Jackson, M. P., 1992. Raft tectonics in the Kwanza Basin, Angola. *Marine and Petroleum Geology*, 9, 389-404.
- Feng, J., 1995. Post Mid-Cretaceous seismic stratigraphy and depositional history, deep Gulf of Mexico. *PhD Dissertation*. University of Texas.
- Fletcher, R. C., Hudec, M. R., & Watson, I. A., 1995. Salt Glacier and Composite Sediment-Salt Glacier Models for the Emplacement and Early Burial of Allochthonous Salt Sheets. In M. P. Jackson, D. G. Roberts, & S. Snelson, *Salt tectonics: a global perspective: AAPG Memoir 65* (pp. 77-108).
- Galloway, W. E., Ganey-Curry, P. E., Li, X., & Buffler, R. T., 2000. Cenozoic depositional history of the Gulf of Mexico basin. *AAPG Bulletin*, 84(11), 1743-1774.
- Ge, H., Jackson, M. P., & Vendeville, B. C., 1997. Kinematics and dynamics of salt tectonics driven by progradation. *AAPG Bulletin*, 81(3), 398-423.
- Hudec, M. R., & Jackson, M. P., 2007. Terra infirma: Understanding salt tectonics. *Earth-Science Reviews*, 82, 1-28.
- Hudec, M. R., Jackson, M. P., & Peel, F. J., 2013. Influence of deep Louann structure on the evolution of the northern Gulf of Mexico. *AAPG Bulletin*, 97(10), 1711-1735.

- Hudec, M. R., Jackson, M. P., & Schultz-Ela, D. D., 2009. The paradox of minibasin subsidence into salt: Clues to the evolution of crustal basins. *GSA Bulletin*, 201-221.
- Hudec, M. R., Norton, I. O., Jackson, M. P., & Peel, F. J., 2013. Jurassic evolution of the Gulf of Mexico salt basin. *AAPG Bulletin*, 97(10), 1683-1710.
- Jackson, C. A., & Lewis, M. M., 2014. Structural style and evolution of a salt-influenced rift basin margin; the impact of variations in salt composition and the role of polyphase extension. *Basin Research*, 1-22.
- Karlo, J. F., & Shoup, R. C., 2000. Classifications of syndepositional Systems and Tectonic Provinces of the Northern Gulf of Mexico. *Search and Discovery*.
- Louisiana Geological Survey., 2000. *Folio Series No. 8: Stratigraphic Charts of Louisiana*. Louisiana State University.
- Mancini, E. A., & Puckett, T. M., 2002. Transgressive-regressive cycles in Lower Cretaceous strata, Mississippi Interior Salt Basin area of the northeastern Gulf of Mexico, USA. *Cretaceous Research*, 23, 409-438.
- Mayall, M. J., Yeilding, C. A., Oldroyd, J. D., Pulham, A. J., & Sakurai, S., 1992. Facies in a Shelf-Edge Delta - An Example from the Subsurface of the Gulf of Mexico, Middle Pliocene, Mississippi Canyon, Block 109. *AAPG Bulletin*, 76(4), 435-448.
- Obid, J. A., 2006. Seismic Stratigraphy of the Jurassic Section in Mobile Area, Offshore. *The Gulf Coast Association of Geological Societies*, 608-620.

- Peel, F. J., Travis, C. J., & Hossack, J. R., 1995. Genetic structural provinces and salt tectonics of the Cenozoic offshore U.S. Gulf of Mexico: a preliminary analysis. In M. P. Jackson, D. G. Roberts, & S. Snelson, *Salt tectonics: a global perspective: AAPG Memoir 65* (pp. 153-175).
- Pilcher, R. S., Murphy, R. T., & Ciosek, J. M., 2014. Jurassic raft tectonics in the northeastern Gulf of Mexico. *Interpretation*, 39-55.
- Posamentier, H. W., 2004. Seismic Geomorphology: Imaging Elements of Depositional Systems from Shelf to Deep Basin Using 3D Seismic Data: Implications for Exploration and Development. *The Geological Society of London Memoirs*, 29, 11-24.
- Posamentier, H. W., & Kolla, V., 2003. Seismic Geomorphology and Stratigraphy of Depositional Elements in Deep-water Settings. *Journal of Sedimentary Research*, 73(3), 367-388.
- Prather, B. E., Booth, J. R., Steffens, G. S., & Craig, P. A., 1998. Classification, Lithologic Calibration, and Stratigraphic Succession of Seismic Facies of Intraslope Basins, Deep-Water Gulf of Mexico. *AAPG Bulletin*, 82(5A), 701-728.
- Quirk, D. G., & Pilcher, R. S., 2012. Flip-flop salt tectonics. *Geological Society, London, Special Publications*, 363, 245-264.
- Rowan, M. G., 1993. A systematic technique for the sequential restoration of salt structures. *Tectonophysics*, 331-348.

- Rowan, M. G., 2014. Passive-margin salt basins: hyperextension, evaporite deposition, and salt tectonics. *Basin Research*, 26, 154-182.
- Rowan, M. G., Jackson, M. P., & Trudgill, B. D., 1999. Salt-related fault families and fault welds in the northern Gulf of Mexico. *AAPG Bulletin*, 83(9), 1454-1484.
- Salvador, A., 1991. Triassic-Jurassic. In *The Gulf of Mexico Basin* (Vol. J, pp. 131-180). Geological Society of America, The Geology of North America.
- Sawyer, D. E., Flemings, P. B., Shipp, R. C., & Winker, C. D., 2007. Seismic geomorphology, lithology, and evolution of the late Pleistocene Mars-Ursa turbidite region, Mississippi Canyon area, northern Gulf of Mexico. *AAPG Bulletin*(2), 215-234.
- Todd, R. G., & Mitchum, Jr., R. M., 1977. Seismic stratigraphy and global changes of sea level, part 8: identification of Upper Triassic, Jurassic, and Lower Cretaceous seismic sequences in Gulf of Mexico and offshore West Africa. In C. E. Payton (Ed.), *AAPG Memoir 26: Seismic stratigraphy - applications to hydrocarbon exploration* (pp. 145-163).
- U.S. Energy Information Administration., 2015. *U.S. Crude Oil and Natural Gas Proved Reserves, 2014*. Washington, D.C.: U.S. Department of Energy.
- Warsitzka, M., Kley, J., & Kukowski, N., 2014. Analogue experiments of salt flow and pillow growth due basement faulting and differential loading. *Solid Earth Discussion*, 6, 1625-1686.

- Weimer, P., & Bouroullec, R., 2013. Petroleum Geology of the Mississippi Canyon, Atwater Valley, Western Desoto Canyon, and Western Lloyd Areas, Northern Deep Gulf of Mexico: Traps, Reservoirs, and Their Timing. In N. C. Rosen, P. Weimer, S. M. dos Anjos, S. Henrickson, E. Marques, M. Mayall, . . . F. Schroeder, *New Understanding of the Petroleum Systems of Continental Margins of the World: 32nd Annual* (Vol. 32, pp. 110-132).
- Wood, L. J., 2007. Quantitative Seismic Geomorphology of Pliocene and Miocene Fluvial Systems in the Northern Gulf of Mexico, U.S.A. *Journal of Sedimentary Research*, 77, 713-730.

Appendix A: Seismic Technical Data

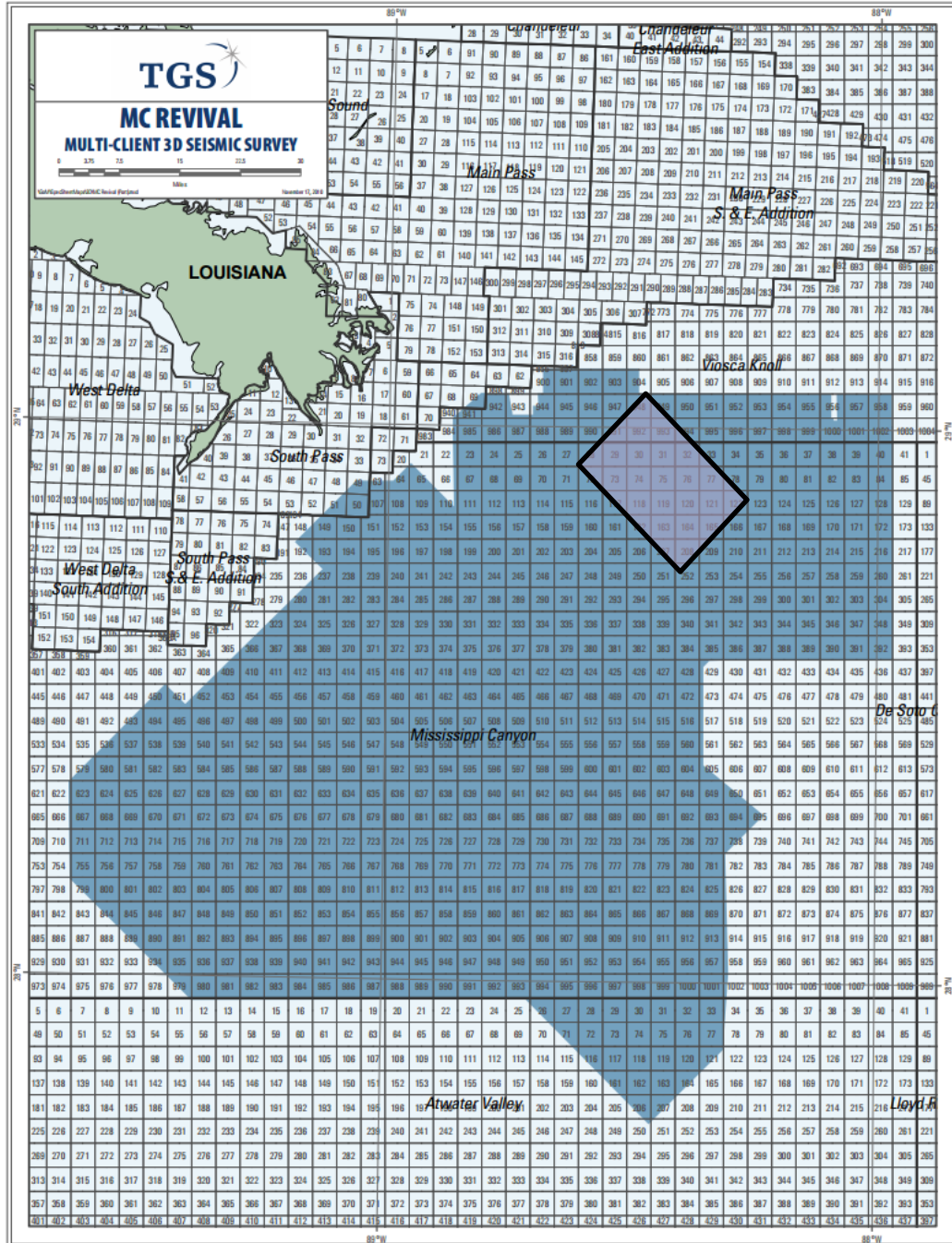


Figure 75: Full extent of MC Revival seismic survey by TGS with study area shown in purple rectangle.



MISSISSIPPI CANYON REVIVAL 3D MULT-CLIENT 3D SURVEY

PRE-STACK TIME ACQUISITION

	Mississippi Canyon 1	Mississippi Canyon 2	Mississippi Canyon 3	Mississippi Canyon 3-6
Acquisition Date:	3/8/99-10/27/99	10/23/99-07/06/00	10/23/99-07/06/00	1/7/99-4/28/00
Data Acquired by:	CGG	CGG	GECO (undershoot)	GECO
Shooting Orientation:	North/South	North/South	North/South	Northwest/Southeast
Recording Instrument:	Syntron 480	Syntron 480	Triacq	Triacq
Streamer Type:	Syntron	Syntron	Nessie 3 & 4	Nessie 3 & 4
Source/Streamer Positioning:	GPS/DGPS	GPS/DGPS	GPS/DGPS	GPS/DGPS
Airgun Source:	4180 cubic inches	4180 cubic inches	5400 cubic inches	5400 cubic inches
Gun Depth:	7.5 meters +/- 1 meter	7.5 meters +/- 1 meter	6 meters +/- 1 meter	6 meters +/- 1 meter
Shotpoint Interval:	75 meters per CMP line	62.5 meters per CMP line	62.5 meters per CMP line	62.5 meters per CMP line
CMP Crossline Separation:	45 meters	40 meters	40 meters	40 meters
Group Interval:	25 meters	25 meters	25 meters	25 meters
Recording Channels:	288/240 per streamer	288 per streamer	320 per streamer	320 per streamer
Streamer Depth:	9 meters +/- 1.5 meters	9 meters +/- 1.5 meters	9 meters +/- 1.5 meters	9 meters +/- 1.5 meters
Streamer Length:	4 x 7200 meters/ 4 X 6000 meters	7200 meters	8000 meters	8000 meters
Record Length:	12.288 seconds	12.288 seconds	12.288 seconds	12.288 seconds
Sample Interval:	4 milliseconds	2 milliseconds	2 milliseconds	2 milliseconds
Nominal Fold:	57.6	57.6	64	64

Figure 76: Acquisition specifications for MC Revival seismic survey



MISSISSIPPI CANYON REVIVAL 3D MULT-CLIENT 3D SURVEY

PRE STACK TIME PROCESSING SEQUENCE

- Processing provided by: TGS Imaging-Houston
- Processing completed November 2004
- Input navigation merge shot ordered tapes
 - SEG Y – 4ms sample rate
- Debubble
- Noise attenuation
- Output shot ordered tapes - SEG Y
- Surface related multiple elimination (SRME)
- Noise attenuation
- Velocity analysis
- Radon de-multiple
- Application of cold water statics
- 3D bin sort – 12.5m CDP interval, 58/64 fold
- Deterministic decon
- Spherical divergence and gain correction
- Output bin sorted tapes – SEG Y
- Grid data – 25m x 40m – diagonal grid
- Input migration velocities provided by TGS-NOPEC
- Kirchhoff pre stack curved ray migration – 25m x 40m
- Output 3D bin sorted tapes – 29/32 fold – SEG Y
- Velocity analysis
- Output velocity spectra tapes – SEG Y
- Automatic velocity picking update at every CDP location
- Output 3D velocity trace volume
 - SEG Y (12.5m by 20m by 4msec)
- Output ETA velocity correction trace volumes- SEG Y
 - (25m by 40m by 48msec and 12.5m by 20m by 4msec)
- Radon de-multiple
- Output migrated gathers with NMO/Radon
 - 29/32 fold – SEG Y
- Mute and stack
- Output raw migration – SEG Y – 25m x 40m
- Output 4 corridor stacks – SEG Y – 12.5m x 20m
- Apply filter and wrap scale
- Output processed migration – SEG Y – 12.5m x 20m

DELIVERABLES

- Raw field data/shot ordered (MC1 @ 4ms, MC2 – 6 @ 2ms)
- Field data with navigation in the trace headers / shot ordered
- MC1,2,3,5,6 – 4ms sample rate
- MC4 – 2ms sample rate and 4ms sample rate available
- Debubble data/ shot ordered
- SRME and Radon de-multiple CDP gathers - 12.5m x 40m/45m
- Areas MC1-6 will be delivered on the diagonal grid
- Areas MC1 and MC2 will also be available on the N/S grid
- Pre stack time migrated CDP gathers without NMO - 25m x 40m
- Pre stack time migrated CDP gathers with NMO/Radon - 25m x 40m
- Corridor stacks - 12.5m x 20m
- Raw migration – 25m x 40m
- Processed migration - 12.5m x 20m
- Migration velocities (ASCII)
- Stacking velocities (ASCII)
- 3D stacking velocity trace volume – SEG Y (12.5m by 20m every 4ms)
- ETA velocity correction - high order NMO correction - SEG Y
 - Volume 1- 25 by 40 meters every 48msec
 - Volume 2- 12.5 by 20 meters every 4msec
- Processed source-receiver navigation – UKOOA
- Workstation-ready tapes available in SMT, Landmark, and Geoquest

Figure 77: Processing sequence and deliverables for the MC Revival seismic survey

Appendix B: Depiside Maps from Galloway et al (2000)



Figure 78: Explanation of symbols for paleogeographic maps.

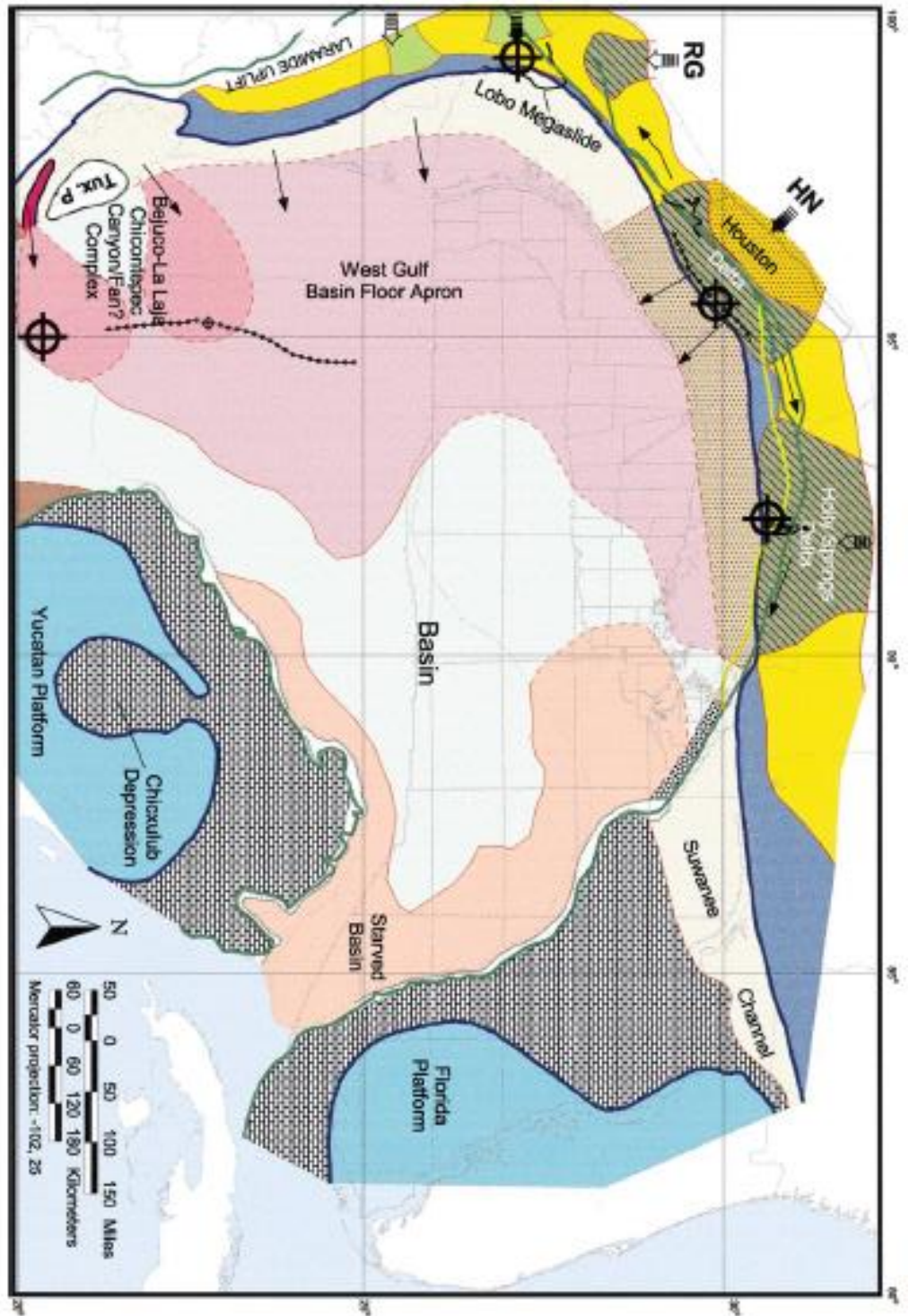


Figure 79: Paleogeography of the Lower Wilcox deposide (61-56.4 Ma)

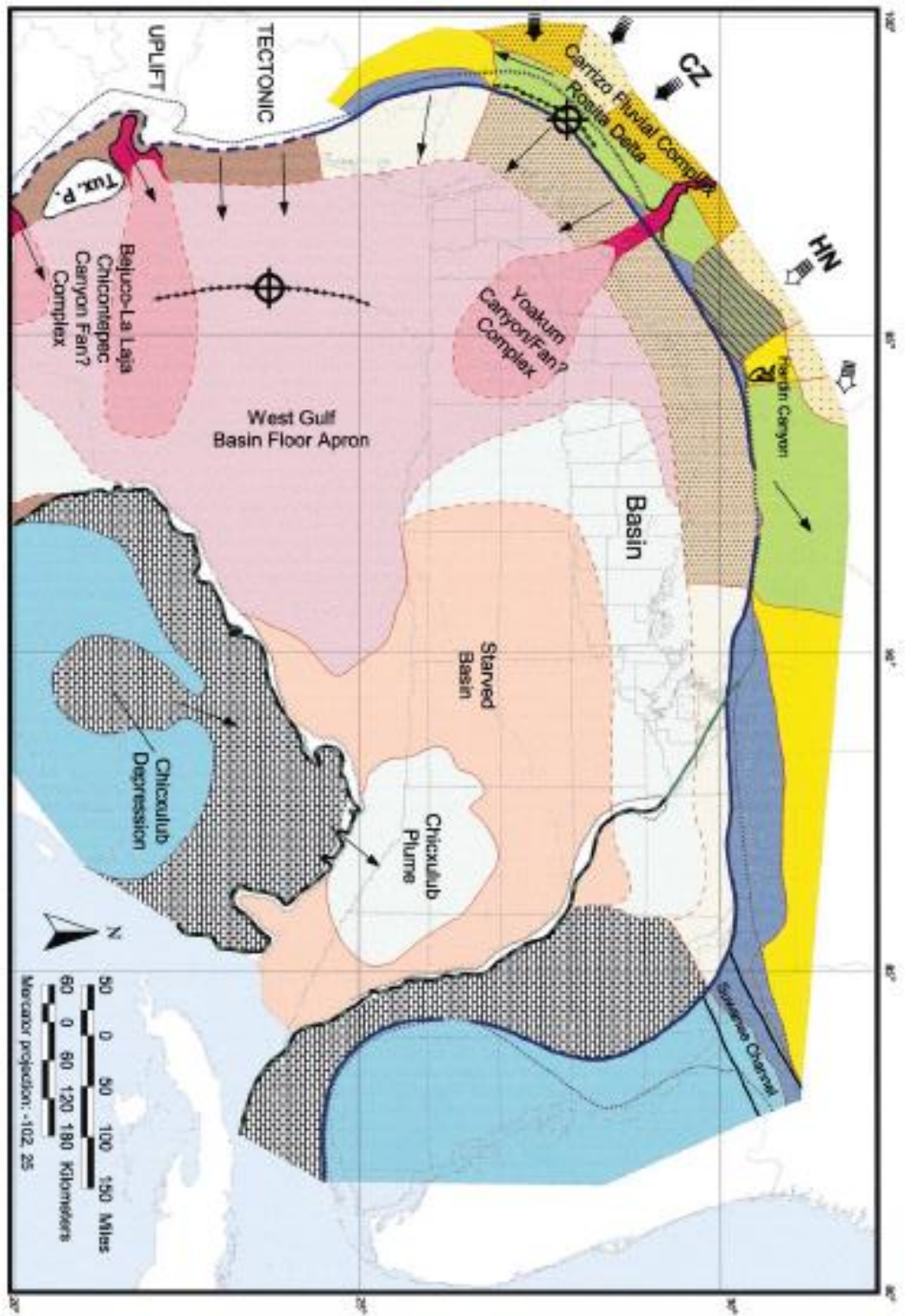


Figure 80: Paleogeography of the Upper Wilcox deposide (48.5-54.5 Ma)

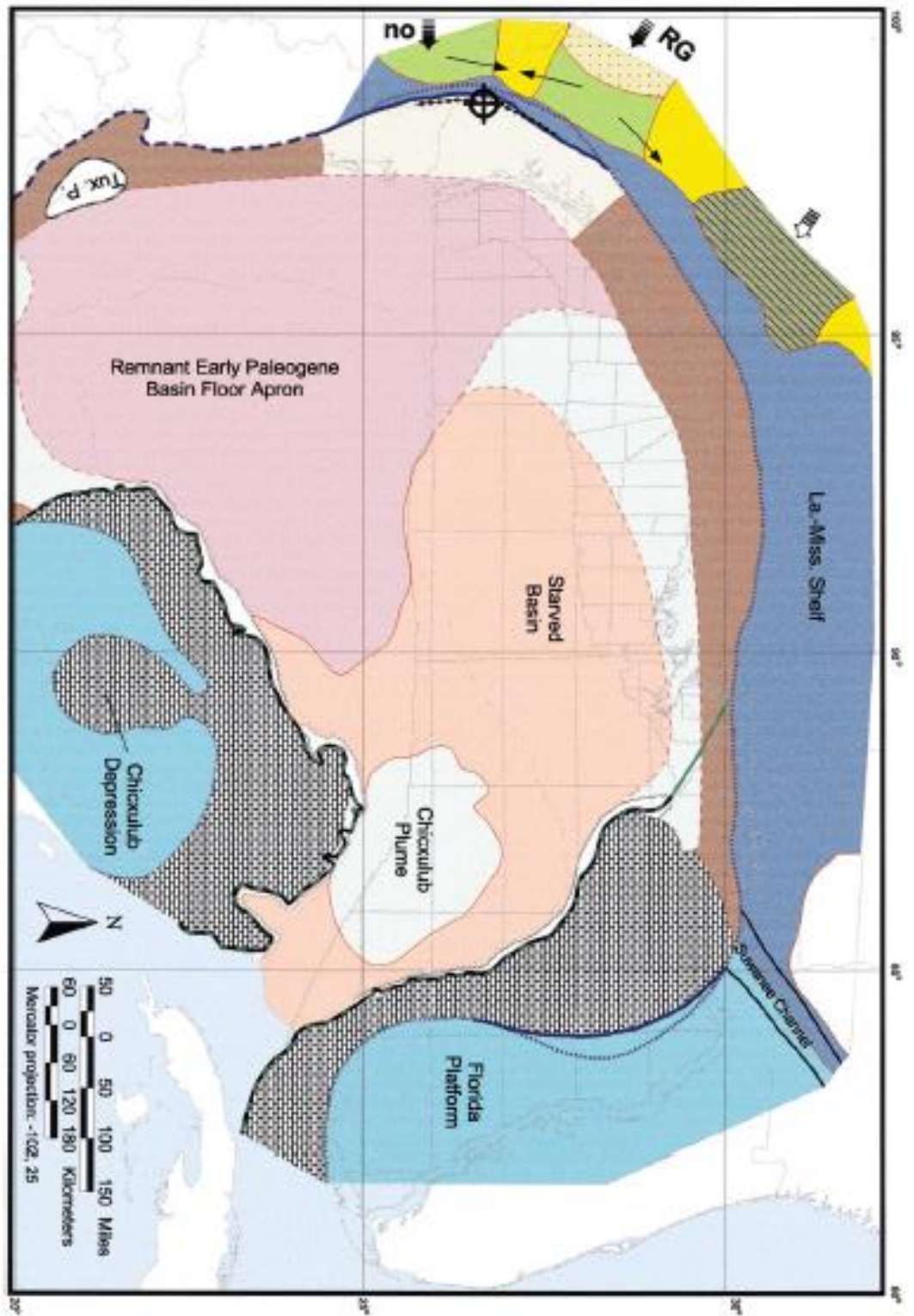


Figure 81: Paleogeography of the Queen City depiside (47.5-44.5 Ma)

Figure 82: Paleogeography of the Yegua/Cockfield deposide (38.5-35 Ma)

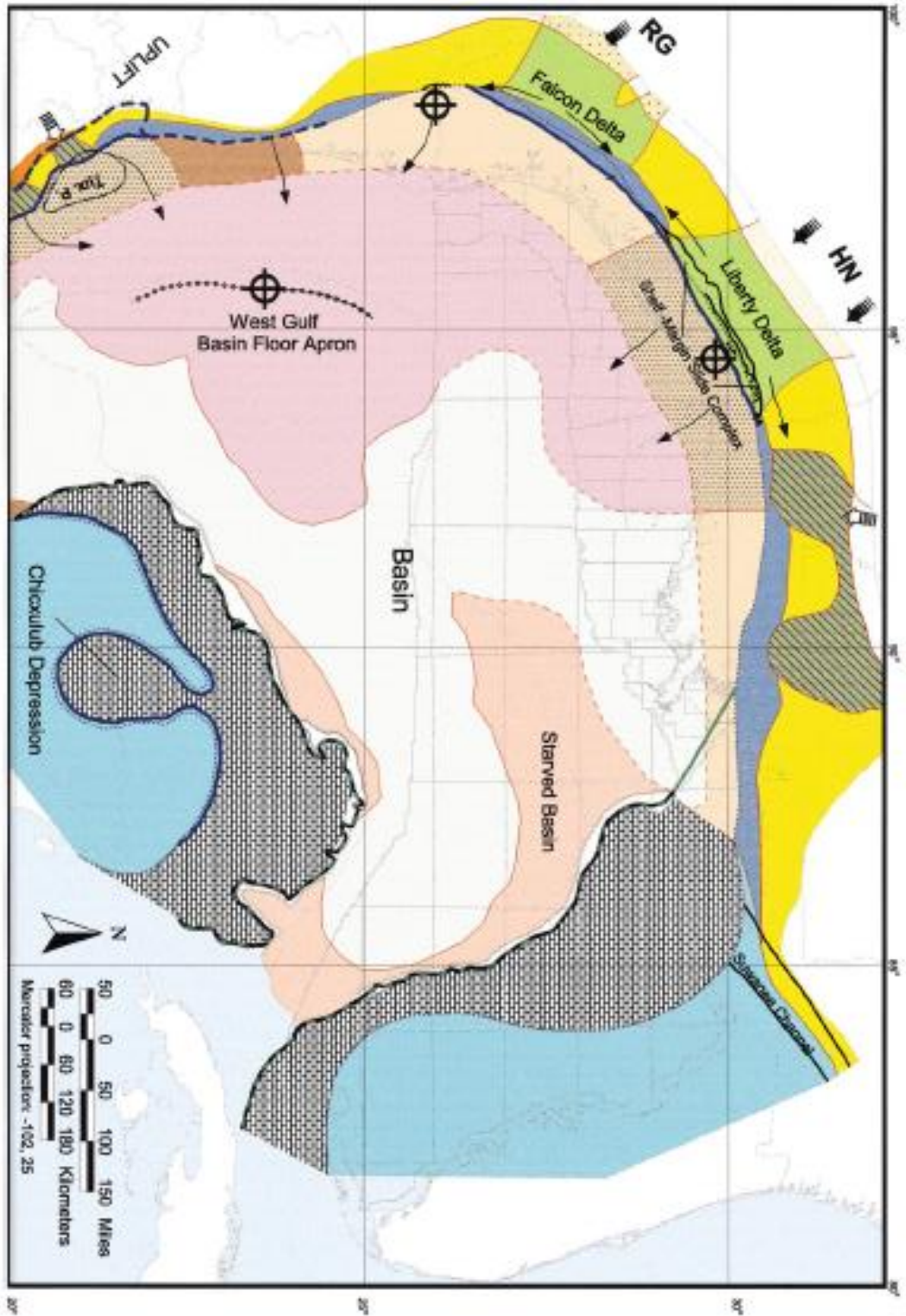
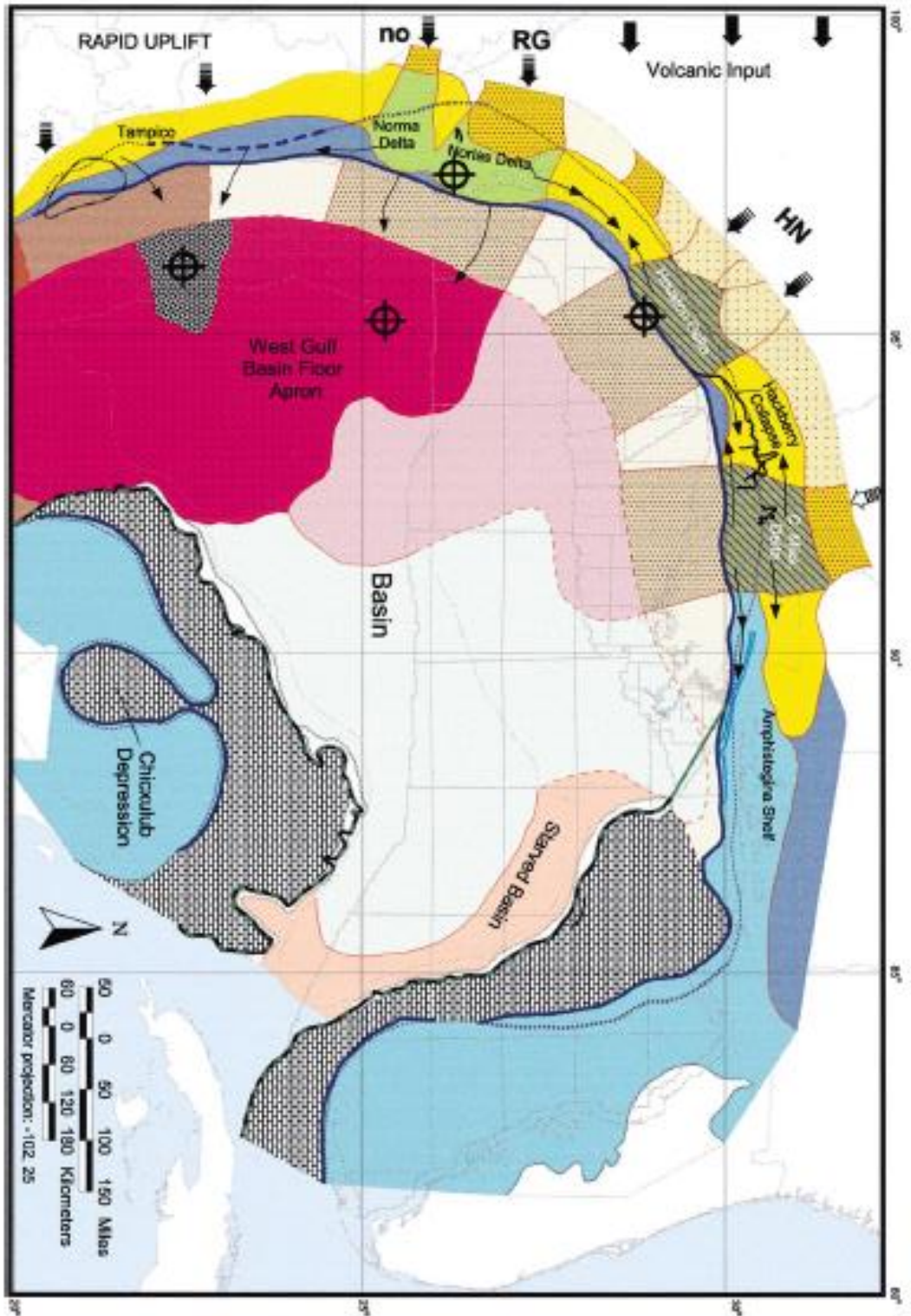


Figure 83: Paleogeography of the early Frío/Vicksburg deposide (32.6-28 Ma)



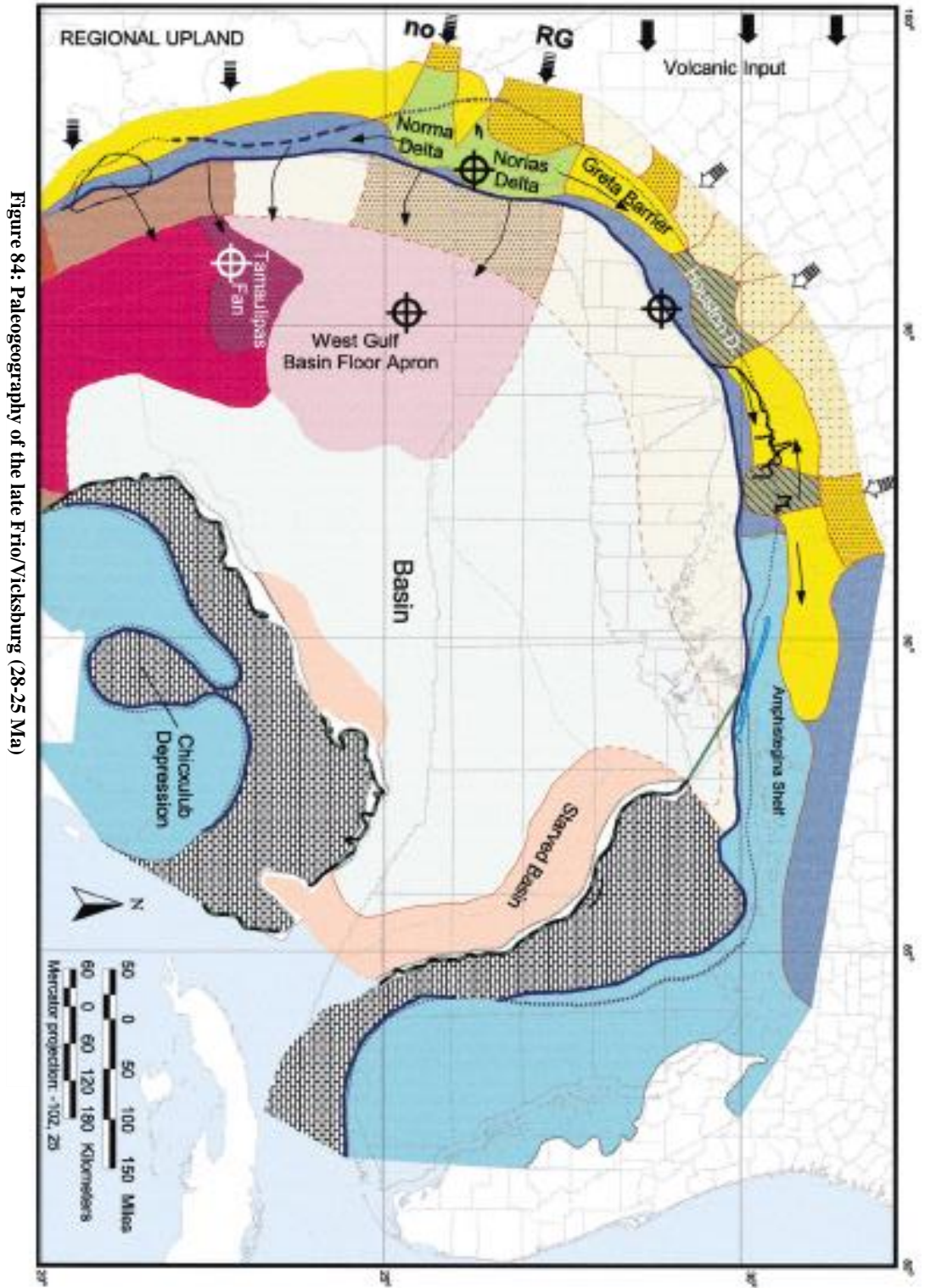


Figure 84: Paleogeography of the late Frio/Vicksburg (28-25 Ma)

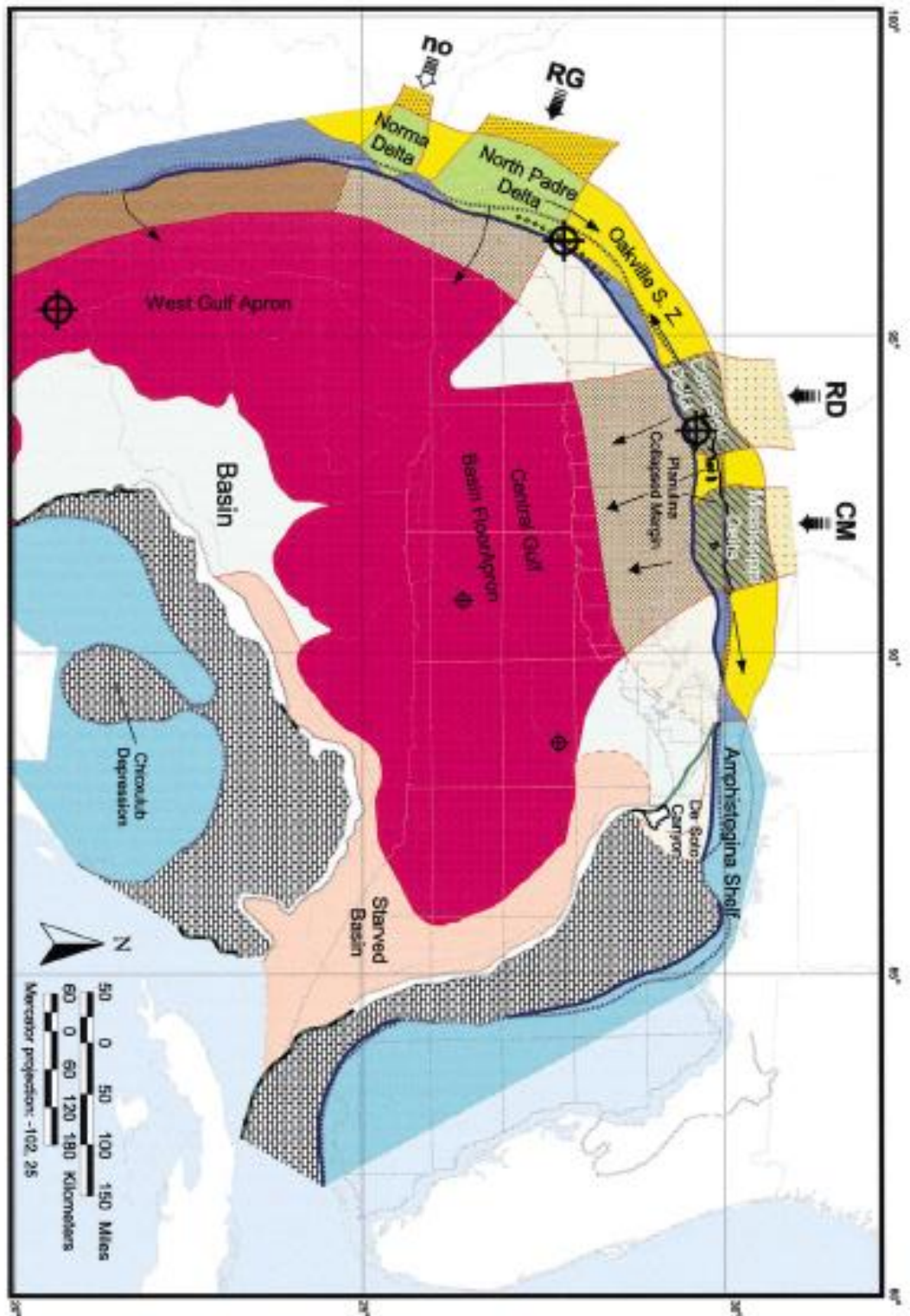


Figure 85: Paleogeography of the first early Miocene depositional period (25-18 Ma)

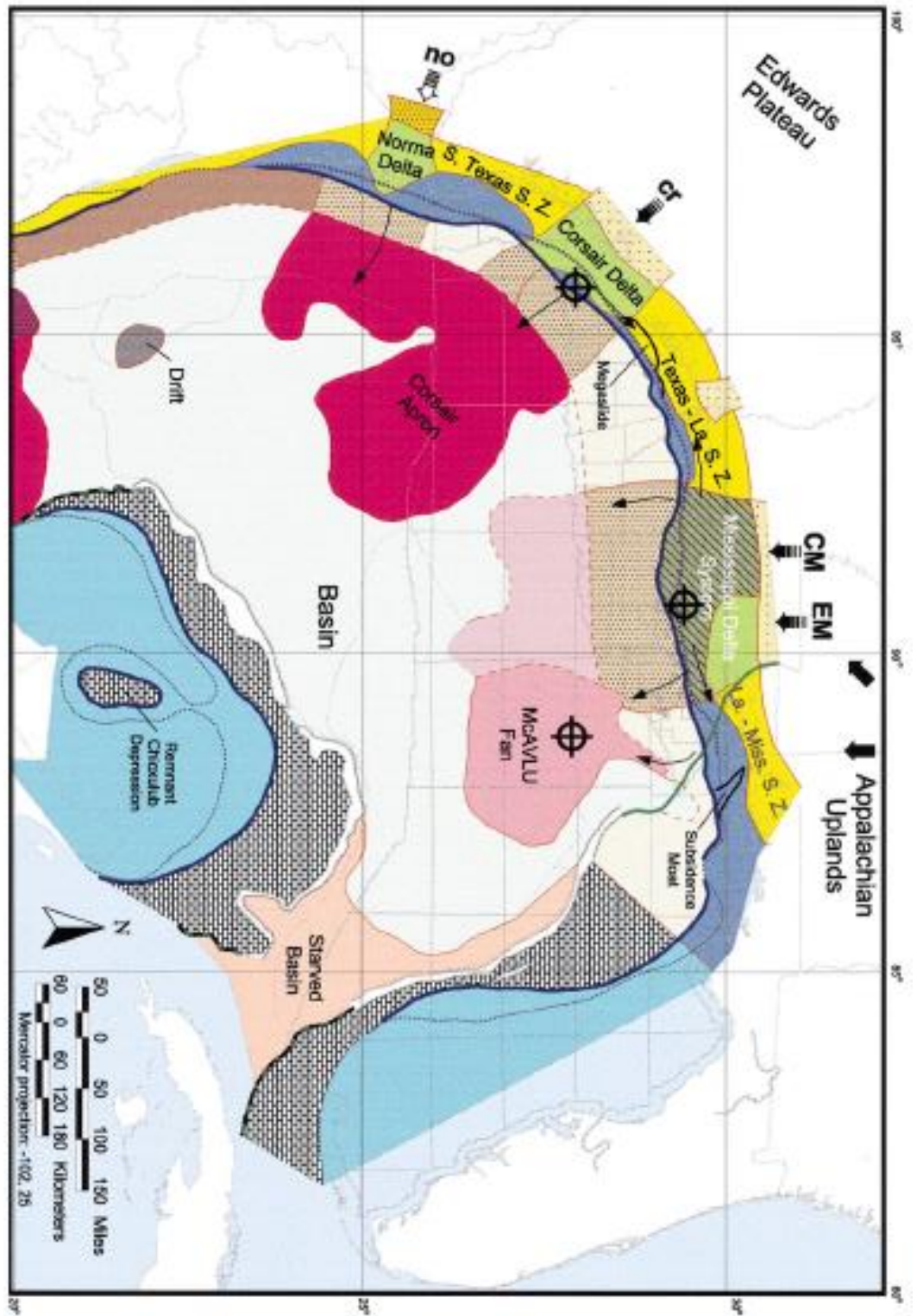


Figure 86: Paleogeography of the middle Miocene deposide (15.6-12 Ma)

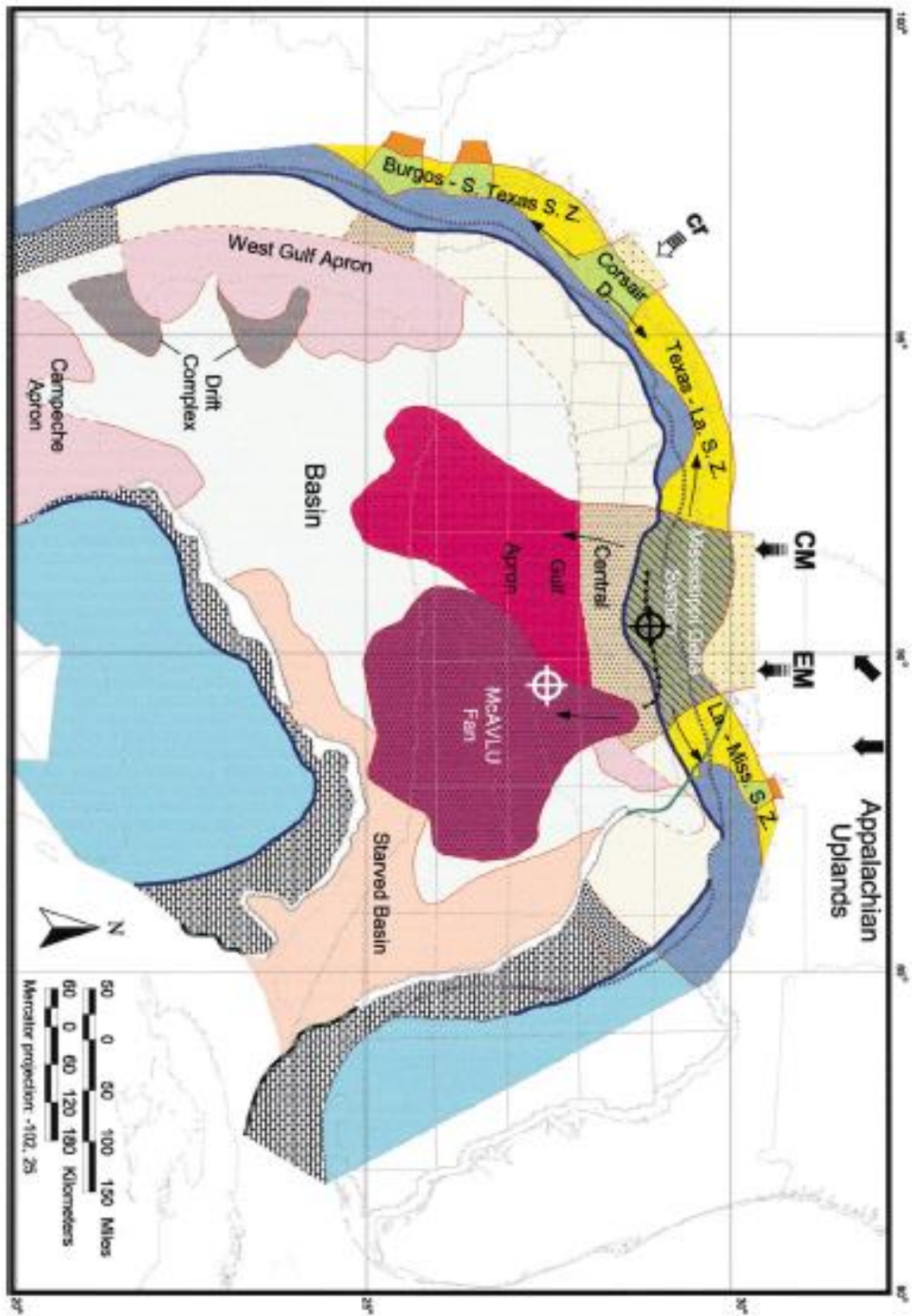


Figure 87: Paleogeography of the Late Miocene deipisode (12-6.4 Ma)

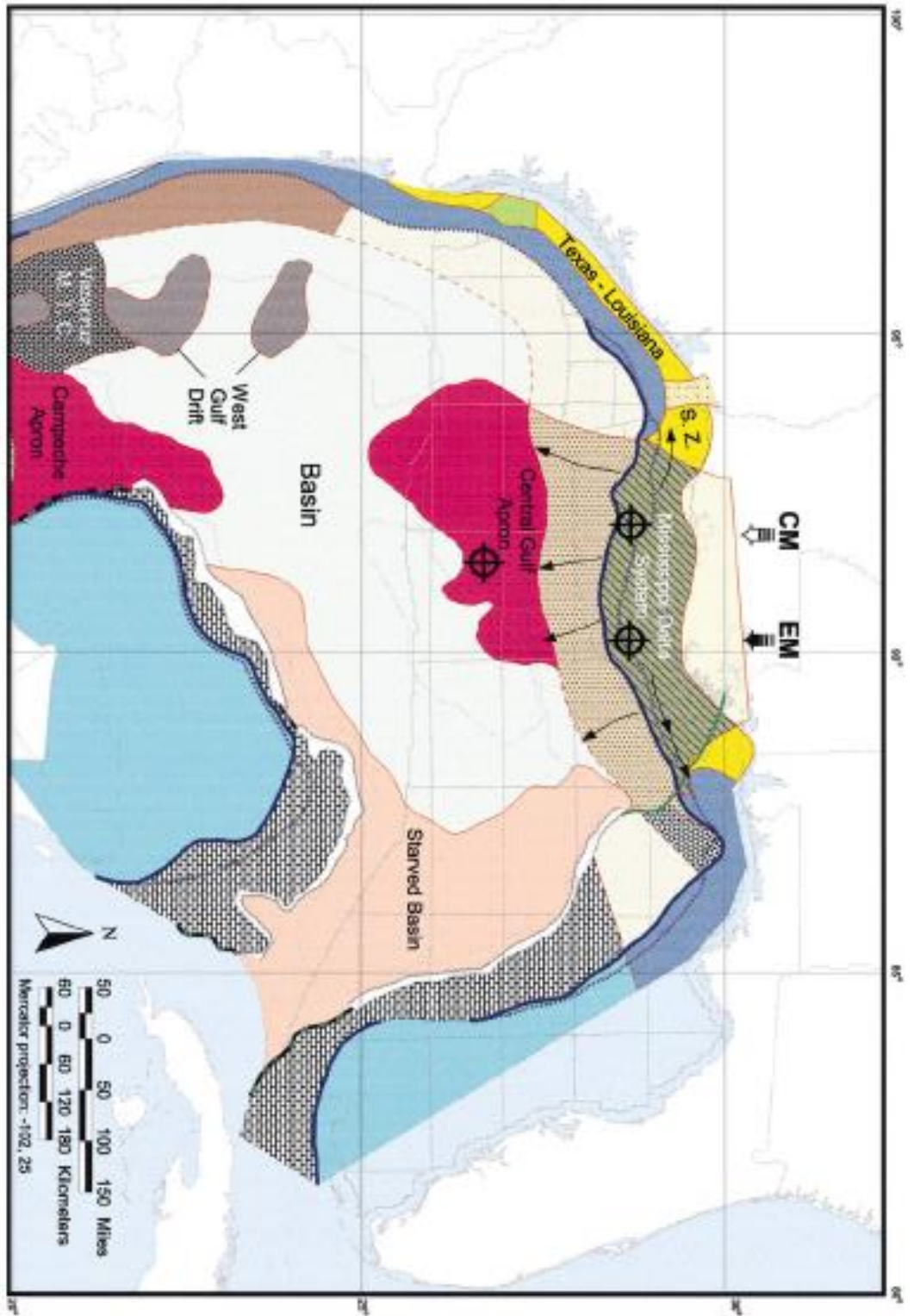


Figure 88: Paleogeography of the *Buliminella 1* debrisode (6.4-4.2 Ma)

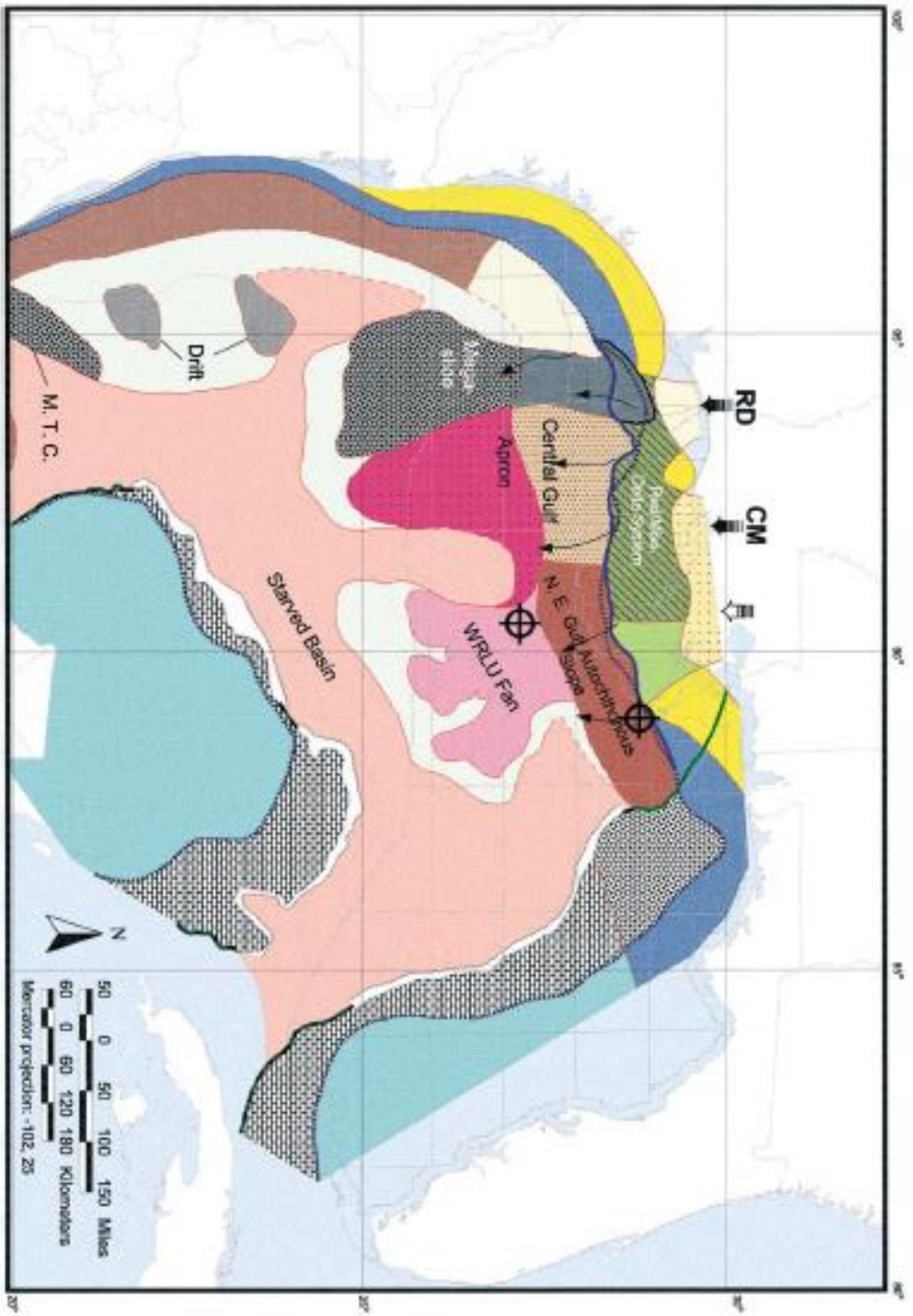


Figure 89: Paleogeography of the Globobuccina altispira depisode (4.2-3.1 Ma)

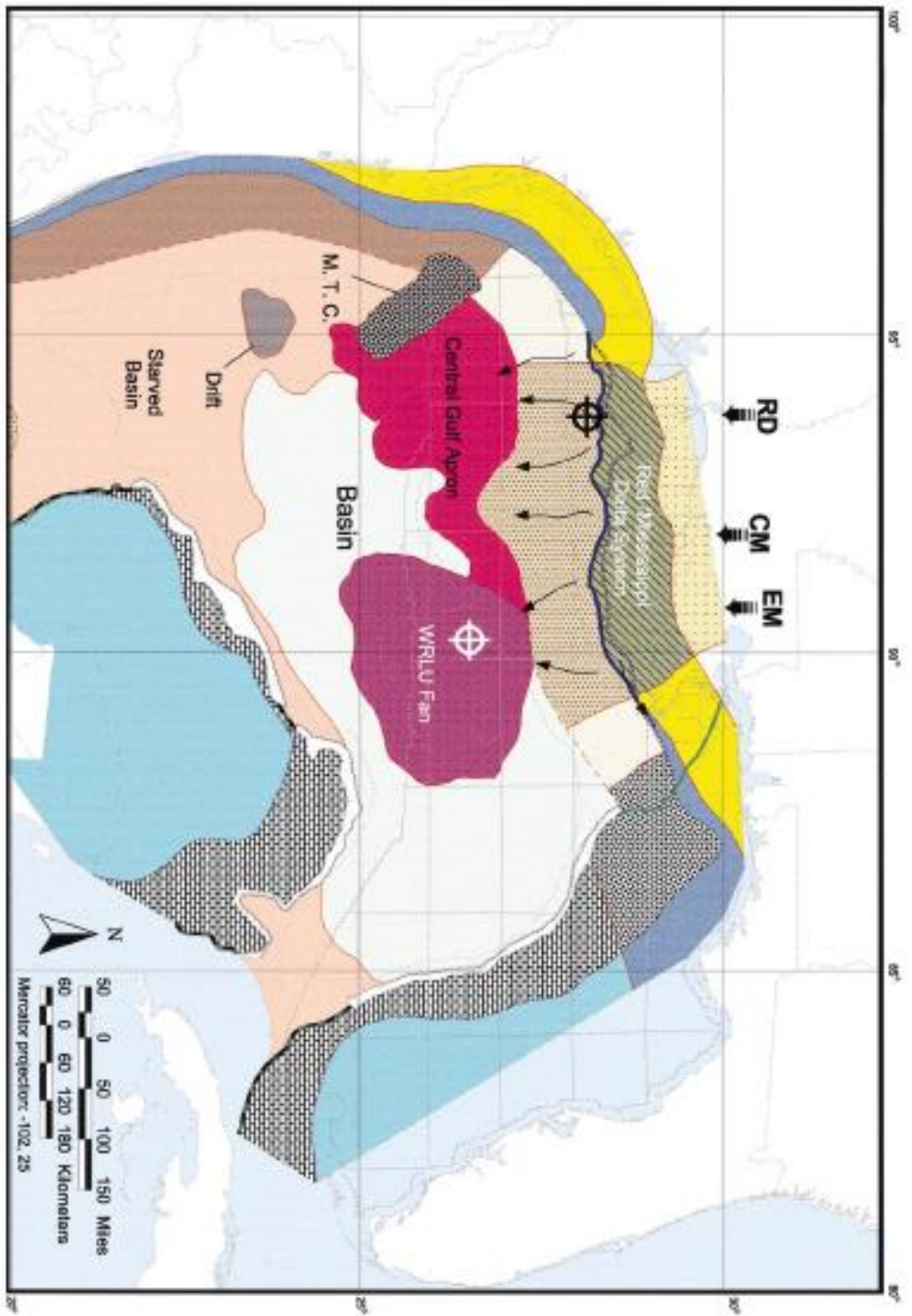


Figure 90: Paleogeography of the Lenticulina 1 deposide (3.1-2.3 Ma)

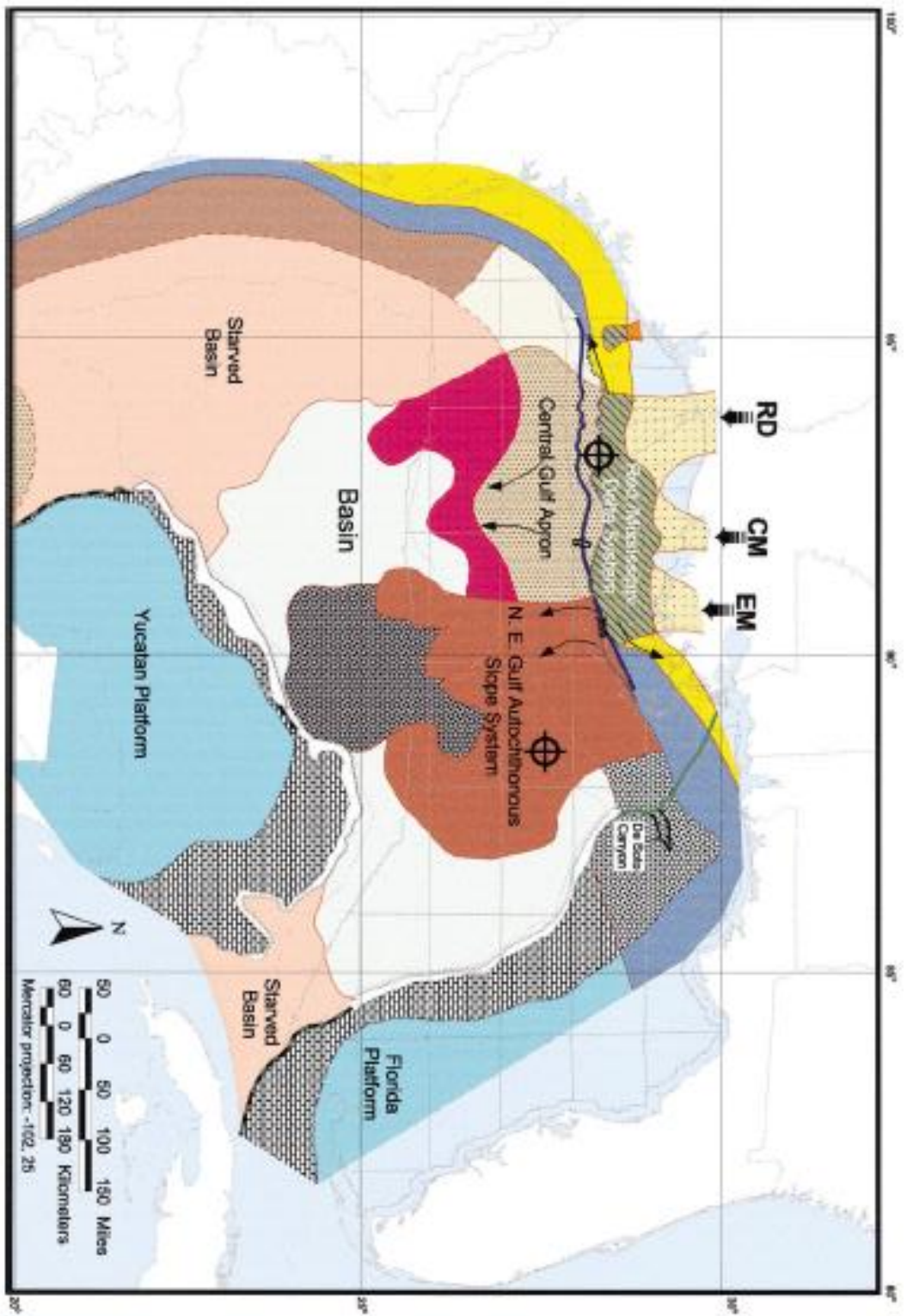


Figure 91: Paleogeography of the early phase of the Angulogerina B depisode (2.3-2 Ma)

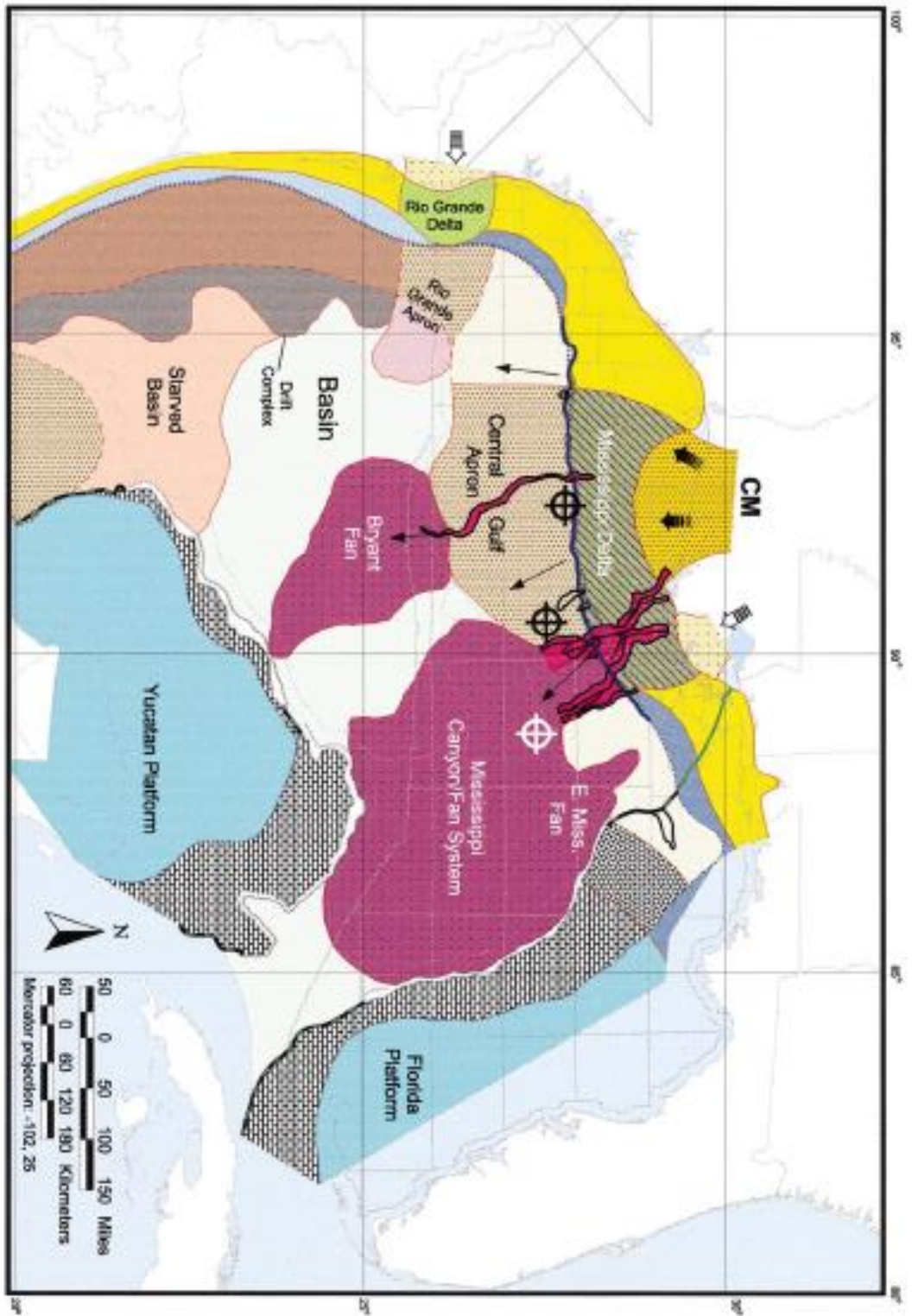


Figure 92: Paleogeography of the Sangamonian deposide (0.6-0.1 Ma)

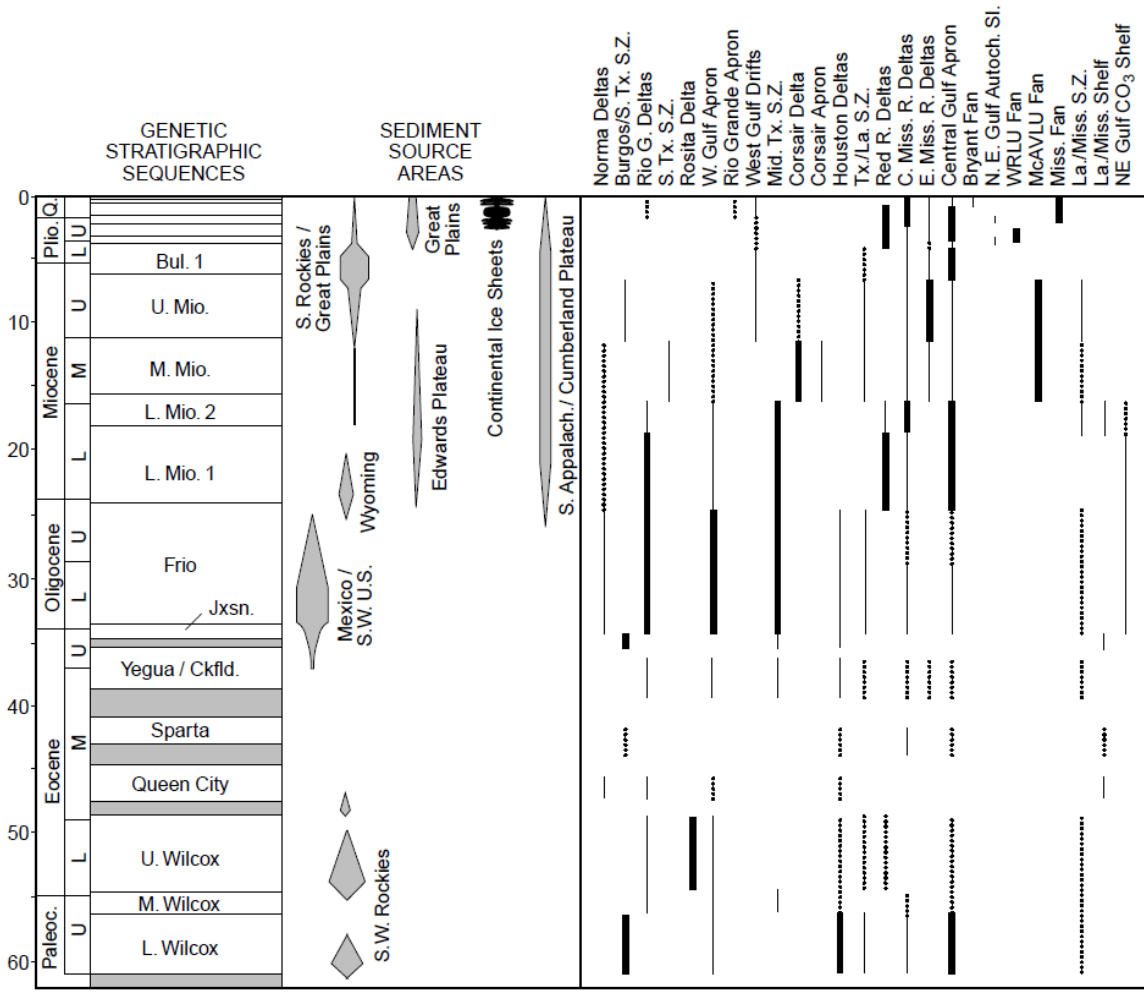


Figure 93: Temporal distribution of volumetrically important Cenozoic depositional systems of the northern Gulf basin and major tectonic phases affecting North American and adjacent Mexican sediment source areas. Bars indicate duration and relative importance of each source area's uplift. Continental glaciation also affected late Neogene sediment supply. Length of the bar beneath each system shows the period(s) of active sediment accumulation within that system. Width of bar reflects the relative volumetric importance of the depositional system. Systems are arranged by geographic location from west to east; updip systems within a major dispersal axis are to the left.

VITA

Matthew Worrell began his academic career as a music major at the University of North Texas in 2005. He transferred to Stephen F. Austin State University in 2007 and received his BA in Sociology with an Anthropology emphasis in 2011. He returned to SFA in 2012 and finished his BS in Geology in 2013 and continued directly into his studies for a MS in Geology which he completed in 2017.

Permanent address: 3230 Pearl St. #17
Nacogdoches, TX 75965

The SEG style guide (<http://seg.org/Publications/Journals/-Geophysics/Information-for-Authors/Instructions-to-authors>) was used for this thesis.

This thesis was typed by Matthew Worrell